Robust and Flexible Persistent Scatterer Interferometry for Long-Term and Large-Scale Displacement Monitoring

Zur Erlangung des akademischen Grades eines

DOKTORS DER INGENIEURWISSENSCHAFTEN (Dr.-Ing.)

von der KIT Fakultät für
Bauingenieur, Geo- und Umweltwissenschaften des
Karlsruher Instituts für Technologie (KIT)

genehmigte

DISSERTATION

von

M.Sc. Nils Dörr
geb. in St.Wendel

Tag der mündlichen Prüfung: 10.07.2023
Referent: Prof. Dr.-Ing. habil. Stefan Hinz
Korreferent: Prof. Dr. Michael Eineder

Karlsruhe 2024

Abstract

The Persistent Scatterer Interferometry (PSI) is a powerful technique to monitor displacements of the Earth's surface from space. It is based on identifying and analyzing Persistent Scatterers (PSs) by applying time series analysis approaches to stacks of Synthetic Aperture Radar (SAR) acquisitions. PSs dominate the backscatter of the resolution cells they are located in and are affected by marginal decorrelation over time. Displacements of such PSs can be monitored with potential sub-millimeter accuracy if noise sources are properly minimized.

PSI has developed into an operational technology over time in certain applications. However, challenging applications of the technique still exist. Physical land surface changes and changes in the acquisition geometry can cause PSs to appear or fade over time. The number of continuously coherent PSs decreases with increasing time series length, while the number of Temporary Persistent Scatterers (TPSs) increases which are only coherent during one or several separated segments of the analyzed time series. This is why it is desirable to include the analysis of such TPSs into PSI in order to develop a flexible PSI system which is able to handle dynamic land surface changes, thus enabling continuous displacement monitoring. Another main challenge is large-scale monitoring in regions with complex atmospheric conditions, leading to high uncertainty in the displacement time series at large distances to the spatial reference.

This thesis deals with modifications and extensions which were realized on the basis of an existing PSI algorithm with the purpose to develop a robust and flexible PSI approach that handles the above-mentioned challenges. The first main contribution is the proposal of a method to fully integrate TPSs into PSI. It is demonstrated in evaluation studies with real SAR data that the TPS integration indeed enables the handling of dynamic land surface changes and has increasing relevance for PSI-based observation networks with increasing time series length. The second main contribution is the presentation of a covariance-based reference integration into large-scale PSI for the estimation of spatially correlated noise in interferograms. The method is based on sampling the noise at reference pixels with known displacement time series and interpolating it at other PS locations, taking the spatial statistics of the noise into account. It is shown in a simulation and a real data study that the proposed method exhibits superior performance compared to alternative methods to remove spatially correlated noise in interferograms by integrating reference pixels.

The developed PSI approach is finally applied to subsidence monitoring in the Vietnamese Mekong Delta, which has recently been affected by subsidence and various other environmental challenges. The estimated subsidence rates feature high variabil-

ity on short as well large spatial scales. Highest subsidence rates of up to 6 cm/yr are mainly found in urban cities. Furthermore, it can be shown that the largest part of the subsidence originates from shallow subsurface depths. The proposed method to reduce spatially correlated noise significantly improves the results in case that a proper spatial distribution of reference areas is available. In that case, noise is effectively reduced and independent results from two interferogram stacks agree, which were acquired from different orbits. The TPS integration leads to considerably larger number in identified TPSs than PSs across the study area for the analyzed time series of six years, thus enhances the observation network significantly. A special use case of the TPS integration is presented which bases on clustering appearing TPSs to systematically identify new constructions and analyze their initial subsidence time series.

Zusammenfassung

Die Persistent Scatterer Interferometrie (PSI) ist eine Methode zur Überwachung von Verschiebungen der Erdoberfläche aus dem Weltraum. Sie basiert auf der Identifizierung und Analyse von stabilen Punktstreuern (sog. Persistent Scatterer, PS) durch die Anwendung von Ansätzen der Zeitreihenanalyse auf Stapel von SAR-Interferogrammen. PS Punkte dominieren die Rückstreuung der Auflösungszellen, in denen sie sich befinden, und werden durch geringfügige Dekorrelation charakterisiert. Verschiebungen solcher PS Punkte können mit einer potenziellen Submillimetergenauigkeit überwacht werden, wenn Störquellen effektiv minimiert werden.

Im Laufe der Zeit hat sich die PSI in bestimmten Anwendungen zu einer operationellen Technologie entwickelt. Es gibt jedoch immer noch herausfordernde Anwendungen für die Methode. Physische Veränderungen der Landoberfläche und Änderungen in der Aufnahmegeometrie können dazu führen, dass PS Punkte im Laufe der Zeit erscheinen oder verschwinden. Die Anzahl der kontinuierlich kohärenten PS Punkte nimmt mit zunehmender Länge der Zeitreihen ab, während die Anzahl der TPS Punkte zunimmt, die nur während eines oder mehrerer getrennter Segmente der analysierten Zeitreihe kohärent sind. Daher ist es wünschenswert, die Analyse solcher TPS Punkte in die PSI zu integrieren, um ein flexibles PSI-System zu entwickeln, das in der Lage ist mit dynamischen Veränderungen der Landoberfläche umzugehen und somit ein kontinuierliches Verschiebungsmonitoring ermöglicht. Eine weitere Herausforderung der PSI besteht darin, großflächiges Monitoring in Regionen mit komplexen atmosphärischen Bedingungen durchzuführen. Letztere führen zu hoher Unsicherheit in den Verschiebungszeitreihen bei großen Abständen zur räumlichen Referenz.

Diese Arbeit befasst sich mit Modifikationen und Erweiterungen, die auf der Grundlage eines bestehenden PSI-Algorithmus realisiert wurden, um einen robusten und flexiblen PSI-Ansatz zu entwickeln, der mit den oben genannten Herausforderungen umgehen kann. Als erster Hauptbeitrag wird eine Methode präsentiert, die TPS Punkte vollständig in die PSI integriert. In Evaluierungsstudien mit echten SAR Daten wird gezeigt, dass die Integration von TPS Punkten tatsächlich die Bewältigung dynamischer Veränderungen der Landoberfläche ermöglicht und mit zunehmender Zeitreihenlänge zunehmende Relevanz für PSI-basierte Beobachtungsnetzwerke hat. Der zweite Hauptbeitrag ist die Vorstellung einer Methode zur kovarianzbasierten Referenzintegration in großflächige PSI-Anwendungen zur Schätzung von räumlich korreliertem Rauschen. Die Methode basiert auf der Abtastung des Rauschens an Referenzpixeln mit bekannten Verschiebungszeitreihen und anschließender Interpolation auf die restlichen PS Pixel unter Berücksichtigung der räumlichen Statistik

des Rauschens. Es wird in einer Simulationsstudie sowie einer Studie mit realen Daten gezeigt, dass die Methode überlegene Leistung im Vergleich zu alternativen Methoden zur Reduktion von räumlich korreliertem Rauschen in Interferogrammen mittels Referenzintegration zeigt.

Die entwickelte PSI-Methode wird schließlich zur Untersuchung von Landsenkung im Vietnamesischen Teil des Mekong Deltas eingesetzt, das seit einigen Jahrzehnten von Landsenkung und verschiedenen anderen Umweltproblemen betroffen ist. Die geschätzten Landsenkungsraten zeigen eine hohe Variabilität auf kurzen sowie großen räumlichen Skalen. Die höchsten Senkungsraten von bis zu 6 cm pro Jahr treten hauptsächlich in städtischen Gebieten auf. Es kann gezeigt werden, dass der größte Teil der Landsenkung ihren Ursprung im oberflächennahen Untergrund hat. Die präsentierte Methode zur Reduzierung von räumlich korreliertem Rauschen verbessert die Ergebnisse signifikant, wenn eine angemessene räumliche Verteilung von Referenzgebieten verfügbar ist. In diesem Fall wird das Rauschen effektiv reduziert und unabhängige Ergebnisse von zwei Interferogrammstapeln, die aus unterschiedlichen Orbits aufgenommen wurden, zeigen große Übereinstimmung. Die Integration von TPS Punkten führt für die analysierte Zeitreihe von sechs Jahren zu einer deutlich größeren Anzahl an identifizierten TPS als PS Punkten im gesamten Untersuchungsgebiet und verbessert damit das Beobachtungsnetzwerk erheblich. Ein spezieller Anwendungsfall der TPS Integration wird vorgestellt, der auf der Clusterung von TPS Punkten basiert, die innerhalb der analysierten Zeitreihe erschienen, um neue Konstruktionen systematisch zu identifizieren und ihre anfängliche Bewegungszeitreihen zu analysieren.

Contents

Abbreviations

APS	atmospheric phase screen
AmPS	Ambivalent Persistent Scatterer
ANOVA	analysis of variance
CRLB	Cramér-Rao Lower Bound
DEM	digital elevation model
DePSI	Delft implementation of PSI
D-InSAR	differential InSAR
DLR	German Aerospace Center
DS	Distributed Scatterer
DBSCAN	Density-Based Spatial Clustering of Applications with Noise
EGMS	European Ground Motion Service
ESA	European Space Agency
GNSS	Global Navigation Satellite System
ILS	integer least-squares
InSAR	Interferometric Synthetic Aperture Radar
LOS	line-of-sight
LAMBDA	Least-squares Ambiguity Decorrelation Adjustment
LRT	likelihood ratio test
MAD	mean absolute deviation
M-SBAS	Multi Small Baseline Subset
MST	minimum spanning tree
MT-InSAR	Multi-Temporal InSAR
OSM	Open Street Map
OTL	ocean tide loading
PDF	probability density function
PRF	pulse repetition frequency

PS	Persistent Scatterer
PSC	Persistent Scatterer Candidate
PSI	Persistent Scatterer Interferometry
Radar	Radio Detection and Ranging
RAR	Real Aperture Radar
RMSE	root-mean-square error
SAR	Synthetic Aperture Radar
SBAS	small baseline subset
SET	solid earth tide
SLC	single look complex
SCN	spatially correlated noise
SCR	signal-to-clutter ratio
SNAPHU	Statistical-Cost, Network-Flow Algorithm for Phase Unwrapping
SNR	signal-to-noise ratio
StaMPS	Stanford Method for Persistent Scatterer Interferometry
SVD	singular value decomposition
TEC	total electron content
TPS	Temporary Persistent Scatterer
TPSC	Temporary Persistent Scatterer Candidate
TRAIN	Toolbox for Reducing Atmospheric InSAR Noise
VMD	Vietnamese Mekong Delta

Symbols

Operators and annotations

Δ_{ij}	distance between pixels i and j
diag{.}	diagonal matrix with the input vector as diagonal elements
$E\{.\}$	expectation
i	imaginary unit
$\mathcal{I}$	identity matrix
p	probability density function
$*$	complex conjugate
$W\{.\}$	wrapping operator
$\hat{.}$	hat indicating an estimated parameter

SAR observation

λ	radar wavelength
R	slant range
θ_{inc}	incidence angle
θ_0	master look angle
z	complex SAR signal
A	SAR amplitude
ψ	SAR phase
ν	amplitude of a point scatterer
σ^2	signal variance of distributed scattering

Interferometry

g	complex interferogram
ϕ	wrapped interferometric phase

φ	unwrapped interferometric phase
γ	coherence
τ	temporal baseline
ϑ	thermal baseline
$B_\perp$	perpendicular baseline
$B_\parallel$	parallel baseline

Other symbols

v	linear displacement rate in line-of-sight
α	thermally induced displacement rate in line-of-sight
h	pixel height above reference

1. Introduction

1.1. Motivation

Measuring displacements of the Earth's surface with high accuracy is a fundamental task in geodesy. The observations are essential input for the study of the underlying dynamic processes and assessments of related hazards, which in turn can be substantial for the formulation of countermeasures. Displacements of the Earth's surface are of natural and human origin, such as subsidence due to groundwater or gas exploitation, tectonic movements and earthquakes, landslides, ice flow as well as settlement and thermal expansion of infrastructure. A prominent example is subsidence in deltas worldwide, which are inhabited by about 340 Million people (Edmonds et al., 2020). Syvitski et al. (2009) showed that many deltas are sinking at much higher rates than the additional and increasing sea level rise, leading to a growing risk of severe flooding.

Geodesy provides different tools to measure surface displacements which are characterized by different accuracy and different temporal and spatial sampling. Besides the repeated surveying of geodetic networks using pointwise levelling or Global Navigation Satellite System (GNSS) measurements, Interferometric Synthetic Aperture Radar (InSAR) is an appropriate method to monitor displacements from space with potential sub-millimeter accuracy (Ferretti et al., 2007). The technique is based on evaluating phase differences between coherent Synthetic Aperture Radar (SAR) acquisitions (Massonnet and Feigl, 1998), which correspond to changes in the range from the sensor to the surface. These range changes are used to derive the surface topography and displacements over time. Main advantages of the method are the high spatial sampling which usually is in the order of meters as well as the large swath width of the acquisitions. The latter is 250 km in case of the Interferometric Wide Swath acquisition mode of the Sentinel-1 SAR sensor. The revisit time of most SAR satellites used in science is in the order of several days, which is sufficient for many applications. Main limitations of the technique are signal decorrelation (Zebker and Villasenor, 1992) and atmospheric disturbances (Zebker et al., 1997; Hanssen, 2001).

Various Multi-Temporal InSAR (MT-InSAR) techniques have been developed to tackle the limitations of InSAR. The Persistent Scatterer Interferometry (PSI) (Ferretti et al., 2001; Kampes and Hanssen, 2004; Hooper et al., 2007) was developed to identify and analyze point scatterers which dominate the backscatter cell they are located in and are affected by marginal decorrelation over time. They are usually referred to as Persistent Scatterers (PSs). The main drawback of the method is that PSs mainly form on man-made structures. In order to extend the method to natural terrain with moderate coherence, methods to analyze Distributed Scatterers (DSs) were developed.

DSs are pixels whose signal is formed by many small, random scatterers. DS analysis techniques can be subdivided into two main approaches. In the first one, the analysis is restricted to interferogram subsets with small geometrical and/or temporal baselines, referred to as small baseline subsets (SBASs), in order to minimize the impact of decorrelation (Berardino et al., 2002; Lanari et al., 2004; Hooper, 2008). The second one aims at reducing the stochastic noise in DS phase time series by exploiting all possible interferogram combinations (Guarnieri and Tebaldini, 2008; Ferretti et al., 2011; Samiei-Esfahany et al., 2016; Ansari et al., 2018). In this case, DSs can be treated like and jointly be processed like PSs after the noise reduction. DS analyses are characterized by higher computational cost and more complex parameter handling compared to PS approaches. Furthermore, they reflect averaged displacements of among adjacent pixels sharing similar reflectivity as result from multi-looking during the processing, as opposed to PSI reflecting the displacement of single scatterers. In summary, both PS and DS approaches are characterized by different advantages and disadvantages and are utilized depending on the study area and application.

MT-InSAR has developed into an operational technology in certain applications over the last 20 years. A significant example for continuous, operational displacement monitoring is the European Ground Motion Service (EGMS) which is funded by the European Commission and part of the Copernicus Land Monitoring Service (Crosetto et al., 2020; Costantini et al., 2021; Costantini et al., 2022). It applies a combination of PS and DS techniques to full-resolution Sentinel-1 acquisitions to monitor ground deformations over all Copernicus participating countries. The results are transformed into an absolute geodetic reference frame by integrating them with GNSS measurements. They are available to the public and will be annually updated.

Despite the progressive example of operational MT-InSAR monitoring by the EGMS, challenging applications for MT-InSAR still exist. A main challenge in PSI is long-term monitoring, as physical land surface changes or changes in the acquisition geometry can cause PSs to fade or appear within the available time series. The number of continuously coherent PSs decreases with increasing time series, while the number of such Temporary Persistent Scatterers (TPSs) increases. It is desirable to include the analysis of TPSs into PSI in order to develop a flexible PSI system which handles dynamic land surface changes during the time series, thus provides the best possible PSI-based geodetic measurement network for long-term displacement monitoring. Standard PSI approaches are not capable of identifying and analyzing TPSs. As a result, the number of identifiable measurement points decreases with increasing time series length. Various approaches have been proposed to identify and partially analyze TPSs (Ferretti et al., 2004; Ansari et al., 2014; Dogan and Perissin, 2014; Hu et al., 2019), but none of these fully integrated TPSs into PSI including phase unwrapping. Another main challenge in MT-InSAR in general is large scale monitoring in regions with complex atmospheric conditions, leading to high uncertainty in the displacement time series at large distances to the spatial reference. Complex atmospheric conditions for InSAR are mainly characterized by a high spatial variability of water vapor in the troposphere. This can be difficult to capture in numerical weather models, which are mainly used for tropospheric delay modelling. It was shown that the performance of

numerical weather models for tropospheric delay modelling increases with increasing latitude (Cong et al., 2018) and increasing topography of the study area (Liu et al., 2009). Several approaches have been developed to correct residual spatially correlated noise in SAR interferograms by integrating measurements from GNSS networks (Argus et al., 2005; Neely et al., 2020; Xu et al., 2021; Liu et al., 2022). These methods offer potential for improvement by taking the spatial statistics of the noise into account.

1.2. Scientific Objectives

This thesis aims at enhancing PSI to a robust and flexible technique for long-term and large-scale displacement monitoring in challenging areas. The basis for further developments is the PSI algorithm Multi Small Baseline Subset (M-SBAS), described in Schenk (2015), which was originally designed to robustly and efficiently monitor heterogeneous displacements in small-scale urban study areas. The main objectives of the thesis are summarized in the following:

- Integration of M-SBAS into large-scale PSI and design of a robust method to estimate residual spatially correlated noise to enable large-scale monitoring with minimal uncertainty.

- Full integration of TPSs into the PSI algorithm in order to achieve the best possible PS-based geodetic network for long-term monitoring.

- Test of the proposed algorithm in a suitable study area.

The proposed algorithm is tested by means of land subsidence monitoring in the Vietnamese Mekong Delta (VMD) using Sentinel-1 data acquired between 2016 and 2022. Subsidence rates of several centimeters per year have been reported recently for the area, which have been mainly attributed to groundwater over-exploitation and natural compaction of young Holocene deposits (Erban et al., 2014; Minderhoud et al., 2017; Zoccarato et al., 2018; Minderhoud et al., 2020). The VMD is suitable for testing the proposed algorithm for various reasons. The covered area of approximately $250\,\text{km} \times 230\,\text{km}$ can be considered large-scale. Furthermore, difficult atmospheric conditions for InSAR are expected in the VMD due to its low latitude, direct connection to the sea and flat topography. The time series length of six years is not exceptional long for InSAR but sufficient to test the relevance of the TPS integration into PSI, especially due to the recent high construction and land use change activity in the study area (Minderhoud et al., 2018). Beyond the main objectives of this thesis, subsidence monitoring in the VMD is essential input for the study of causes of land subsidence, related hazards and risks as well as for the formulation of countermeasures.

1.3. Thesis Outline

This thesis is organized into seven chapters. Relevant fundamentals of InSAR are described in Chapter 2. Special attention is paid to SAR and InSAR statistics, which

constitute the foundations of PS and TPS identification, as well as to the composition of the interferometric phase. The latter has to be adjusted for various contributions in order that the displacement phase can be extracted.

The fundamentals of PSI are introduced in Chapter 3. The main steps of the PSI processing are described and special features of the M-SBAS approach are characterized, which is the basis of extensions in this thesis. At the end of the chapter, further developments and potential improvements of PSI in general and M-SBAS are presented.

The integration of M-SBAS into robust large-scale PSI is the subject of Chapter 4. Special focus is put on the reduction of phase noise contributions which are especially relevant for large-scale displacement monitoring. This includes the presentation of a covariance-based integration method of reference pixels with known displacement time series to correct interferograms for residual spatially correlated noise. Reference pixels could be pixels which GNSS stations are located on or pixels which are located in stable areas. The method is validated with simulated and real data.

The integration of TPSs into the PSI approach is described in Chapter 5. Innovative extensions of existing TPS analysis approaches are the refinement of the change dates of TPSs, which define the onset and ending of their coherent segments, based on their interferometric phases as well as the joint phase unwrapping of PSs and TPSs. The temporal datum of those TPSs has to be re-defined whose lifetime does not include the selected master acquisition. Experimental results based on Sentinel-1 data acquired over the Vietnamese city of Ca Mau are presented. The relevance of the TPS integration for PSI-based observation networks as a function of the considered SAR time series length is analyzed at the end of the chapter.

Chapter 6 presents the application of the proposed approach to subsidence monitoring in the VMD. Sentinel-1 data acquired in descending and ascending orbits between April 2016 and April 2022 are analyzed. The results are examined with regard to the evaluation of the proposed method. This also includes comparisons of the results with alternative measurements. A special use case of the TPS integration is presented, which identifies new constructions by clustering appearing TPSs. The initial subsidence time series of such constructions can be systematically analyzed.

The essential aspects of the thesis are summarized in Chapter 7. The conclusion is followed by an outlook for further developments.

Parts of the thesis have been submitted or published in various publications. In the following, paragraphs marked by vertical lines along the text margins originate from such a publication. Paragraphs from Dörr et al. (2021) are marked in orange, from Dörr et al. (2022a) in blue, from Dörr et al. (2022b) in green and from Dörr et al. (2023) in purple. They are printed in the same form as originally submitted or published, with the exceptional of occasional small editorial changes.

2. Fundamentals of InSAR

This chapter introduces fundamentals of SAR and InSAR which are relevant in the context of this thesis. The principles of SAR imaging and statistics are introduced first, followed by an overview of InSAR and InSAR statistics. Finally, different InSAR approaches and applications are introduced. Comprehensive literature on SAR is found in Curlander and McDonough (1992) and Cumming and Wong (2005). Comprehensive literature on InSAR can be found in Bamler and Hartl (1998), Rosen et al. (2000), Hanssen (2001), Pepe and Calò (2017), and Minh et al. (2020).

2.1. SAR Imaging

Imaging Radio Detection and Ranging (Radar) systems are active remote sensing systems which produce two-dimensional radar backscatter maps of an object's surface, commonly the Earth's surface. They emit microwave pulses with a given pulse repetition frequency (PRF) towards the object while moving and recording the backscatter. They are employed in a side-looking acquisition geometry to prevent signal diffraction and backscatter ambiguities in the wave propagation direction, which is referred to as range direction. The range resolution depends on the wavelength of the emitted microwaves and is greatly increased by emitting frequency-modulated chirps and applying pulse compression techniques. The resolution in the moving direction of the sensor, which is called azimuth, is proportional to the angular beam width of the antenna, which increases with decreasing antenna size. This is a practical restriction of Real Aperture Radar (RAR), in addition to the fact that the resolution is also proportional to the range of the sensor to the illuminated object.

SAR bypasses the limitations of the azimuth resolution of RAR by mimicking a large antenna along the azimuth direction while actually using a short physical antenna. SAR systems emit coherent microwave pulses with a high PRF so that scatterers are illuminated many times during data acquisition. The varying range between the sensor and a scatterer during transmission of the various pulses leads to a radial velocity between both, thus to a doppler shift in the recorded data. This allows to apply compression techniques to focus the data in azimuth direction, with a-posteriori resolutions in the range of meters. The larger the range between the sensor and a scatterer, the more often it is illuminated and the longer its specific synthetic aperture. As a result, the azimuth resolution of SAR systems is, in theory, independent of the flight altitude of the sensor. The SAR imaging geometry is illustrated in Figure 2.1.
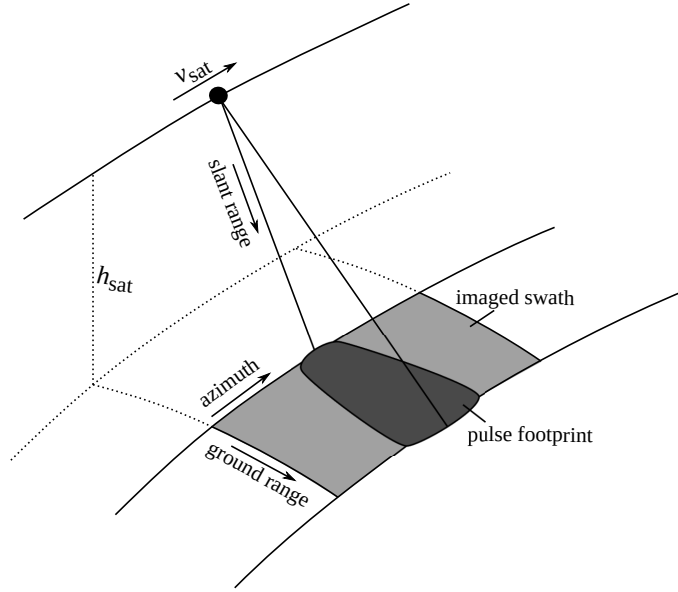
Figure 2.1.: SAR imaging geometry. The spacecraft is moving with the velocity v_{sat} in azimuth direction at a height h_{sat} above the Earth's surface. An imaged swath is formed by a number of consecutive pulses. Slant range is the direction of radar signal propagation, while the direction perpendicular to azimuth on the surface is referred to as ground range.

The SAR image formation consists of range and azimuth compression, usually carried out in the frequency domain, with weighting functions applied in order to suppress side lobes. The parameters of the applied weighting functions affect the final geometrical resolution of the SAR image. The signal is formed by the 2D convolution of the reflectivity function over the object with a range dependent phase term and the point spread function. Assuming ideal focusing conditions and discrete scatterers within the pixel, the measured signal is the complex sum of all wavelets scattered back by discrete scatterers in p (Bamler and Hartl, 1998; Hanssen, 2001). In this case, the measured signal of a pixel p can be expressed by the complex phasor

$$z = A \exp\left(i\psi\right) = \sum_{k=1}^{K} x_k + i y_k, \tag{2.1}$$

where A and ψ are the amplitude and the phase, respectively, K the number of scatterers in the pixel and x_k and y_k real and imaginary parts of their backscatter. The amplitude is defined as $A = \sqrt{I}$ with the pixel intensity I. The amplitudes of the different wavelets depend on the scatterers' reflectivity, while their phase depends on their range and location within the pixel. As a result, the phase ψ of a pixel can be described as the sum of different contributions:

$$\psi = -2\pi a + \psi_{\text{range}} + \psi_{\text{scatt}} + \psi_{\text{atmo}} + \psi_{\text{noise}}, \qquad a \in \mathbb{N} \tag{2.2}$$

with a denoting the phase ambiguity, ψ_{range} the range dependent phase, ψ_{scatt} the phase caused by the unknown pixel-specific scattering, ψ_{atmo} the phase due to the propagation delay induced in the atmosphere and ψ_{noise} the phase noise.

2.2. SAR Statistics

SAR scattering is usually distinguished into two extreme cases which are distributed scattering and point scattering. Distributed scattering describes the case of many small, random scatterers forming the signal of a resolution cell together (Figure 2.2 (a)). It is assumed that the central limit theorem applies in that case so that the signal of such a resolution cell is described as a complex circular Gaussian variable, with real and imaginary parts of the signal being independent Gaussian variables with the same variance σ^2 (Bamler and Hartl, 1998):

$$z = A \exp(i\psi) = x + iy = \sum_{k=1}^{K} x_k + iy_k, \ \text{with } x, y \sim \mathcal{N}\left(0, \sigma^2\right)$$

$$z \sim \mathcal{CN}\left(0, 2\sigma^2\right), \tag{2.3}$$

where $\mathcal{N}$ and $\mathcal{CN}$ denote the univariate Gaussian and complex circular Gaussian distributions. Under the assumptions made, the joint probability density function (PDF) of amplitude and phase is derived by applying a transformation to polar coordinates (Papoulis and Pillai, 2002) in the complex circular Gaussian distribution (Goodman, 1963):

$$p(A, \psi) = \frac{A}{2\pi\sigma^2} \exp\left(-\frac{A^2}{2\sigma^2}\right). \tag{2.4}$$

The marginal PDF of the signal amplitude is the Rayleigh distribution

$$p(A) = \left(\frac{A}{\sigma^2}\right) \exp\left(-\frac{A^2}{2\sigma^2}\right), \tag{2.5}$$

and the marginal PDF of the phase is

$$p(\psi) = \frac{1}{2\pi}, \tag{2.6}$$

i.e. uniform. As a result, the phase of a distributed scatterer is without information in a single SAR acquisition.

Point scattering occurs when a strong scatterer dominates the backscatter of a resolution cell, while all other small, random scatterers form the clutter (Figure 2.2 (b)). The signal of such a resolution cell can be considered as a complex deterministic signal $z_p = v \exp(i\psi_0)$ perturbed by clutter which follows the complex circular Gaussian statistics described before for distributed scatterers. The joint PDF of amplitude and phase is in this case (Blachman, 1953)

$$p(A, \psi) = \frac{A}{2\pi\sigma^2} \exp\left(-\frac{A^2 + v^2 - 2Av\cos(\psi - \psi_0)}{2\sigma^2}\right). \tag{2.7}$$
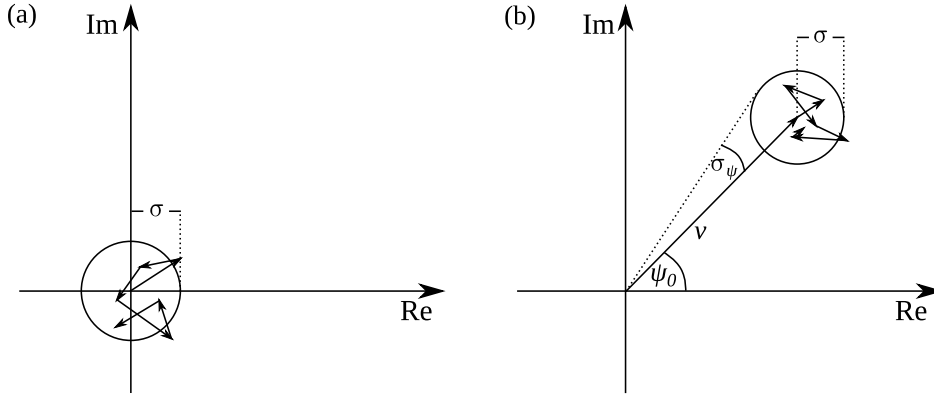
Figure 2.2.: (a) Complex phasor of a distributed scatterer. The signal is formed by many random scatterers visualized by arrows. It follows a complex circular Gaussian distribution with real and imaginary parts being independent variables sharing the same variance σ^2, which is illustrated by the circle with radius equaling the standard deviation σ. (b) Complex phasor of a point scatterer. The point scatterer is characterized by the deterministic signal $z_p = \nu \exp(i\psi_0)$ which is perturbed by clutter. The clutter is characterized by the same statistics of a distributed scatterer.

The marginal PDF of the amplitude is the Rice distribution (Rice, 1948)

$$p(A) = \frac{A}{\sigma^2} \exp\left(-\frac{A^2 + \nu^2}{2\sigma^2}\right) I_0\left(\frac{A\nu}{\sigma^2}\right), \tag{2.8}$$

where I_0 denotes the modified Bessel function of first kind. The signal-to-clutter ratio (SCR) of a point scatterer is defined as

$$\mathrm{SCR} = \frac{\nu^2}{2\sigma^2}. \tag{2.9}$$

The Rice distribution approaches the Gaussian distribution for large SCR values and the Rayleigh distribution (Equation 2.5) for low SCR values (Goodman, 2015).

The marginal PDF of the phase of a point scatterer is given by (Blachman, 1953)

$$\begin{aligned}
p(\psi) = &\frac{1}{2\pi} \exp\left(-\frac{\nu^2}{2\sigma^2}\right) \\
&+ \frac{\nu}{\sqrt{2\pi}\sigma} \cos(\psi - \psi_0) \exp\left(-\frac{\nu^2}{2\sigma^2} \sin^2(\psi - \psi_0)\right) \mathrm{ERF}\left(\frac{\nu}{\sigma} \cos(\psi - \psi_0)\right),
\end{aligned} \tag{2.10}$$

with the error function

$$\mathrm{ERF}(x) = \frac{1}{\sqrt{2\pi}} \int_{-\infty}^{x} \exp\left(\frac{-u^2}{2}\right) du. \tag{2.11}$$

The PDF approaches the uniform phase density function of a distributed scatterer (Equation 2.6) for small SCR. For large SCR values, we can assume $|\psi - \psi_0| \ll 1$ and the PDF approaches

$$p(\psi) = \frac{\nu}{\sqrt{2\pi}\sigma} \exp\left(-\frac{\nu^2(\psi - \psi_0)}{2\sigma^2}\right), \tag{2.12}$$

i.e., a normal distribution about ψ_0 with standard deviation

$$\sigma_\psi = \frac{\sigma}{\nu}. \tag{2.13}$$

Gaussian statistics are widely assumed in SAR applications to characterize distributed scattering and clutter (Bamler and Hartl, 1998; Hanssen, 2001; Ferretti et al., 2001; Hu et al., 2019), including this thesis. However, it has to be noted that the assumptions necessary to justify the use of Gaussian statistics are violated under certain conditions, especially when the scatterers in a resolution cell are highly heterogeneous or when the geometrical resolution of the SAR system is very high, leading to small number of physical scatterers (Trunk, 1972; Skolnik, 1999). Various non-Gaussian PDFs have been introduced to account for non-Gaussian SAR backscatter (Anastassopoulos et al., 1999; Kuruoğlu and Zerubia, 2004; Eltoft, 2005).

2.3. Interferometric Phase

The scattering phase of a SAR pixel is unknown if the exact position of scatterers within the pixel is unknown. In addition, the atmospheric conditions at the time of acquisition are usually unknown. These circumstances prevent the direct phase analysis of single SAR acquisitions in geoscientific applications. The difference between two or more acquisitions can, however, lead to the reduction of the unknown phase contributions. This characteristic is made use of in InSAR, which is described in the following.

An interferogram g is formed by the complex conjugated multiplication of two coregistered SAR acquisitions z_0 and z_1, one of which is called master and the other one slave:

$$g = z_0 z_1^* = |z_0|\,|z_1| \exp\left(i\left(\psi_0 - \psi_1\right)\right) = |z_0|\,|z_1| \exp\left(i\varphi\right), \tag{2.14}$$

where $(.)^*$ denotes the complex conjugate and φ the absolute phase difference. The measured interferometric phase ϕ is wrapped into the interval $[-\pi, \pi)$

$$\phi = \arg\left\{\exp\left(i\varphi\right)\right\} = W\{\varphi\} = \varphi - 2\pi a \quad \text{with } a \in \mathbb{N}. \tag{2.15}$$

with the wrapping operator W. The interferometric phase is usually described by the following functional model:

$$\begin{aligned}
\phi &= W\left\{\varphi_{\text{range}} + \varphi_{\text{atmo}} + \varphi_{\text{orb}} + \varphi_{\text{noise}}\right\} \\
&= W\left\{-\frac{4\pi}{\lambda}\left(R_0 - R_1\right) + \varphi_{\text{atmo}} + \varphi_{\text{orb}} + \varphi_{\text{noise}}\right\},
\end{aligned} \tag{2.16}$$

with the interferometric phase φ_{range} due to the range difference $R_0 - R_1$ for both acquisitions, the phase φ_{atmo} resulting from differences in the atmospheric delays at the acquisitions, φ_{orb} due to orbital errors of master and slave and phase noise φ_{noise}. The factor 4π results from the two-way travel path of the signal.
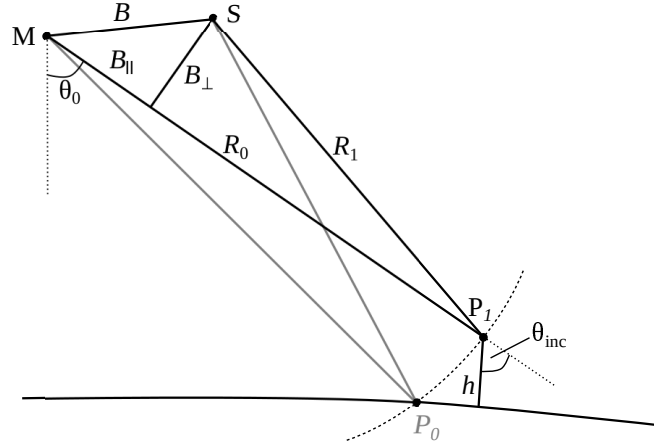
Figure 2.3.: Baseline configuration of repeat-pass InSAR. Master and slave orbits are labelled as M and S. The flight direction of the sensor is into the paper plane. The baseline B denotes the distance between M and S. $B_\parallel$ and $B_\perp$ refer to the parallel and perpendicular component of the baseline with regard to the line-of-sight (LOS) direction of the master. P_1 is a point at height h above the reference surface. P_0 is located on the reference surface at the same range R_0 to M as P_1, thus both points are located in the same range resolution cell. R_1 is the range between S and P_1. The look angle of the sensor θ_0 and the incidence angle θ_{inc} at the surface do not equal due to the earth curvature and local topography.

The acquisition configuration of an interferogram is displayed in Figure 2.3. Master and slave are usually acquired from different orbit positions and, in repeat-pass interferometry, at different times. As a result, the range-dependent interferometric phase can be split into three parts:

$$\varphi_{\text{range}} = \varphi_{\text{flat}} + \varphi_h + \varphi_{\text{defo}}. \tag{2.17}$$

The flat Earth phase φ_{flat} accounts for the phase resulting from range differences of both orbits to a reference surface like the ellipsoid, while the topographic phase φ_h is due to the topography above this reference surface. The deformation phase φ_{defo} is caused by displacements of the surface between both acquisitions. Summarizing, the functional model becomes

$$\phi = W\left\{\varphi_{\text{flat}} + \varphi_h + \varphi_{\text{defo}} + \varphi_{\text{atmo}} + \varphi_{\text{orb}} + \varphi_{\text{noise}}\right\}. \tag{2.18}$$

The contributions of the model are described in more detail in the following.

Flat Earth and Topographic Phase

The geometrical baseline B defines the distance between master and slave acquisitions (Figure 2.3) and is responsible for different contributions in interferograms. Nonzero baseline leads to a phase variation in ground range direction and a phase contribution correlated to the surface topography. Furthermore, the baseline length can be

responsible for geometrical decorrelation (Zebker and Villasenor, 1992), leading to phase noise (see in description of phase noise below).

The flat earth phase φ_{flat} is caused by range differences of master and slave to a reference surface like the ellipsoid (Figure 2.3). Using the notation from Figure 2.3, the phase is

$$\varphi_{\text{flat}} = -\frac{4\pi}{\lambda} \left(R_{\text{M,P}_0} - R_{\text{S,P}_0} \right), \tag{2.19}$$

where $R_{\text{X,Y}}$ denotes the range between points X and Y. Under the far-field or parallel-ray approximation for $B << R$ (Zebker and Goldstein, 1985; Rosen et al., 2000), the phase can be approximated as

$$\varphi_{\text{flat}} = -\frac{4\pi}{\lambda} B_{\parallel}, \tag{2.20}$$

with the parallel baseline $B_{\parallel}$ which is the projection of the baseline vector onto the LOS. The flat earth phase is visible in interferograms as a phase ramp in ground range direction, since $B_{\parallel}$ increases with increasing ground range (Rosen et al., 2000; Hanssen, 2001).

The actual topography h of a pixel above the reference surface leads to an additional range difference between master and slave acquisitions. It is defined as

$$\varphi_h = -\frac{4\pi}{\lambda} \left(R_{\text{M,P}_1} - R_{\text{S,P}_1} - \left(R_{\text{M,P}_0} - R_{\text{S,P}_0} \right) \right), \tag{2.21}$$

with $R_{\text{M,P}_1} = R_0$ and $R_{\text{S,P}_1} = R_1$. P_0 and P_1 are located in the same range resolution cell, thus the equation simplifies to

$$\varphi_h = -\frac{4\pi}{\lambda} \left(R_{\text{S,P}_0} - R_{\text{S,P}_1} \right). \tag{2.22}$$

Applying the far-field approximation again, the topographic phase can be approximated as (Zebker and Goldstein, 1985; Hanssen, 2001)

$$\varphi_h = -\frac{4\pi B_{\perp}}{\lambda \sin \theta_0 \, R_0} h, \tag{2.23}$$

where $B_{\perp}$ denotes the perpendicular baseline and θ_0 the satellite look angle at master acquisition.

Deformation Phase

A displacement of the surface between master and slave acquisitions can lead to an additional range difference if the projection of the displacement onto the LOS (d_{los}) is nonzero. This consequently also means that InSAR is only able to measure projections of displacements in the LOS direction. The resulting phase is

$$\varphi_{\text{defo}} = -\frac{4\pi}{\lambda} d_{\text{los}}. \tag{2.24}$$

The LOS measurements are sensitive to both horizontal and vertical displacements. However, they are basically insensitive to horizontal displacements in north-south direction due to the near-polar orbits of SAR satellites, corresponding to orbit headings close to the north-south direction (Wright et al., 2004; Fuhrmann and Garthwaite, 2019). It is possible to separate the vertical displacement component from a horizontal component by assuming the direction of the horizontal displacement and combining LOS measurements from ascending and descending orbits (Hu et al., 2014; Fuhrmann and Garthwaite, 2019).

Atmospheric Phase

Radar signals are delayed in media with a refractive index $n > 1$. The resulting two-way phase delay along the travel path x is

$$\psi = -\frac{4\pi}{\lambda} \int_x n(x) dx. \tag{2.25}$$

The atmosphere can be described as a medium with spatially and temporally heterogeneous refractive index, which depends on various atmospheric parameters and is slightly larger than *one* (Smith and Weintraub, 1953; Hanssen, 2001). The atmospheric phase delay contributing to a SAR scene is usually referred to as atmospheric phase screen (APS). Changes in the refractive index between master and slave lead to an interferometric phase difference which is determined by the integrated difference in the refractive index along the signal travel paths at both acquisitions, i.e., the difference of master and slave APS. Assuming the same travel path at both acquisitions, the interferometric phase delay is

$$\varphi_{\text{atmo}} = -\frac{4\pi}{\lambda} \int_x \left(n(x, t_M) - n(x, t_S) \right) dx, \tag{2.26}$$

where $n(x, t_0)$ and $n(x, t_1)$ are the refractive indices along the travel path at master and slave acquisitions, respectively.

Significantly variable refractive indices are found in the troposphere and the ionosphere (Tarayre and Massonnet, 1994; Hanssen, 2001). The refractive index in the troposphere mainly depends on the atmospheric pressure, the atmospheric temperature and the water vapor content (Smith and Weintraub, 1953). The resulting tropospheric phase delay is usually divided into the sum of wet and dry delay (Goldhirsh and Rowland, 1982; Zebker et al., 1997; Hanssen, 2001). The wet delay describes the delay contribution from the water vapor. It is highly variable in space and time and can reach pseudo range differences of up to several decimeters in interferograms. The dry delay accounts for the residual contribution of the atmospheric phase delay, mainly caused by temperature and pressure. The total dry delay can amount to several meters in SAR acquisitions (Elgered, 1982), thus is considerably larger than the wet delay. However, it has much lower impact on the interferometric phase owing to less spatial and temporal variability (Hanssen et al., 1999).

Another practical way of decomposing the atmospheric phase delay is to distinguish between vertically stratified and turbulent delay (Zebker et al., 1997; Hanssen, 2001). The vertically stratified delay comprises contributions from dry and wet delay, whereas the turbulent delay is primarily due to the variable water vapor content. Temporal variations in the stratified atmosphere lead to an interferometric phase delay which is correlated to surface elevation (Delacourt et al., 1998; Doin et al., 2009). The turbulent delay is caused by local and large-scale water vapor transport. Examples of different meteorological phenomena mapped by InSAR were shown in Hanssen et al. (1999). A deterministic description of these processes is difficult, thus the interferometric phase caused by the turbulent atmosphere is typically assessed in a stochastic way with the spatial covariance (Hanssen, 2001; Knospe and Jónsson, 2010) or by means of its spatial power law spectrum, which can be described by the Kolmogorov turbulence theory (Goldstein, 1995; Williams et al., 1998; Hanssen, 2001). With regard to the temporal and spatial acquisition parameters of InSAR, the tropospheric phase delay is often considered as spatially correlated and temporally uncorrelated with regard to the revisit time of SAR satellites. However, it has been shown that it can be seasonally correlated (Doin et al., 2009).

The ionosphere is characterized by free electrons which arise due to ionization processes through the interaction of the medium with sun radiation. The interaction of the traversing radar waves with the free electrons leads to a dispersive delay (Tarayre and Massonnet, 1994; Belcher, 2008). The refractive index is inversely proportional to the signal frequency and proportional to the electron density. As a result, the total ionospheric delay increases with decreasing frequency and depends on the total electron content (TEC) which is the integrated electron density along the travel path. The electron density varies with time of day, time of year, latitude and solar activity (Tarayre and Massonnet, 1994; Snoeij et al., 2001). Differences in the TEC between master and slave lead to an interferometric phase delay which has decreasing significance with increasing SAR frequency. The effect is significant for InSAR studies with P- and L-band SAR (Gray et al., 2000) and partially for C-band InSAR studies, depending on the latitude and time of day at acquisition (Liang et al., 2019). The effect is largest in low-latitude areas and larger at dusk than dawn.

Orbit Error Phase

Orbital errors of master and slave propagate into the determination of the interferometric baseline, thus into the estimation of the flat earth and topographic phase. The orbit error phase φ_{orb} compensates for these errors in the functional model of the interferometric phase. Comprehensive descriptions of orbit errors in InSAR and their estimation are given in Hanssen (2001), Bähr (2013) and Fattahi and Amelung (2014). They usually generate a spatial phase trend in interferograms, thus are important to consider for studies of long-wavelength displacements. Fattahi and Amelung (2014) showed that the impact of orbit errors on InSAR, especially MT-InSAR, has decreased for new satellite missions like Sentinel-1 and TerraSAR-X, compared to older missions like ERS-1 and or ENVISAT, due to more precise orbit measurements with on-board

GPS receivers. They reported orbital uncertainties of maximum $0.5\,\text{mm/yr}\,100\,\text{km}^{-1}$ for TerraSAR-X and Sentinel-1.

Phase Noise

The phase noise comprises all residual phase contributions and is referred to as decorrelation. Main decorrelation sources are changing scattering characteristics of the SAR pixels between master and slave, processing noise like coregistration errors and thermal noise of the SAR instrument. Decorrelation leads to a loss in the magnitude of the complex coherence γ of a pixel in an interferogram, which is defined as the complex correlation of the two SAR signals z_0 and z_1:

$$\gamma = \frac{E\{z_0 z_1^*\}}{E\{|z_0|^2\}E\{|z_1|^2\}}, |\gamma| \in [0, 1],\tag{2.27}$$

where $E\{.\}$ denotes the expectation value. The coherence is affected by contributions of the different decorrelation sources, which are multiplicative (Zebker and Villasenor, 1992):

$$\gamma = \gamma_{\text{temp}} \times \gamma_{\text{geom}} \times \gamma_{\text{dopp}} \times \gamma_{\text{therm}} \times \gamma_{\text{proc}}.\tag{2.28}$$

Temporal decorrelation γ_{temp} accounts for physical changes of the pixels between the acquisitions. Examples are the growth and movement s of vegetation, water movement and demolition or reconstruction work on man-made buildings. The temporal decorrelation in vegetated areas is smaller for low frequency compared to higher frequency SAR systems, since the former are less sensitive to small scattering changes. Geometrical decorrelation γ_{geom} is caused by varying incidence angles and increases with increasing geometrical baseline. The critical baseline describes the perpendicular baseline which pixel scattering becomes completely uncorrelated at.

The Doppler decorrelation γ_{dopp} is caused by differences in the doppler centroid frequencies between master and slave. This effect is small for SAR systems with proper antenna steering, such as Sentinel-1. Thermal noise of the sensor during acquisitions leads to thermal decorrelation γ_{therm}, while processing decorrelation γ_{proc} is caused by processing errors like coregistration errors. The coregistration requirements are exceptionally high for Sentinel-1 due to its burst imaging and azimuth beam steering. For this reason, enhanced coregistration approaches incorporating enhanced spectral diversity were proposed (Yague-Martinez et al., 2016).

2.4. InSAR Statistics

The previously introduced coherence (Equation 2.27) is a key parameter in the statistics of InSAR. As described in Section 2.3, it provides a measure of the persistence of the backscatter signal of a resolution cell, and its absolute value has been shown to be related to the signal-to-noise ratio (SNR) of the signal (Zebker and Villasenor, 1992):

$$|\gamma| = \frac{\text{SNR}}{\text{SNR} + 1}.\tag{2.29}$$

Furthermore, the marginal PDF of the interferometric phase is a function of the coherence (Just and Bamler, 1994; Lee et al., 1994)

$$
p(\phi) = \frac{1 - |\gamma|^2}{2\pi} \frac{1}{1 - |\gamma|^2 \cos^2(\phi - \phi_0)} \\
\times \left(1 + \frac{|\gamma| \cos(\phi - \phi_0) \arccos(-|\gamma| \cos(\phi - \phi_0))}{(1 - |\gamma|^2 \cos^2(\phi - \phi_0))^{1/2}} \right),
\tag{2.30}
$$

where ϕ_0 denotes the expected value of the interferometric phase which equals the phase of the coherence $E\{\phi\} = \phi_0 = \arg\{\gamma\}$. The PDF is periodic with 2π. The joint PDF of interferometric amplitude and phase as well as the marginal PDF of the interferometric amplitude are given in Bamler and Hartl (1998). Just and Bamler (1994) showed that the phase variance is independent of ϕ_0 and presented numerical evaluations of it. Rodriguez and Martin (1992) derived the Cramér-Rao bound for the phase variance which is given by

$$
\sigma_\phi^2 = \frac{1 - |\gamma|^2}{2|\gamma|^2}.
\tag{2.31}
$$

This phase variance is useful to describe point scattering with an absolute coherence close to one.

The coherence estimation is crucial but challenging, thus subject to intense research (Seymour and Cumming, 1994; Ferretti et al., 2011; Deledalle et al., 2011; Jiang et al., 2014; Mukherjee et al., 2021; Adam, 2022). The challenge lies in the fact that no ensemble averaging is possible due to the absence of simultaneously acquired interferograms. As a result, the coherence is estimated under the assumption of spatial or temporal stationarity and ergodicity. In the case of distributed scattering, spatial stationarity is generally assumed within uniform regions, so the coherence can be estimated by averaging over these regions (Seymour and Cumming, 1994). Point scatterers, which are the scatterer type of interest in this thesis, are usually examined in MT-InSAR approaches. Their coherence is estimated assuming temporal stationarity. For a stack of N available interferograms which are denoted as $g_n = z_0^n z_1^{n*}$, the coherence estimator for a point scatterer under this assumption is

$$
|\hat{\gamma}| = \frac{\left| \sum_{n=1}^{N} g_n \right|}{\sqrt{\sum_{n=1}^{N} |z_0^n|^2 + \sum_{n=1}^{N} |z_1^n|^2}}.
\tag{2.32}
$$

Alternatively, Ferretti et al. (2001) introduced the phase coherence

$$
|\hat{\gamma}_\phi| = \frac{1}{N} \left| \sum_{n=1}^{N} \exp\left(i\phi_n\right) \right|.
\tag{2.33}
$$

Schenk (2015) numerically compared the bias of both estimators and found the estimator in 2.32 to be characterized by lower bias, especially at high coherence values. He also showed that the coherence estimation becomes more robust for overdetermined interferogram stacks, i.e., stacks with permuting master acquisitions.

2.5. InSAR Approaches and Applications

The composition of the interferometric phase (Equation 2.18) provides an overview of possible applications of InSAR in earth science. First InSAR studies concerned topographic mapping of the Earth's surface (Graham, 1974; Zebker and Goldstein, 1985), followed by studies of surface displacements induced by geophysical phenomena like seismic events, ice flow, subsidence due to aquifer drawdown and volcanic deformation (Gabriel et al., 1989; Massonnet et al., 1993; Rignot et al., 1995; Galloway et al., 1998; Hooper and Zebker, 2007). The atmospheric delay is considered as noise in most InSAR applications. In that regard, the tropospheric delay is a large noise source (Section 2.3). However, InSAR has also been used for atmospheric parameter inversions (Hanssen et al., 1999; Meyer et al., 2006; Alshawaf et al., 2015; Fersch et al., 2022). Other exemplary applications of InSAR include land cover studies (Engdahl and Hyyppä, 2003; Jacob et al., 2020) and urban damage detection (Arciniegas et al., 2007; Milillo et al., 2018) based on the coherence.

In this thesis, we apply InSAR to study displacements of the Earth's surface. Early displacement studies based on InSAR made use of single interferograms, which is still done when studying displacements with large amplitudes, e.g. displacements caused by an earthquake. For this purpose, the interferometric phases have to unwrapped, which is the process of solving the phase ambiguity modulo 2π within the interferograms. In order to reduce unwanted phase contributions in the interferograms, the phase due to the height is subtracted with the help of digital elevation models (DEMs) and the interferograms can, if necessary, be filtered. This method is called differential InSAR (D-InSAR). Main limitations of D-InSAR are decorrelation and atmospheric noise whose phase contributions often exceed the phase signals of interest by far in single interferograms, when studying small amplitude displacements.

Several MT-InSAR time series approaches have been developed to tackle the mentioned limitations of D-InSAR. A crucial characteristic of MT-InSAR approaches is their interferogram network, describing which SAR scenes are combined to form interferograms that are used for the analysis. The goal is to minimize the sum decorrelation in the data set with the right choice of interferograms. Various interferogram networks have been proposed for different MT-InSAR approaches and the baseline configurations of three of the most applied networks are displayed in Figure 2.4: the single-master, small-baseline and fully connected multi-master networks.

The PSI technique (Ferretti et al., 2001; Kampes and Hanssen, 2004; Hooper et al., 2007) aims at identifying and analyzing coherent point scatterers. These scatterers are referred to as PSs which are assumed to be affected by marginal temporal and geometrical decorrelation over time. As a result, the single-master interferogram network is usually used for PSI analyses, which permits interferograms with large perpendicular and temporal baselines. This network is characterized by one master and all other scenes are slaves. The master is usually selected the way that the sum decorrelation is minimized (Hooper et al., 2007). The largest limitation of PSI is that PSs mainly form on man-made structures.
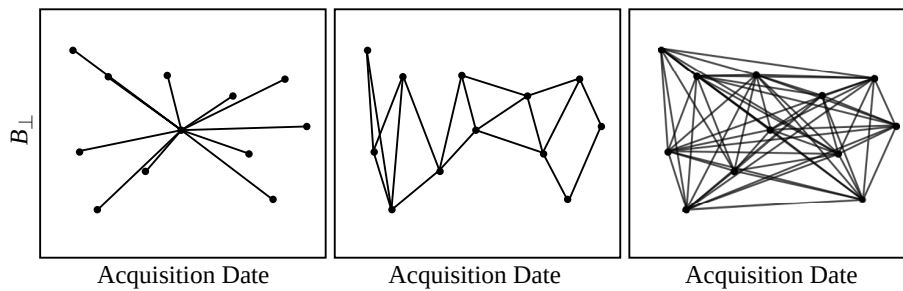
Figure 2.4.: Examples of different baseline configurations used in MT-InSAR. The dots show acquisition dates and corresponding perpendicular baselines $B_\perp$ with respect to the master. The lines represent interferogram connections. (Left) Single-master network, (center) small-baseline network, (right) fully connected multi-master network.

The identification analysis of DSs was introduced in order to include natural surfaces with moderate coherence into MT-InSAR. As a result of the possibly large temporal and geometrical decorrelation, the single-master interferogram cannot be used for the analysis of DSs. DS analysis techniques can generally be divided into two approaches: The first ones limit the MT-InSAR analysis to coherent interferograms characterized by small spatial and/or temporal baselines and are called SBAS techniques (Berardino et al., 2002; Lanari et al., 2004; Hooper, 2008). The latter exploit all available multi-master interferograms to estimate the wrapped phase time series of DSs (Guarnieri and Tebaldini, 2008; Ferretti et al., 2011; Samiei-Esfahany et al., 2016; Ansari et al., 2018), which then can be treated like and jointly processed with PSs. PS analyses are characterized by significantly lower processing times and simpler parameter handling than DS approaches. Moreover, they reflect the displacement at a certain singular scatterer, while DS approaches provide averaged displacements among several pixels. This is why PSI is still widely applied in geophysical and geodetic research, depending on the study area and the research question (Crosetto et al., 2019; Tomás et al., 2019; Aslan et al., 2020).

SAR interferograms have an integer phase ambiguity modulo 2π due to unknown absolute atmospheric and ionospheric conditions, tidally induced displacements and plate motions. Even if there are first approaches to recover the absolute phase history of interferogram stacks (Xu and Sandwell, 2020), InSAR is mostly applied as a double-differential method in space and time. The unwrapped phase observations are referenced in time to a selected SAR scene and in space to one or several reference pixels in order to remove the integer phase ambiguity of the interferograms. Obviously, variations of atmospheric delays and other long-wave noise contributions within interferograms remain as noise, which increases with increasing distance to the reference (Fattahi and Amelung, 2015; Parizzi et al., 2021). These effects should be removed as much as possible in order to increase the InSAR performance. The spatial reference is in most cases selected at a region with known displacements, e.g. in presumably stable areas. A datum connection can be carried out if displacement measurements in an absolute geodetic datum are available for certain pixels, for example when corner

reflectors or active transponders are connected to GNSS antennas (Mahapatra et al., 2018).

3. Persistent Scatterer Interferometry

In this chapter, the foundations of PSI in general and the main PSI approaches are described. The M-SBAS approach, proposed in Schenk (2015), is described individually as it is subject to adaptations and extensions in this thesis. Further developments of PSI and potential improvements of PSI in general and M-SBAS are given at the end of the chapter.

3.1. General Procedure

The PSI approach was first introduced by Ferretti et al. (2001) as a MT-InSAR approach to overcome the main limitations of D-InSAR, which are temporal decorrelation and atmospheric disturbances. Similar approaches and adaptions were proposed shortly after in Werner et al. (2003), Adam et al. (2003), Kampes (2005), and Hooper et al. (2007). The goal of the approach is to identify and analyze point scatterers in a coregistered stack of SAR acquisitions which are characterized by marginal decorrelation during the time series of interest. They are referred to as permanent scatterers in the original approach and persistent scatterers (PSs) in most following works. The phase time series of these PSs, which is characterized by low phase noise, can be analyzed by means of time series analysis approaches. The goal of PSI is to estimate the displacement time series of PSs with the highest accuracy possible. Ferretti et al. (2007) showed that sub-millimeter accuracy is possible for PSs with high SCR when atmospheric noise is effectively removed.

The pre-processing of PSI includes the generation of the interferometric data stack. All available SAR acquisitions are coregistered onto a master acquisition. Subsequently, interferograms between the master and each slave are computed in order to derive an interferometric phase time series per pixel. The choice of the master is non-trivial, since noise in this acquisition can propagate into the coregistration procedure of the *slaves* and into the interferometric phases. For this reason, the master should minimize the sum decorrelation of all interferograms (Hooper et al., 2007). Another part of the pre-processing is the subtraction of known phase contributions, which are the flat Earth phase (Equation 2.20) and the topographic phase (Equation 2.23), which can be simulated on basis of an available DEM. Residual errors in the DEM remain in the interferometric phase and will be estimated later.

The main PSI procedure can be roughly divided into following steps:

   (i) selection of Persistent Scatterer Candidates (PSCs)

(ii) phase noise estimation for PSCs

(iii) selection of PSs

(iv) unwrapping

(v) estimation of spatially correlated signals

The single steps and differences in various approaches are described in the following. A review of different PSI approaches is found in Crosetto et al. (2015).

Selection of PS Candidates

PSs are point scatterers with low phase noise. In order to get an estimate of a pixel's phase noise, the different contributions in the interferometric phase of the pixel (Equation 2.18) have to be estimated and reduced. The phase noise estimate is then used to accept or reject a pixel as PS. The estimation of the phase noise is computationally expensive and needs long-wave phase contributions to be removed a-priori. The prior selection of PSCs can help to address both challenges. On the one hand, it considerably reduces the number of pixels to be tested for PS behavior, because it is expected that a superior number of pixels do not meet the requirements imposed on PS, depending on the study area on the used SAR sensor. On the other hand, the estimation of the long-wave phase contributions can be made more robust if a pre-selection of possibly stable pixels has been made. Lastly, the PSC selection can be used to establish a hierarchy of reliability levels among the selected pixels, as done in the Delft implementation of PSI (DePSI) algorithm (Leijen, 2014).

PSC selection methods are mainly based on amplitude statistics (Ferretti et al., 2001; Adam et al., 2005; Kampes, 2005). Ferretti et al. (2001) used in their original PSI approach the amplitude dispersion D_A as phase noise proxy. The phase standard deviation of a point scatterer with high SCR (Equation 2.13) can be approximated on basis of a stack of SAR scenes using the approximation

$$\sigma_\psi = \frac{\sigma}{\nu} \simeq \frac{\sigma_A}{\mu_A} = D_A, \qquad (3.1)$$

where σ_A and μ_A denote the standard deviation and mean of the amplitude of a pixel, respectively. The approximation of the phase noise by means of the amplitude dispersion is reasonable for point scatterers with high SCR. The amplitude dispersion approaches ~ 0.5 for low SCR, i.e., the estimation of the phase noise becomes less accurate with decreasing SCR (Ferretti et al., 2001), leading to a high false-positive PSCs selection rate for increasing D_A thresholds (Hooper et al., 2007).

Alternative exemplary PSC selection methods are based on the estimation of pixels' SCRs assuming equal clutter power in the pixel of interest and its surrounding pixels (Adam et al., 2005; Kampes, 2005), via maximum likelihood estimation of the Rice distribution parameters (Ansari et al., 2014) or maximum likelihood estimation of the SCR based on the interferometric phase PDF (Shanker and Zebker, 2007).

Phase Noise Estimation

After the PSI pre-processing, the interferometric phase of PSCs is the sum of various contributions:

$$\phi = W\left\{\varphi_h + \varphi_{\text{defo}} + \varphi_{\text{atmo}} + \varphi_{\text{orb}} + \varphi_{\text{noise}}\right\}, \tag{3.2}$$

where φ_h denotes the phase due to the residual height h of the pixel above the DEM used for the topographic phase reduction[1]. The goal is to estimate and split off each of the contributions but φ_{noise} in order to be able to classify a PSC as PS or non-PS.

The first step of the phase noise estimation is the subtraction of long-wave phase contributions. Various contributions of the interferometric phase are spatially correlated with different correlation lengths (see Section 2.3). Orbital errors are mostly visible as spatial trends in interferograms, i.e., have long correlation lengths (Fattahi and Amelung, 2014). Atmospheric disturbances are also spatially correlated, usually with correlation lengths assumed to reach up to kilometers (Hanssen, 2001; Hooper et al., 2007). Errors in DEMs are assumed to be partly spatially correlated as well (Hooper et al., 2007). Lastly, deformations of the Earth's surface can be spatially correlated, depending on the study area.

Potential differential movements on short spatial scales are considered either as signal of interest or noise in different PSI approaches. This distinction is one of the fundamental differences in PSI approaches and is handled depending on the study area and the research question. The Stanford Method for Persistent Scatterer Interferometry (StaMPS) algorithm proposed by Hooper et al. (2007) was designed to study spatially correlated deformation phenomena, and differential movements on short scales are considered as noise. Other approaches like the original PSI approach (Ferretti et al., 2001), DePSI (Kampes, 2005) or PSI-GENESIS by the German Aerospace Center (DLR) (Adam et al., 2003) do not assume all deformation of interest to be spatially correlated, and the uncorrelated deformation is not considered as noise. In this case, uncorrelated deformation has to be accounted for after the subtraction of long-wave phase contributions.

Two main approaches have been proposed to subtract spatially correlated phase contributions. Hooper and Zebker (2007) used an adaptive filter to split off spatially correlated phases, which is based on the filter presented in Goldstein and Werner (1998). The alternative approach is the calculation of phase differences between neighboring pixels, which is carried out along edges of a triangulation network (Ferretti et al., 2001; Adam et al., 2003; Kampes, 2005). Accounting for residual spatially uncorrelated deformation, the residual phase $\tilde{\phi}$ is

$$\tilde{\phi} = W\left\{\tilde{\phi}_h + \tilde{\phi}_{\text{defo}} + \phi_{\text{noise}}\right\}, \tag{3.3}$$

where $\tilde{\phi}$ denotes the spatially uncorrelated part of a phase contribution.

---

[1] In Section 2.3, we used the notation h for the height of a scatterer above the reference surface. We assume that the phase due to a reference DEM was subtracted in the PSI pre-processing and use, out of simplicity, the notation h for the height deviation of the scatterer from the reference DEM consistently in the following of this thesis.

The estimations of the residual phase contributions $\tilde{\phi}_h$ and $\tilde{\phi}_{\text{defo}}$ need the assumption of a functional model which describes the relationship of the residual height and deformation with the phase. The former is given in Equation 2.23, while the latter is often approximated by a linear model:

$$\phi_{\text{defo}} = \phi_v = -\frac{4\pi}{\lambda}\tau v, \tag{3.4}$$

where τ denotes the temporal baseline of an interferogram and v a linear displacement rate in LOS. The assumption is that the deformation model sufficiently describes the deformation time series. Model deficiencies lead to an overestimation of the phase noise and possibly a false rejection of PS. The use of more complex deformation models can help to decrease false negatives in the PS selection (Kampes, 2005; Van Leijen and Hanssen, 2007).

The additional consideration of phases due to thermally induced displacements ϕ_α as part of the deformation phase can improve the PS selection on infrastructure like bridges and skyscrapers when there are significant temperature differences at the acquisitions. Furthermore, it provides additional physical information on pixels (Monserrat et al., 2011; Fornaro et al., 2013). The related phase can also be described by a linear model

$$\phi_{\text{defo}} = \phi_v + \phi_\alpha,$$
$$\phi_\alpha = -\frac{4\pi}{\lambda}\vartheta\alpha, \tag{3.5}$$

where ϑ denotes the thermal baseline of an interferogram, i.e. the temperature difference at both acquisitions involved, and α the thermally induced displacement rate in LOS.

The estimation of the topographic and deformation phase, which are described by linear functional models, is non-linear since the phases are still wrapped module 2π. Various approaches to solve this nonlinear inversion have been proposed. Most of them are based on maximizing the objective function calculated from N interferometric phases

$$\gamma_\phi = \frac{1}{N}\left|\sum_{n=1}^{N}\exp\left\{i\left(\tilde{\phi} - \hat{\phi}_h - \hat{\phi}_{\text{defo}}\right)\right\}\right|, \tag{3.6}$$

where $\hat{\phi}_h$ and $\hat{\phi}_{\text{defo}}$ are the estimates of the topographic and deformation phase. Hooper et al. (2007) solved this problem with a rough grid search followed by a linear inversion around the maximum of the rough search. Spectral analysis methods also can be used to solve the inversion of the squared objective function, which is referred to as periodogram. The Fourier transform can be used for this purpose, however an equidistant spacing of the observations is needed for this. The singular value decomposition (SVD) can be applied to solve the inversion on irregularly spaced observations and was used in Fornaro et al. (2005), Zhu and Bamler (2010b), and Schenk (2015) in this context, while Zhu and Bamler (2010a) and Rebmeister et al. (2021) proposed compressive sensing approaches to solve the inversion. An alternative

approach for the parameter estimation is the use of the integer least-squares estimator (Teunissen, 1995), which was adapted for PSI in DePSI (Kampes and Hanssen, 2004) and PSI-GENESIS (Gernhardt, 2011).

After the parameter estimation, the phase contribution of the parameters are subtracted from the high-pass filtered phase observations to get the estimate of the phase noise

$$\hat{\phi}_{\text{noise}} = W \left\{ \tilde{\phi} - \hat{\phi}_h - \hat{\phi}_{\text{defo}} \right\}. \tag{3.7}$$

PS Selection

The noise estimate is used for the final selection of PSs. In Ferretti et al. (2001), a fixed phase coherence threshold T_γ was used to classify PSCs as PS or non-PS:

$$\gamma_\phi = \frac{1}{N} \left| \sum_{n=1}^{N} \exp\left(i\hat{\phi}_{\text{noise}}\right) \right| \underset{\text{non-PS}}{\overset{\text{PS}}{\gtrless}} T_\gamma. \tag{3.8}$$

Hooper et al. (2007) empirically determined variable thresholds for PSC bins with different amplitude dispersion values by analyzing the probability density of the phase coherence in the different bins. This way, points with high amplitude dispersion can be accepted as PSs even if their phase coherence is lower than that of PSs with low amplitude dispersion.

Phase Unwrapping

The goal of phase unwrapping after the PS selection is to solve the spatial and temporal phase ambiguity modulo 2π of the PSI interferogram stack. A requirement for correct unwrapping is that the phase difference between adjacent points in the spatial and temporal space is less than π, otherwise the point connection constitutes a discontinuity. For this reason, it is favorable to reduce all known phase contributions from the interferometric phases to get interferograms as smooth as possible. The task of an unwrapping algorithm is to identify residual discontinuities and find reasonable integration paths for the unwrapping. Many unwrapping algorithms have been proposed, ranging from sparse unwrapping (Ferretti et al., 2000) to interpolated unwrapping (Hooper et al., 2007) and from 2D+1D unwrapping (Hooper et al., 2004; Devanthéry et al., 2014) to advanced 3D unwrapping (Hooper and Zebker, 2007; Liu et al., 2020) using the full amount of observation information. Deep learning approaches have also been proposed to solve the unwrapping problem (Zhou et al., 2022).

Estimation of Spatially Correlated Noise

Phase disturbances affect the performance of PSI-based displacement monitoring, as described in Section 2.3. The impact of the various contributions increases with

increasing size of the study area, as a result of their limited spatial correlation and the acquisition geometry of SAR. Even if phase variations of the contributions are negligible across the study area, their absolute interferometric offsets can lead to phase ramps in ground range direction due to the mapping onto the local LOS, which is characterized by increasing incidence angle along the ground range direction.

In the original PSI approaches, spatially correlated nuisance terms were reduced from the unwrapped interferometric phase observations by means of spatio-temporal filters. Atmospheric and orbital errors are assumed to be spatially correlated while temporally uncorrelated. On the contrary, deformations are mostly assumed to be temporally correlated. By applying a combination of a temporal high-pass and a spatial low-pass filter, the spatially correlated noise (SCN) can be estimated and subsequently reduced from the interferometric phase observations.

A disadvantage of spatio-temporal filters for atmospheric phase estimation is the nontrivial selection of the filter parameters, which should be based on the statistical properties of the atmosphere (Gong et al., 2015). Furthermore, a filter of such kind is not able to estimate the tropospheric delays properly when the SAR sampling leads to aliasing of daily and seasonal tropospheric variations (Doin et al., 2009). Eventually, the temporal correlation length of atmospheric delays and displacements can overlap so that it is not possible to separate both signals by means of a temporal filter. As a consequence, alternative approaches have been proposed to account for different noise sources in InSAR and PSI. Examples are the estimation of the stratified atmosphere delay based on the correlation between interferometric phase observations and elevation (Wicks et al., 2002; Bekaert et al., 2015a; Murray et al., 2021) and using regional numerical weather models to model the atmospheric delay (Jolivet et al., 2011; Bekaert et al., 2015b; Yu et al., 2018). In the latter approaches, weather parameters which are influencing the radar propagation velocity are extracted from models like ERA-5 (Hersbach et al., 2020) to do a forward calculation of the delay. The parameters of interest are temperature, air pressure and parameters describing the water vapor content in the atmosphere. The performance of these methods is depending on the latitude of the study area, since the weather models can model water vapor variability better in high latitude than in low latitude areas (Cong et al., 2018). Furthermore, the methods perform worse in study areas with flat topography compared to mountainous areas (Liu et al., 2009).

Further SCN contributions are, for example, tidally induced displacements (Dicaprio and Simons, 2008; Parizzi et al., 2021) and ionospheric delays (Gomba et al., 2016; Liang et al., 2019). They are discussed in more detail in Section 4.4. In case that phase disturbances are modelled using auxiliary data, they can be subtracted prior to the phase unwrapping to increase the unwrapping performance.

Table 3.1.: Substitution of parameters and baselines for a uniform description of the one-dimensional parameter estimation problems [in M-SBAS]. © 2022 IEEE.

Parameter k^*	v	h	α
Baseline k	τ	$B_\perp$	ϑ
circular freq. $\omega^{(k)}$	$\frac{4\pi}{\lambda}\tau$	$\frac{4\pi}{\lambda \sin\theta \, r_0} B_\perp$	$\frac{4\pi}{\lambda}\vartheta$

3.2. Multi-Small-Baseline Subset Approach

The PSI approach which this work is based on is the M-SBAS approach described in Schenk (2015). This approach was designed as an efficient PSI approach which is characterized by a robust identification and parameter estimation of PSs in small, heterogeneous urban areas. The approach combines and extends elements of previously described PSI approaches, but is extraordinary in that it uses the fully overdetermined multi-master interferogram stack for a sequential parameter estimation instead of single-master interferograms for a simultaneous parameter estimation, as usually done in PSI. The approach covers only the steps (i) to (iii) of the standard PSI approach (Section 3.1), i.e., the steps from PSC selection to PS selection, and does not include phase unwrapping.

The PSC and PS selections in steps (i) and (iii) are realized by means of amplitude dispersion and temporal coherence thresholds, respectively. For step (ii), the approach considers the residual height h, the linear displacement rate v and the thermally induced displacement rate α of PSCs as parameters to be estimated. By estimating the displacement rate and including thermally induced displacements of single PSCs, it is designed for urban areas characterized by heterogeneous displacements on small scales. The parameters are estimated using the method of periodograms (Ferretti et al., 2001) by means of a truncated singular value decomposition inversion (Fornaro et al., 2005; Zhu and Bamler, 2010b). However, instead of estimating the parameters simultaneously, as usually done, they are estimated sequentially in M-SBAS to reduce the computational cost from O^3 to $3O$. The one-parameter periodograms can be expressed as

$$\gamma(k_r^*) = \frac{1}{N}\left|\sum_{n=1}^{N} \exp\left(j\tilde{\phi}\right)\exp\left(j\omega_n^{(k)}k_r^*\right)\right|^2, \tag{3.9}$$

where $\tilde{\phi}$ denotes the interferometric phases which have been adjusted for spatially correlated nuisance terms, k^* the particular parameter (h, v or α), k the parameter-specific baseline (spatial baseline $B_\perp$, temporal baseline τ or thermal baseline ϑ) and $\omega^{(k)}$ the circular-frequency describing the functional model between the parameter and the phase (see Table 3.1). The goal of the parameter estimation is to find the value k_0^* which maximizes the periodogram

$$k_0^* = \arg\max_r \gamma(k_r^*). \tag{3.10}$$

The problem of solving the parameter estimation sequentially is that the signal components which are not determined in the particular case are included in the

estimation as errors. The algorithm provides two approaches to tackle this problem and enable the sequential parameter estimation. The first approach is to exploit different small-baseline subsets of all available multi-master interferograms for each of the three parameter estimations. As an example, interferogram subsets which are characterized by a small variability in $B_\perp$ and ϑ are selected for the estimation of the displacement rate. In other words, one restricts the selection of interferograms to a connected subset in the τ-$B_\perp$-ϑ diagram. By restricting the selection to small-baseline interferograms, the algebraic correlation between the parameters is reduced for the sequential estimation. Since only the bandwidth of the baselines within the subsets is important and not their absolute position in the τ-$B_\perp$-ϑ diagram, it is possible to build several subsets for each parameter estimation, calculate the periodograms for each of them and stack the periodograms to increase the signal-to-noise ratio. As a result, all multi-master interferograms are exploited [...].

The second approach to correct residual errors in the sequential parameter estimation is the use of an iterative estimation procedure. In every step of the iteration, the three parameters are estimated. The index of the estimated parameter $\hat{k}^*$ is sought whose reduction from the phase observations maximizes the a-posteriori temporal phase coherence. The modelled phase due to the given parameter is reduced from the signal and the next iteration step is initiated. The estimated values of a parameter are cumulated if the correction of the given parameter maximizes the coherence in various iteration steps.

M-SBAS uses the averaged phase of reliable reference PSCs in each of the multi-master interferograms to split off the long-wave phase contributions prior to the parameter estimation. This averaged phase is referred to as reference phase in the following. The averaging allows for a fast computation of the reference phase for fully overdetermined multi-master interferogram stacks. On the other hand, this also leads to the fact the approach is only applicable to small study areas of few square-kilometers, as the single reference phase is incapable of capturing spatial variations in the atmosphere. In a first step, pixels with low amplitude dispersion are selected as reference PSCs and the reference phase of the interferogram formed by acquisitions n and m is estimated by complex averaging of the interferometric phase of K reference PSCs:

$$\hat{\phi}_{nm}^{\mathrm{ref}} = \arg\left\{\frac{1}{K}\sum_{k=1}^{K}\exp\left(i\phi_{nm}^{k}\right)\right\}. \tag{3.11}$$

The reference phases are subtracted from the particular interferograms. Subsequently, the parameters of the reference PSCs are estimated and the corresponding phase contributions subtracted from their phase observations. Reference PSCs with large parameter values are rejected and the adjusted phases of the remaining K reference pixels are used to recalculate the reference phase of the interferograms:

$$\hat{\phi}_{nm}^{\mathrm{ref}} = \arg\left\{\frac{1}{K}\sum_{k=1}^{K}\exp\left(i\left(\phi_{nm}^{k} - \phi_{\hat{h},nm}^{k} - \phi_{\hat{v},nm}^{k} - \phi_{\hat{\alpha},nm}^{k}\right)\right)\right\}. \tag{3.12}$$

The parameter estimation of all other PSCs is finally carried out after the subtraction of the refined reference phase.

Schenk (2015) tested the M-SBAS algorithm with a TerraSAR-X data set over a small urban area which was partly affected by large uplift movements during the acquisition of the data stack. The test also included a comparison with results from the StaMPS algorithm. The M-SBAS approach identified 36 % more stable PS pixels than StaMPS, while its processing time was only about 23 % of the processing time of StaMPS. Furthermore, the StaMPS analysis underestimated the uplift rates, contrary to the M-SBAS analysis, which was found in a comparison to levelling measurements. The underestimation of the displacement rates in StaMPS was traced back to the low-pass filtering of interferograms during the PSI analysis and inconsistencies in the phase unwrapping. This could be anticipated due to the fundamental differences in both PSI approaches. StaMPS was primary designed to study spatially correlated displacements. The main advantage of the approach is that no deformation model has to be assumed during the phase noise estimation process. On the other hand, considerable small-scale variations in the displacement field can lead to problems for the PS identification and phase unwrapping. The M-SBAS algorithm was designed to study displacement fields which are potentially characterized by large small-scale variations. A displacement model has to be assumed for the phase noise estimation in this case.

3.3. Developments and Potential Improvements in PSI and M-SBAS

Various improvements and extensions of the original PSI approaches have been proposed. An essential claim of many developments is an improved PS identification. Examples of modified PS selection approaches are the PS Pairs (Costantini et al., 2008), Quasi-PS (Perissin and Wang, 2012), Cousin-PS (Devanthéry et al., 2014) and phase similarity (Wang and Chen, 2022) methods as well as non-gaussian PS detectors (Huang and Zebker, 2022). Another approach to achieve an improved PS identification is based on polarimetric optimization in multi-polarized InSAR stacks (Navarro-Sanchez and Lopez-Sanchez, 2012; Sadeghi et al., 2018). Meanwhile, the use of deep learning also found its way into PSI and in particular the identification of PSs, as shown in Tiwari et al. (2020) and Aguiar et al. (2022).

Another PSI extension is the SAR tomography, which aims at reconstructing the reflectivity profile along the elevation axis of SAR acquisitions in order to enable the identification and analysis of multiple scatterers within resolution cells (Fornaro et al., 2005; Zhu et al., 2016; Rebmeister et al., 2021). This allows to produce very high-resolution 4-D point clouds and is especially relevant for applications in urban environments. DS approaches can also be considered as important extensions of PSI. The goal is to loosen the coherence requirement of pixels to be analyzed, in order to

include DSs into the time-series analysis. A short introduction on DS approaches was given in Section 2.5.

Challenging applications of PSI still exist. PSs can fade or appear in periods of the available SAR time series due to physical changes in the scene or changes in the acquisition geometry (Ferretti et al., 2004; Perissin and Ferretti, 2007). It can be assumed that the number of TPSs increases with increasing SAR time series as result of ongoing land surface changes, while the number of continuously coherent PSs decreases. It is desirable to include the analysis of such TPSs into PSI in order to develop flexible PSI systems which handle dynamic land surface changes, thus provide the best possible PSI-based geodetic measurement networks. This is especially important for long-term displacement monitoring, which is increasingly in demand in times of long-term SAR missions like Sentinel-1. TPS identification approaches were presented in Ferretti et al. (2004), Ansari et al. (2014), Dogan and Perissin (2014), and Hu et al. (2019), however none of these fully integrated TPSs into PSI including unwrapping. Furthermore, the mentioned approaches to identify TPSs and their coherent lifetime segments are solely based on amplitude statistics. It will be shown in Section 5.3 that the consideration of the interferometric phase improves the estimation of their coherent lifetime segments. The full integration of TPSs into PSI including phase unwrapping and a phase-based detection of their coherent lifetime segments will be the subject of Chapter 5.

Another main challenge of InSAR and PSI is large-scale monitoring in areas with complex atmospheric conditions. Spatially correlated phase noise has to be robustly estimated and subtracted to enable accurate displacement measurements at long distances. A promising approach of reducing long-wave phase disturbances including atmospheric noise is the fusion of InSAR with other geodetic measurements such as from GNSS networks. Various approaches have been proposed to reduce SCN in single interferograms (Argus et al., 2005; Lundgren et al., 2009; Neely et al., 2020) or in estimated displacement rates (Hooper et al., 2012; Parizzi et al., 2020) based on GNSS measurements. The methods are based on sampling the SCN at the GNSS stations and removing an interpolated noise screen from the observations. The reduction of SCN in single interferograms is essential to reduce the uncertainty in estimated displacement time series. None of the proposed methods to reduce SCN in single interferograms considers the spatial statistics of the noise for interpolation. A covariance-based integration of reference points into PSI to reduce SCN in interferograms will be presented in Section 4.5.

The PSI basis of the mentioned improvements is the M-SBAS algorithm. As stated before, the approach was designed for small-scale study areas and does not include phase unwrapping. For this reason, its extension to a full PSI approach which can be applied to large-scale problems and includes phase unwrapping will be described. The extensions developed for this purpose are described in Chapter 4.

4. Integrating M-SBAS into Robust Large-Scale PSI

This chapter covers modifications of M-SBAS which extend it to a full PSI approach which includes unwrapping and robustly handles large-scale displacement monitoring. At the beginning of the chapter, an improved estimation of long-wave phase contributions in multi-master interferograms of small spatial size is presented, which enables an enhanced coherence estimation and PS identification. This way, the applicability of M-SBAS is expanded to rural areas where only few PSs are located and areas which are characterized by largely heterogeneous displacements. Afterwards, large-scale M-SBAS is presented, which is based on running the algorithm in small spatial patches and merging the results afterwards. The phases and estimated parameters of identified PSs are imported into the StaMPS software environment (Hooper et al., 2007) to make use of its unwrapping algorithm. Phase noise contributions which are relevant for large-scale displacement monitoring are discussed and the modelling of the tropospheric delay, tidally induced displacements and plate motion is described. At the end of the chapter, a method to reduce residual SCN in interferograms is presented, based on a covariance-based integration of reference pixels with known displacement time series.

4.1. Reference Phase Adjustment

In M-SBAS, a single reference phase value is used in each of the multi-master interferograms to split off long-wave phase contributions, as described in Section 3.2. It is estimated by averaging the interferometric phase of automatically selected reference PSCs, as shown in Equation 3.12. Phase triangularity is expected to hold true in the multi-master stack for this averaged phase. However, the phase triangularity condition using the interferogram average is not true in reality when the reference phase is decorrelating due to diverging temporally correlated signals among the reference PSCs, such as diverging displacement rates. In this case, averaging is not an accurate estimate of the long-wave phase contributions in interferograms, leading to limited performance of the parameter and coherence estimation of PSCs. This is why it is desirable that reference pixels are selected which share similar displacement rates. However, this requirement cannot be ensured in heterogeneous study areas with largely heterogeneous displacements on small scales.
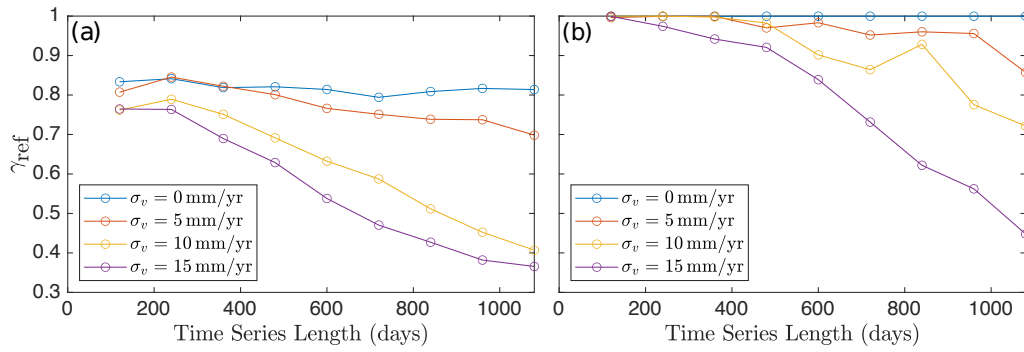
Figure 4.1.: Results of the reference phase estimation simulation study. (a) Differences between the true and estimated reference phases by complex averaging, described by means of the measure γ_{ref}, with regard to length of the considered time series and the standard deviation of the linear displacement rate σ_v of the reference PSCs. (b) Same as (a) with integer rounding adjusted reference phase estimation.

We illustrate the above problem by means of following simulation study. We simulated 2000 reference PSCs in a study area of $2 \times 2\,\mathrm{km}^2$, a radar wavelength of $5.5\,\mathrm{cm}$ and pixel size of $10 \times 10\,\mathrm{m}^2$. The atmospheric delay was simulated as temporally uncorrelated and spatially correlated with the power-law characteristics described in (Hanssen, 2001) using the software SyInteferoPy (Gaddes et al., 2019). The mean of the atmospheric delay was drawn from a uniform distribution in the range $[-\pi, \pi]$ for each SAR acquisition. We simulated reference PSCs with a SCR of 8 and their linear displacement rate was drawn from normal distributions with varying standard deviations σ_v for different simulation runs. Their height was drawn from a normal distribution with a standard deviation of $5\,\mathrm{m}$, and we used a typical perpendicular baseline distribution of Sentinel-1 SAR stacks. The number of simulated single look complexes (SLCs) with a revisit time of 6 days was changed for different simulation runs. We then compared the true interferogram average ϕ_{nm}^{ref} with the estimated reference phase $\hat{\phi}_{nm}^{\mathrm{ref}}$ for all $N(N-1)/2$ multi-master interferograms formed with N SAR acquisitions, using the following measure:

$$\gamma_{\mathrm{ref}} = \frac{2}{N(N-1)} \left| \sum_{n=1}^{N-1} \sum_{m=2, m>n}^{N} \exp\left(i\left(\phi_{nm}^{\mathrm{ref}} - \hat{\phi}_{nm}^{\mathrm{ref}}\right)\right) \right|. \tag{4.1}$$

The measure equals one for accurately estimated interferogram averages and decreases with increasingly false estimations. We carried out 20 simulation runs for each of the time series length and linear displacement rate settings. The medians of the measure γ_{ref} for the runs are shown in Figure 4.1(a). It is striking that the estimation error is considerable already for short time series lengths. This is due to individual phase noise of the reference PSCs as well as their displacement and height induced phases. For increasing time series length, the error stays approximately the same for the runs with all reference PSCs sharing the same displacement rate, while it increases for simulation runs with diverging displacement rates among them. Here, the error increases with increasing standard deviation of the displacement rates. The reason behind lies in

the increasingly decorrelated signals of the PSCs in wrapped interferograms with increasing temporal baselines. An approach to enhance the reference phase estimation is described in the following.

4.1.1. Integer Least-Squares Adjustment

We formulate the above-mentioned problem by stating that the expectation of the mean phase of an interferogram can be written as

$$E\left\{\hat{\phi}_{nm}^{\mathrm{ref}}\right\} = W\left\{\phi_{1m}^{\mathrm{ref}} - \phi_{1n}^{\mathrm{ref}}\right\}, \tag{4.2}$$

where the index 1 indicates the master acquisition. This condition is referred to as expected phase triangularity in an overdetermined interferogram network. The reference phases ϕ_{1n} can be inverted using the integer least-squares (ILS) approach (Teunissen, 1995). Subsequently, the multi-master reference phases can be re-calculated on the basis of ϕ_{1n}. The problem is an analogue to the single-master phase estimation of DS from multi-master interferometric phases described in Samiei-Esfahany et al. (2016). The following description and notation of the ILS inversion are based on that work.

An alternative notation of Equation 4.2 is given by introducing an integer ambiguity term d_{nm}:

$$E\left\{\hat{\phi}_{nm}^{\mathrm{ref}}\right\} = \begin{cases} \phi_{1m}^{\mathrm{ref}} - \phi_{1n}^{\mathrm{ref}} + d_{nm}(2\pi) & \text{if } n, m \neq 1 \\ \phi_{1m}^{\mathrm{ref}} & \text{if } n = 1 \\ -\phi_{1n}^{\mathrm{ref}} & \text{if } m = 1. \end{cases} \tag{4.3}$$

Since the ϕ terms are wrapped phases, the value of the phase differences is between -2π and 2π so that $d_{nm} \in \{-1, 0, 1\}$. This system of equations can be reformulated in matrix notation as

$$E\left\{\underbrace{\begin{bmatrix} \hat{\phi}_{12}^{\mathrm{ref}} \\ \vdots \\ \hat{\phi}_{1N}^{\mathrm{ref}} \\ \vdots \\ \hat{\phi}_{nm}^{\mathrm{ref}} \\ \vdots \end{bmatrix}}_{\mathbf{y}}\right\} = \underbrace{\begin{bmatrix} 0 & \cdots & 0 \\ \vdots & \ddots & \vdots \\ 0 & \cdots & 0 \\ 2\pi & & 0 \\ & \ddots & \\ 0 & & 2\pi \end{bmatrix}}_{D} \underbrace{\begin{bmatrix} \vdots \\ d_{nm} \\ \vdots \end{bmatrix}}_{\mathbf{d}} + \underbrace{\begin{bmatrix} 1 & & 0 \\ & \ddots & \\ 0 & & 1 \\ & \vdots & \\ & -1 \ldots 1 & \\ & \vdots & \end{bmatrix}}_{C} \underbrace{\begin{bmatrix} \phi_{12}^{\mathrm{ref}} \\ \vdots \\ \phi_{1N}^{\mathrm{ref}} \end{bmatrix}}_{\mathbf{c}}. \tag{4.4}$$

It is a hybrid system of linear equations with real unknowns ϕ_{1n} and integer unknowns d_{nm}. In the following, the integer ambiguity estimation to solve the problem is introduced. Comprehensive descriptions of ILS estimators are found, for example, in Teunissen (1995), Kampes (2005), and Leijen (2014). The idea of the ILS estimation is to decompose the objective function

$$\hat{\mathbf{d}}, \hat{\mathbf{c}} = \underset{\mathbf{d} \in \mathbb{Z}, \mathbf{c} \in \mathbb{R}}{\arg \min} \| \mathbf{y} - D\mathbf{d} - C\mathbf{c} \|_W^2 \tag{4.5}$$

into a sum of three L_2-norm components (Samiei-Esfahany et al., 2016)

$$\| \mathbf{y} - D\mathbf{d} - C\mathbf{c} \|_W^2 = \| \mathbf{y} - D\check{\mathbf{d}} - C\check{\mathbf{c}} \|_W^2 + \| \check{\mathbf{d}} - \mathbf{d} \|_{W_d}^2 + \| \check{\mathbf{c}}|_{\mathbf{d}} - \mathbf{c} \|_{W_c}^2 \qquad (4.6)$$

where $\check{\mathbf{c}}|_{\mathbf{d}}$ is the conditional least squares estimate of $\mathbf{c}$, conditioned on $\mathbf{d}$, and W is a weight matrix which can, for example, be defined as the inverse of the variance-covariance matrix of the observables. The weight matrices W_d and W_c are defined as

$$W_d = \bar{D}^T W \bar{D}, \text{ where } \bar{D} = D - C \left(C^T W C \right)^{-1} C^T W D,$$
$$W_c = C^T W C. \qquad (4.7)$$

The three problems are solved sequentially. The first component is solved using standard weighted least squares, ignoring the integer constraint of $\mathbf{d}$ and leading to so-called float solutions $\check{\mathbf{d}}$ and $\check{\mathbf{c}}$. The second component in Equation 4.6 is minimized by mapping the float solution of d to the nearest integer vector in the metric of matrix W_d to obtain $\hat{\mathbf{d}}$. Various mapping approaches exist which account for the correlations in W_d to different degrees. The integer rounding does not consider correlations in W_d at all, i.e. assumes W_d to be a diagonal matrix. The integer bootstrapping approach accounts for some correlations among the float solutions, while the ILS estimator accounts for all of them. However, the ILS problem cannot be solved directly so that the Least-squares Ambiguity Decorrelation Adjustment (LAMBDA) method by Teunissen et al. (1995) is a two-step ILS estimator. In the last step, the fixed solution of c is derived by calculating

$$\hat{\mathbf{c}} = \left(C^T W C \right)^{-1} C^T W \left(\mathbf{y} - D\hat{\mathbf{d}} \right). \qquad (4.8)$$

Since the matrix W_d is very close to diagonal in the given problem, we only tested integer rounding in the simulation. We used the following weights as diagonal elements in the weight matrix W:

$$w = \frac{2\hat{\gamma}_{nm}^2}{1 - \hat{\gamma}_{nm}^2}, \qquad (4.9)$$

adapted from the Fisher information index, which was suggested as weight in the ILS approach in Samiei-Esfahany et al. (2016). We estimated the coherence of the interferograms $\hat{\gamma}_{nm}$ assuming spatial stationarity among all reference PSCs. The results for the integer rounding derived reference phases in the simulation study for the two highest standard deviations of the displacement rates are shown in Figure 4.1(b). It can be seen that the reference phase estimation error for the integer rounding is negligible for short time series and consistently smaller compared to the complex phase averaging. As an example, the integer rounding based coherence measure is about 0.72 for a time series length of 1080 days and a displacement rate standard deviation of 10 mm/yr, compared to 0.41 for the phase averaging. For a large displacement rate standard deviation of 15 mm/yr, the integer rounding based results do not show much improvement for long time series compared to the phase averaging. This indicates
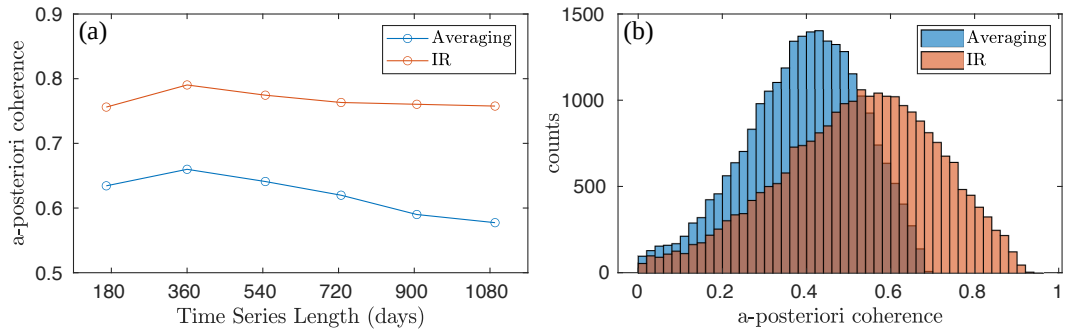
Figure 4.2.: (a) Comparison of the a-posteriori coherence of reference PSCs in a real data study based on Sentinel-1 data over the Vietnamese city of Can Tho for the complex averaging and integer rounding least squares adjustment (IR) of the reference phase for different time series lengths. (b) Comparison of the a-posteriori coherence histograms of all PSCs for both methods in the real data study with a time series length of three years.

a disability to reconstruct the reference phase by means of the integer rounding for largely decorrelated signals of reference PSCs, caused by the diverging displacement rates and long temporal baselines. However, such a large spread in the displacement rates within small study areas of few square kilometers is unlikely in reality.

4.1.2. Real Data Study

The improvement achieved by the presented reference phase adjustment was also studied with a real data set. We used Sentinel-1 data acquired over the Vietnamese city of Can Tho (Figure 6.1) with a study area size of about $5\,\mathrm{km}^2$. We applied the standard M-SBAS approach with phase averaging to estimate the reference phase of the interferograms as well as the modified approach with the integer rounding least squares adjustment of the reference phase. The a-posteriori phase coherence of the automatically selected reference PSCs was used as a measure to compare the results. It denotes the phase coherence after reduction of the reference phase and phases due to the estimated parameters from the observed interferometric phases. We compared the results for different time series lengths of up to three years, corresponding to 174 SAR scenes.

The results are displayed in Figure 4.2 (a). The integer rounding adjustment leads to increased coherence of PSCs already for a short time series of half a year compared to the phase averaging. Both results exhibit an increased coherence for a time series length of one year compared to half a year, which is probably caused by a more robust parameter estimation due to an increased amount of observations. The coherence for longer time series decreases for both methods, however the coherence approaches about 0.75 for the integer rounding while it steadily decreases for the phase averaging to be less than 0.58 for a time series length of three years. The standard deviation of the estimated displacement rate of the reference PSCs is about $8\,\mathrm{mm/yr}$, thus the

comparing results of the simulation study are represented by the red and yellow lines in Figure 4.1. The significant coherence difference, which is increasing with increasing time series length, was suggested by the simulation study. The a-posteriori coherence of all PSCs for a time series length of three years is compared for both methods in Figure 4.2 (b). Clearly, the overall coherence of all PSCs, not just the reference PSCs, is increased by means of the integer rounding based reference phase adjustment.

Concluding, the reference phase adjustment based on integer rounding least squares adjustment allows to enhance the estimation of the reference phases which are subtracted from interferograms to split off spatially long-wave phase contributions. The gain provided by the reference phase adjustment was illustrated in a simulation study and a real data study. The reference phase adjustment leads to increased a-posteriori coherences of PSCs in the real data study. This indicates that long-wave phase contributions are better estimated, leading to a more robust parameter and phase noise estimation of PSCs. As a result, the identification of PSs is considerably improved.

4.2. Large-Scale M-SBAS

The M-SBAS algorithm was designed for small-scale study areas. The reference phase is represented by a single value per interferogram to account for spatially long-wave phase contributions. This allows for a fast computation of the reference phase for multi-master interferogram stacks, but is only applicable to study areas of few square-kilometers in size.

In order to enable large-scale processing, the algorithm has to be adapted to sufficiently account for spatial undulations in the long-wave phase contributions, such as the atmosphere. This could be realized by implementing a spatial filter, as done in Hooper et al. (2007), or by studying phase differences between triangulated PSCs as done in Ferretti et al. (2001) and Kampes (2005). However, instead of changing the reference phase estimation, we keep the structure of the original M-SBAS approach and adapt it for large-scale problems in an alternative way. The study area is subdivided into small patches and the algorithm is run within each of these patches (Figure 4.3), as also done in Hou et al. (2021). An advantage of this approach is that the processing can be easily parallelized. A necessary step after running the algorithm in each patch is the spatial integration of the estimated parameters. The reason behind is that these only represent relative values with respect to the average of the reference PSs in each particular patch. Since we do not expect spatially correlated errors with large magnitudes in modern DEMs and also no spatially correlated thermally induced displacements, we here only integrate the estimated displacement rates. However, the height and thermally induced displacement rates could be integrated analogously to the method below. The estimated displacement rate of pixel i in patch a can be expressed as

$$v_i^a = v_i^{\text{total}} - v^{\text{ref,a}}, \tag{4.10}$$
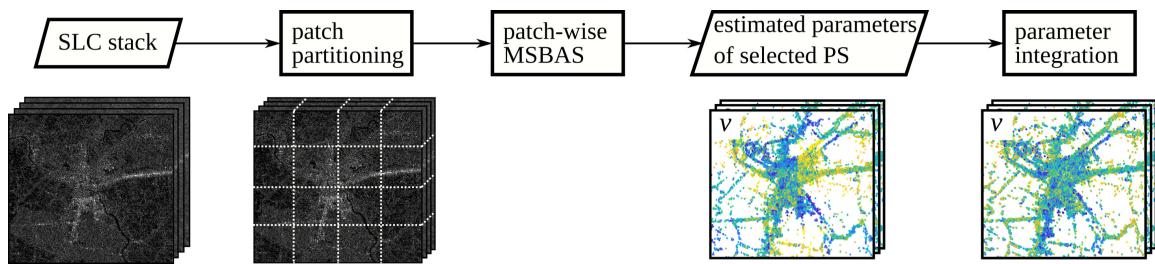
Figure 4.3.: Flowchart of large-scale M-SBAS. The study area is partitioned into small patches and M-SBAS is run separately in each patch. Afterwards, the estimated parameters linear displacement rates v, height h and thermally induced displacement rate α of identified PSs are integrated spatially.

where v_i^{total} denotes the total displacement rate of the pixel including spatially long-wave displacements and $v^{\text{ref,a}}$ the average total displacement rate of all reference PSs in patch a. The goal is to derive v_i^{total} by estimating and subtracting $v^{\text{a,ref}}$ from v_i^a. This is accomplished by estimating differences in v^{ref} in a network of connected patches and integrating them spatially by using the following weighted least-squares approach

$$\mathbf{v}^{\text{ref}} = \left(A^T W A \right)^{-1} A^T W \Delta \mathbf{v}^{\text{ref}}, \tag{4.11}$$

where $\mathbf{v}^{\text{ref}}$ denotes the vector containing the reference displacement rates of all patches, $\Delta \mathbf{v}^{\text{ref}}$ the vector which contains the differences in $\mathbf{v}^{\text{ref}}$ between connected patches and A the design matrix which describes the patch connections. W contains weights of the patch connections used for the integration. The integration is characterized by a datum deficiency, which we handle by solving the integrating with regard to an arbitrary patch. This means that v^{total} can only be estimated with a constant offset among all pixels. If there are reference pixels in the study area with ground truth displacement rates, the estimated rates can subsequently be adjusted with regard to these pixels. However, the goal of the integration is to remove discontinuities at patch boundaries, while the absolute value of the displacement rates is not relevant at this point. The modelled phases due to the estimated parameters are removed prior to the subsequent unwrapping to remove small-scale phase variations, thus improve the unwrapping performance. After the unwrapping, the phases are re-referenced to PSs with known displacement time series (Section 4.5.1) and the parameters are re-estimated with respect to these reference pixels.

There are different possibilities to estimate the differences in $\mathbf{v}^{\text{ref}}$ along the edges of patch connections. A simple approach would be to subdivide the study area into overlapping patches and calculate the averaged differences in estimated displacement rates at common PSs in the patch overlaps (Hou et al., 2021). However, various disadvantages characterize this approach. Pixels in the overlaps are examined multiple times by the PSI algorithm, leading to dispensable computational cost. Furthermore, the method does not work properly if there are disconnected patch groups without common overlap PSs, as visualized in Figure 4.4 (a). In that case, the integration
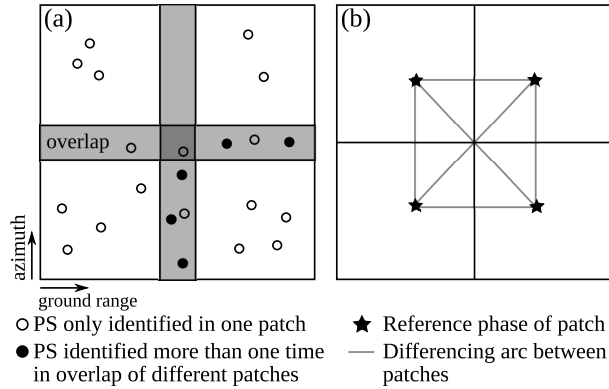
Figure 4.4.: Two possible approaches to estimate differences in displacement rates between neighboring patches, which are needed for the parameter integration in large-scale M-SBAS. (a) Difference estimation based on overlap PSs. The upper left patch does not have common overlap PSs with neighboring patches, leading to a rank deficiency in the integration problem. (b) Difference estimation based on differences in the patch reference phases. No overlap is needed in this case.

becomes a mixed-determined inversion problem (Tarantola, 2005) and has to be regularized with methods such as the truncated SVD or imposing a smoothness constraint (Jónsson et al., 2002).

We implemented an alternative approach to estimate $\Delta\mathbf{v}^{\mathrm{ref}}$ along patch connections, which is not depending on overlapping patches. The approach estimates the differences between patches on the basis of differences in their references phases, which have been used before in M-SBAS to split off the spatially long-wave phase contributions in interferograms (Sections 3.2 and 4.1). The reference phases are the averaged phases of all reference PSs, thus comprise the phases due to the averaged displacement rate of the reference PSs and overlaying stochastic noise. Consequently, the differences in the reference phases between connected patches contain phases due to differences in their $\mathbf{v}^{\mathrm{ref}}$. As a result, the differences in $\mathbf{v}^{\mathrm{ref}}$ between connected patches can be estimated analogous to the parameter estimation of single PSs in M-SBAS (Equations 3.9 and 3.10). The difference in the $\mathbf{v}^{\mathrm{ref}}$ between patches a and b, for example, is estimated based on N wrapped reference phase differences $\Delta\phi^{\mathrm{ref},a,b}$ using

$$\Delta v^{\mathrm{ref},a,b} = \arg\max_{v} \gamma(v), \ \text{with}$$

$$\gamma(v) = \frac{1}{N}\left|\sum_{n=1}^{N}\exp\left(j\Delta\phi^{\mathrm{ref},a,b}\right)\exp\left(j\frac{4\pi}{\lambda}\tau_n v\right)\right|^2. \tag{4.12}$$

The estimation is implemented analogously to the parameter estimation in M-SBAS, i.e., with dedicated small-baseline interferogram subsets. As a result, this approach represents a consistent modification of M-SBAS and was easily integrated into the algorithm. In practice, each patch is connected to its eight nearest patches and the differences in $\mathbf{v}^{\mathrm{ref}}$ along each edge are estimated. The a-posteriori coherence of the
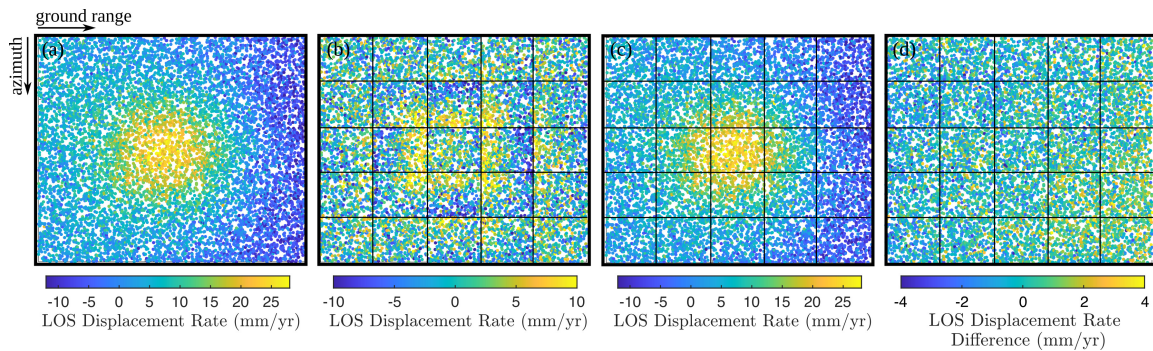
Figure 4.5.: Results of the large-scale M-SBAS simulation study. (a) Linear displacement field of 10000 simulated PSs in a study area of $10\,\text{km} \times 10\,\text{km}$. (b)-(c) Estimated linear displacement rates of identified PSs before and after the integration, respectively. The black lines represent the borders between separated patches. (d) Differences between estimated and true linear displacement rates.

residual reference phase differences along the edges are estimated and used as weights in the parameter integration.

We tested the proposed large-scale M-SBAS algorithm in a simulation study. We simulated 10000 PSs with SCR values between 1.5 and 10, whose occurrence was described by an exponential distribution, in an area of $10\,\text{km} \times 10\,\text{km}$ and 50 SAR scenes with a revisit time of 6 days. The sensor and acquisition characteristics of the Sentinel-1 mission were realized, i.e., a radar wavelength of $5.5\,\text{cm}$ and a pixel size of $2\,\text{m}$ in ground range and $14\,\text{m}$ in azimuth. As for the simulation study in Section 4.1, the tropospheric delay was simulated as spatially correlated with the power-law characteristics described in (Hanssen, 2001) using the software SyInteferoPy by Gaddes et al. (2019). The mean of the tropospheric delay was drawn from a uniform distribution in the range $[-\pi, \pi]$ for each SAR acquisition. We only studied the identification of PSs and the estimation and integration of the estimated linear displacement rate. For this purpose, a linear displacement field was simulated which is characterized by a blob with large displacement rates of up to $30\,\text{mm/yr}$ in the center of the scene, an overlaying spatial trend as well as small individual deviations at each PS (Figure 4.5 (a)). No heights and thermally induced displacement rates were simulated. The results of large-scale M-SBAS applied to the simulated data are displayed in Figure 4.5. The patch size was set to $2\,\text{km} \times 2\,\text{km}$, resulting in 25 patches. More than 97 % of the simulated PSs were identified by the algorithm. The overlooked PSs were the ones with the lowest simulated SCR. The estimated linear displacement rates featured large discontinuities at the patch borders prior to the integration, which were removed after the parameter integration. The estimated displacement field represents a reasonable estimation of the true simulated displacement field. The differences between true and estimated displacement field are normally distributed with a standard deviation of $1.6\,\text{mm/yr}$ and feature a slight spatial trend. The spatial trend in the differences was caused by incidental temporal correlations in the simulated tropospheric delays. As stated before, long-wave residuals are not diminishing the

performance of the method at this point because they do not affect the unwrapping. They are estimated and reduced after the unwrapping (Sections 4.4 and 4.5).

4.3. M-SBAS-2-StaMPS

The M-SBAS algorithm does not include phase unwrapping of identified PSs. In most geoscientific cases, however, it is preferable to estimate their full displacement time series instead of only displacement rates. This enables the study of the temporal evolution and nonlinear displacements. We extended the algorithm to a full PSI algorithm, including phase unwrapping, by integrating it into the StaMPS software environment. This is why the adapted algorithm is referred to as M-SBAS-2-StaMPS.

The first part of M-SBAS-2-StaMPS is the data import of the M-SBAS results into the StaMPS software environment. The data import was implemented in the way that no StaMPS functions had to be adapted. The estimated parameters of the selected PSs and additional metadata of the data stack and the PSs are saved into the StaMPS *Matlab* format. Additionally, the complex interferometric measurements of the PSs are saved in a *Matlab* file. The interferogram network, which is used from this point on, can be selected freely, e.g. as single-master network or small-baseline network with specific baseline thresholds. The master acquisition is selected to be the scene with the lowest estimated mean phase variance, which is estimated at the end of the original M-SBAS approach in each patch. After the M-SBAS import into StaMPS, the full functionality of StaMPS is available. This also includes StaMPS add-ons like the Toolbox for Reducing Atmospheric InSAR Noise (TRAIN) toolbox (Bekaert et al., 2015b) which features various tropospheric correction methods.

StaMPS provides different two- and three-dimensional unwrapping approaches, which are described in Hooper et al. (2004) and Hooper and Zebker (2007). The default unwrapping algorithm for PS time series is a stepwise three-dimensional unwrapping algorithm which first unwraps the data in the time dimension and subsequently optimizes the initial unwrapping solution in the two spatial dimensions. The spatial unwrapping makes use of the Statistical-Cost, Network-Flow Algorithm for Phase Unwrapping (SNAPHU) which was described in Chen and Zebker (2001). The phases have to be gridded onto a regular grid prior to the phase unwrapping with SNAPHU.

It is preferable to reduce spatially uncorrelated phase contributions from the interferometric observations prior to unwrapping in order to spatially smooth the phases to be unwrapped, thus improve the unwrapping performance. The phase contribution can be added back after unwrapping for a final parameter estimation. The different assumption of the spatial correlation length of displacements is one of the fundamental differences between M-SBAS and StaMPS. In StaMPS, spatial correlation in displacements is assumed, so only the residual height of PSs is estimated and reduced prior to unwrapping. In contrast, displacements are not required to be spatially correlated in M-SBAS and linear displacement rates of PSs are estimated. We implemented the reduction of the phases due to all estimated parameters in M-SBAS, i.e., the residual
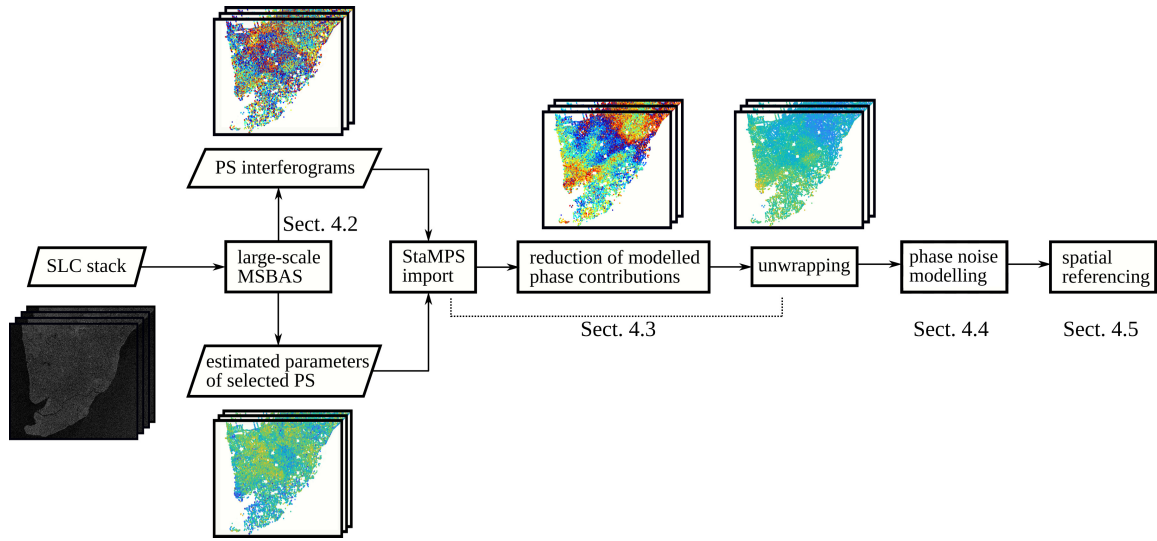
Figure 4.6.: Flowchart of the proposed M-SBAS-2-StaMPS algorithm.

height, linear displacement rate and thermally induced displacement rate, prior to the phase unwrapping. The residual phase ϕ_{res} is

$$\phi_{\text{res}} = W\left\{\phi - \hat{\phi}_h - \hat{\phi}_v - \hat{\phi}_\alpha\right\} = W\left\{\phi_{\text{nlin}} + \phi_{\text{atmo}} + \phi_{\text{orb}} + \phi_{\text{noise}}\right\}, \qquad (4.13)$$

where ϕ_{nlin} denotes the phase due to nonlinear displacements. The phase due to the estimated linear displacement rate is added back after the unwrapping to have the full displacement time series of PSs.

In the following sections, two approaches to decrease the uncertainty of the unwrapped displacement time series in large-scale applications are covered. This first consists of the modelling of different large-scale phase noise contributions and secondly of a covariance-based reference integration method for the estimation of residual SCN. The flowchart of the full approach is displayed in Figure 4.6.

4.4. Modelling of Phase Noise

Phase noise affects the performance of InSAR-based displacement monitoring [, as described in Section 2.3 and 3.1]. Relevant SCN contributions are tropospheric and ionospheric delays [...], orbital errors [...] and surface displacements which are not the target in the specific displacement monitoring. The latter include tidally induced displacements [...], plate motions [...] and possibly displacements due to atmospheric pressure loading and pole tides. Even if phase variations of these effects are negligible across the studied area, their absolute offsets in interferograms can lead to significant phase ramps in ground range direction due to the mapping onto the local LOS.

We implemented the modelling of three phase noise terms in addition to the existing functionality in StaMPS. They include an improved tropospheric delay modelling based on the ERA-5 weather reanalysis, as well as the consideration of tidally induced

displacements and tectonic plate motions. They are described in the following subsections. The estimation of orbital errors is not considered as their impact for MT-InSAR has significantly decreased for new satellite missions like Sentinel-1 and TerraSAR-X, compared to older missions, due to more precise orbit measurements with on-board GPS receivers. Fattahi and Amelung (2014) reported maximum orbital uncertainties of $0.5\,\mathrm{mm/yr}\,100\,\mathrm{km}^{-1}$ for TerraSAR-X and Sentinel-1. We also do not consider the displacement signal due to atmospheric pressure loading and pole tides, as we expect these to be insignificant for PSI. Ionospheric effects are also not estimated here, even though they can have a significant impact on C-band and longer-wavelength SAR interferometry. Liang et al. (2019) showed that ionospheric effects on MT-InSAR can be strong for ascending data acquired in low-latitude areas, while descending data is largely unaffected. They mainly lead to long-wave phase trends, which can reach up to several phase cycles over hundreds of kilometers. They can also lead to spatial ramps in the estimated velocity field in the order of few mm/yr as result of temporal correlations. Methods to account for the ionosphere are the range split-spectrum method (Rosen et al., 2010; Gomba et al., 2016) and modelling based on TEC maps (Eineder et al., 2011; Yunjun et al., 2022). The estimation of ionospheric effects is the subject of future work. In this thesis, all unconsidered or insufficiently modelled phase noise terms are summarized as residual noise and considered later in our strategy to reduce residual SCN, described in Section 4.5.

4.4.1. Tropospheric Delay

The application of spatio-temporal filters to reduce SCN, which is mainly induced by the tropospheric delay, has been replaced more and more by alternative methods. The reasons behind are described in Section 3.1. The StaMPS add-on toolbox TRAIN contains alternative state-of-the-art correction methods which are compared in Bekaert et al. (2015b). It includes the correction of tropospheric delays based on numerical weather models, spectrometer observations if available and phase-based approaches assuming linear or power-law relationships between the phase and topography in the study area.

The tropospheric delay modelling in TRAIN based on numerical weather models is developed on integrating the modelled tropospheric phase delay along the zenith path from the surface and back-projecting the integrated value onto the local LOS. The assumption behind this simplified approach is that the troposphere is isotropic, which is expected to be not always the case. For this reason, we implemented the method proposed by Hu and Mallorquí (2019) which integrates the modelled delay along the actual LOS of the satellite, avoiding modelling errors by anisotropic tropospheric features. For this purpose, the weather parameters temperature T, partial pressure of dry air P and water vapor partial pressure e from the ERA-5 reanalysis are interpolated onto integration points along the LOS path. The two-way tropospheric delay is then modelled using the expression

$$\psi_{\mathrm{atmo}} = \frac{-4\pi}{\lambda}10^{-6}\int_{\mathbf{r}_{\mathrm{surf}}}^{\mathbf{r}_{\mathrm{sat}}} n(\mathbf{r})d\mathbf{r} = \frac{-4\pi}{\lambda}10^{-6}\int_{\mathbf{r}_{\mathrm{surf}}}^{\mathbf{r}_{\mathrm{sat}}} k_1\frac{P}{T} + k_2\frac{e}{T} + k_3\frac{e}{T^2}d\mathbf{r}, \qquad (4.14)$$

where $k_1 = 0.776\,\mathrm{KPa^{-1}}$, $k_2 = 0.716\,\mathrm{KPa^{-1}}$, $k_3 = 3750\,\mathrm{K^2Pa^{-1}}$, $\mathbf{r}_\mathrm{surf}$ the location of a pixel on the Earth's surface and $\mathbf{r}_\mathrm{sat}$ the satellite location. In practice, the integration is only performed up to a maximum altitude which affects the relative tropospheric phase delay. It is usually set to a maximum altitude of $30\,\mathrm{km}$ (Hu and Mallorquí, 2019). After the integration, the interferometric delays are computed by subtracting the delays from master and slave scenes. Hu and Mallorquí (2019) showed that their proposed method improves the performance of the delay modelling based on numerical weather models, especially in areas with large topography gradients.

4.4.2. Tidally Induced Displacements

Tides are caused by gravitational forces of the moon and sun as well as orbiting-induced forces. Solid earth tides (SETs) describe the resulting elastic deformation of the solid Earth's surface, while ocean tides describe the water redistribution of the oceans. Ocean tides do not have direct impact on InSAR, but the mass redistribution also leads to deformations of the solid Earth's surface. This effect, which is strongest in coastal areas, is called ocean tide loading (OTL). Both considered effects can have an impact on InSAR analyses, depending on the location and the size of the study area (Dicaprio and Simons, 2008; Parizzi et al., 2021; Peng et al., 2020).

We implemented a phase correction method to account for both considered kinds of tidally induced displacements. The SET and OTL induced displacements in the interferograms are modelled based on the programs *solid* (Milbert, 2018) and *SPOTL* (Agnew, 2012), respectively. The modelled 3D tidal displacements $\mathbf{d}^\mathrm{tide}$ are projected onto LOS of the SAR satellite, described by the LOS unit vector $\mathbf{e}_\mathrm{los}$

$$d^\mathrm{tide,los} = \mathbf{d}^\mathrm{tide} \cdot \mathbf{e}_\mathrm{los}, \tag{4.15}$$

converted to phase and finally removed from the interferograms.

4.4.3. Tectonic Plate Motions

Earth's tectonic plates are characterized by rigid motion which can be described by a rotation about a pole, called Euler pole, with angular rotation rates in the order of a degree per million years (Bullard et al., 1965; D. P. McKenzie and R. L. Parker, 1967). The resulting plate velocity varies over large SAR swaths due to varying distances to the pole. As for the tidally induced displacements, the projection of the velocities onto the LOS leads to additional phase ramps in interferograms along the ground range direction, even if the velocity variations within a swath are small. Bähr et al. (2012) and Stephenson et al. (2022) showed that plate motions can lead to spatial ramps in InSAR-derived velocity fields of several millimeters per year over hundreds of kilometers. As we are interested in intraplate displacements, we consider this signal as noise and want to subtract it from the InSAR observations.

The interferometric phases due to plate motion can be modelled using Euler pole information from the International Terrestrial Reference Frame 2014 plate motion

model (Altamimi et al., 2017) or the NNR-MORVEL56 model by Argus et al. (2011), for example. The linear velocity vector $\mathbf{v}_p(\mathbf{r})$ due to plate motion at any point $\mathbf{r}$ on a plate can be derived as (Stephenson et al., 2022)

$$\mathbf{v}_p(\mathbf{r}) = \omega \times \mathbf{r}, \tag{4.16}$$

where ω denotes the angular velocity vector in the Earth-centered, Earth-fixed reference frame and $\times$ the cross product. This velocity vector is transformed into the local east-north-up system at $\mathbf{r}$, projected onto the LOS of the satellite and finally used to calculate and subtract interferometric phases.

4.5. Reference Integration for Spatially Correlated Noise Estimation

Residual SCN persists in interferograms due to insufficient noise modelling and unconsidered noise signals. The former can be due to the limited performance of numerical weather models based tropospheric delay modelling, which is depending on the location of the study area (Liu et al., 2009; Cong et al., 2018). It decreases with decreasing latitude, decreasing topography in the study area and increasing proximity to the coast due to higher water vapor content and variability in the atmosphere.Unconsidered noise signals have been listed in Section 4.4.

Various strategies have been proposed to account for SCN in interferograms or estimated displacement fields. One approach is to fit and subtract linear or quadratic spatial functions (Pritchard et al., 2002; Fournier et al., 2011), but this is not applicable if large-scale displacements are of interest. Alternatively, ground truth or reference displacement measurements such as from GNSS can be exploited to constrain the noise (Argus et al., 2005; Lundgren et al., 2009; Parizzi et al., 2020; Neely et al., 2020; Xu et al., 2021; Liu et al., 2022). The idea is to sample the SCN at the reference pixels with known displacement time series, interpolate it onto the PS locations and subtract the interpolated noise screen from the observations. In Argus et al. (2005), Neely et al. (2020), and Liu et al. (2022), the sampled SCN in interferograms is interpolated using surface fitting, while nearest neighbor interpolation is used in Xu et al. (2021). We adapt the general approach by interpolating the noise, taking its spatial statistics into account. The approach shares the basic idea of the covariance-based InSAR and GNSS fusion method presented in Parizzi et al. (2020). Their method, however, is used to calibrate estimated displacement rates with GNSS measurements, taking the spatial statistics of the displacement rate error into account. Our approach aims at reducing SCN in single interferograms, thus reducing the uncertainty in derived PS displacement time series. In the following, we assume that a phase-to-displacement conversion has already been carried out in the interferograms.
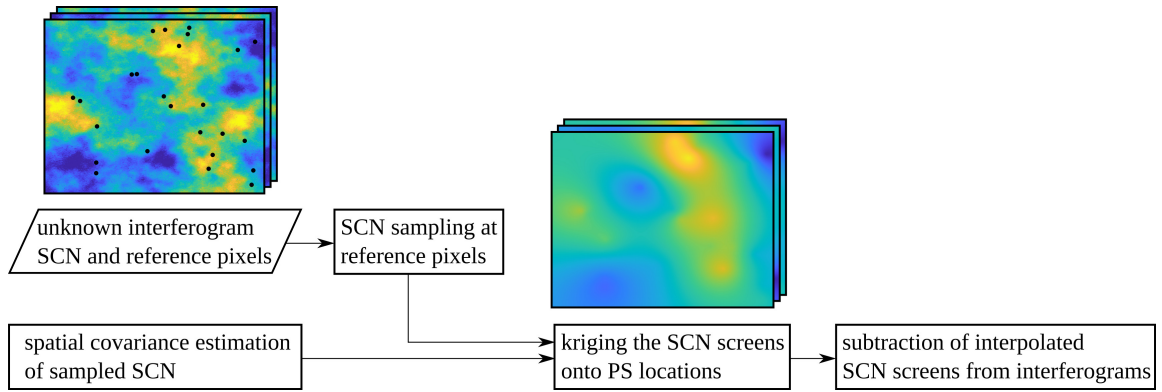
Figure 4.7.: Flowchart of the reference integration for residual SCN noise estimation in interferograms.

4.5.1. Method Description

As introduced in Section 2.5, reference pixels are necessary in InSAR in the first place to resolve the unknown phase ambiguity of interferograms. In the standard approaches, the displacement of one reference pixel or the average of several is subtracted from the interferograms, leading to relative displacements with regard to these reference pixels (Hooper et al., 2007). This is why it is desirable to select reference pixels which are presumably stable in the study period or whose displacement time series has been estimated a-priori by means of alternative geodetic methods such as GNSS. In the latter case, the InSAR estimates can be transformed into an absolute terrestrial reference frame using datum connection (Mahapatra et al., 2018). In case that there are several reference pixels with ground truth (or assumed) displacement time series and distributed across the study area, they can be exploited to estimate the residual SCN screen in interferograms.

The flowchart of our proposed method to correct for residual SCN in single interferograms is displayed in Figure 4.7. The first step is to sample the unknown interferogram SCN at reference pixels with known displacement time series. The ground truth displacement d_{nk}^{gt} of reference PS k in an interferogram n can be computed by subtracting the PS's ground truth position $\mathbf{r}_k(t)$ at the involved acquisitions t_{n0} and t_{n1} and projecting it onto the LOS of the SAR satellite:

$$d_{nk}^{\text{gt}} = [\mathbf{r}_k(t_{n0}) - \mathbf{r}_k(t_{n1})] \cdot \mathbf{e}_{\text{los}}. \tag{4.17}$$

The SCN screen r_{nk} in the interferogram can then be sampled by calculating the residuals between the ground truth displacement and the interferogram LOS displacement d_{nk}^{PSI} at that position:

$$r_{nk} = d_{nk}^{\text{PSI}} - d_{nk}^{\text{gt}}. \tag{4.18}$$

In case of GNSS stations used as reference, the residuals are commonly calculated between their displacement and the mean displacement of PSs located in a radius around. If presumably stable regions are selected as reference, it is assumed that $d_{nk}^{\text{gt}} = 0$, thus that the interferogram observations of PSs located in these regions equal

the residual SCN. The unevenly sampled SCN is then interpolated, taking its spatial statistics into account, in order to get an estimate of the SCN screen $\hat{r}_n$ at each PS location. The variance-covariance matrix C_{ref} of the sampled SCN at K reference pixels has to be estimated for this purpose, which is defined as

$$C_{\text{ref}} = \text{diag}\left\{\sigma_{\text{gt},1}^2, ..., \sigma_{\text{gt},K}^2\right\} + \text{diag}\left\{\sigma_{\text{PSI},1}^2, ..., \sigma_{\text{PSI},K}^2\right\} + C_{\text{scn}}\left(\mathbf{x}_{\text{ref}}, \mathbf{x}_{\text{ref}}\right), \qquad (4.19)$$

where $\sigma_{\text{gt},k}^2$ and $\sigma_{\text{PSI},k}^2$ denote the variances of the ground truth and PSI derived displacements, respectively, and C_{scn} the covariance of the SCN at the reference PSs $\mathbf{x}_{\text{ref}}$. We implicitly assume in this definition that the variances σ_{gt}^2 and σ_{PSI}^2 are independent and not spatially correlated. The ground truth variance depends on which kind of reference is used. In case of GNSS stations being used as reference, the ground truth variance σ_{gt}^2 is the variance of their displacement estimates. In contrast, the ground truth variance can be assumed to be zero if regions are selected as reference which are presumably stable during the study period. The variance of the PSI derived displacements of the reference PSs used to calculate the residuals between the ground truth and the PSI results (Equation 4.18) can be estimated by means of their estimated temporal coherence [, e.g. by applying Equation 2.31].

The covariance estimation of the residual SCN is carried out under the assumption of spatial stationarity after the subtraction of modelled tropospheric delays and tidally induced displacements. The same assumption was also made in Gonzalez et al. (2018) and Parizzi et al. (2020). In this case, the covariance matrix $C_{\text{scn}}(i, j)$ is only depending on the distance Δ_{ij} between PS pixels i and j

$$C_{\text{scn}}(i, j) = C_{\text{scn}}(\Delta_{ij}), \qquad (4.20)$$

and can be described by the variogram $\Gamma(\Delta_{ij})$. In general, the number and spatial distribution of reference pixels across the study area are too poor for a robust estimation of the SCN variograms. Instead, we average variograms between all available PS pixels in many interferograms with small temporal baselines. The average variogram is automatically fitted with a variogram model, which represents the mean covariance of the SCN in all interferograms. Interferograms with small temporal baselines are used to minimize displacement induced phases of examined PS pixels which do not belong to the set of reference pixels. The residual SCN is expected to be on the order of the magnitude of a centimeter, thus to constitute the dominant signal in such small-baseline interferograms. For the short revisit times of modern SAR satellites, which are down to six days in case of Sentinel-1, displacement rates would have to reach several decimeters per year to affect the variogram calculation of the SCN (Parizzi et al., 2020). The impact of potential high-magnitude displacement events on short time scales is suppressed by averaging variograms of several interferograms.

The sampled SCN can be interpolated onto the PS locations using ordinary kriging as soon as its variance-covariance matrix has been estimated. The kriging method is, however, referred to as error cokriging since the measurement variances of the sampled SCN are considered in C_{ref} (Chilès and Delfiner, 2012; Chilès and Desassis, 2018). The goal of the kriging interpolation is to invert the weights of the sampled

SCN at each reference PS for the interpolation at each other PS location, taking its variance-covariance matrix into account. We refer to the locations to be interpolated as query points. The kriging system for the interpolation at query point x_0 is given by:

$$(C_{\text{ref}} - \mu \mathcal{I}) \, \mathbf{w} = C_{\text{scn}} \, (\mathbf{x}_{\text{ref}}, x_0)$$
$$\sum_{k=1}^{K} w_k = 1, \tag{4.21}$$

where μ denotes the Lagrange multiplier, $\mathcal{I}$ the identity matrix, $\mathbf{w}$ the weight vector for the interpolation at pixel x_0 and $C_{\text{scn}} \, (\mathbf{x}_{\text{ref}}, x_0)$ the covariance model evaluated at the distances between all reference PS pixels $\mathbf{x}_{\text{ref}}$ and x_0. The Lagrange multiplier and the weights are simultaneously inverted by means of a least-squares inversion.

The interpolation is a linear combination of the weighted sampled SCN

$$\hat{r}_n(x_0) = \sum_{k=1}^{K} w_k r_{nk}. \tag{4.22}$$

The interpolated SCN screen $\hat{r}_n$ is finally subtracted from the interferograms to get the adjusted displacements $d_n^{\text{PSI,adj}}$:

$$d_n^{\text{PSI,adj}} = d_n^{\text{PSI}} - \hat{r}_n. \tag{4.23}$$

One of the advantages of the proposed method, besides considering the spatial statistics during interpolation, is that the prediction variance-covariance of the interpolation is known. The variance is given by

$$\sigma_{\text{ck}}^2(x_0) = E \left\{ (r_n(x_0) - \hat{r}_n(x_0))^2 \right\} = \mu + C_{\text{scn}}(0) - \mathbf{w}^T C_{\text{scn}} \, (\mathbf{x}_{\text{ref}}, x_0) \tag{4.24}$$

and depends on the location of x_0 with regard to the reference pixels, the covariance of the SCN and the variances of the sampled SCN. For increasing measurement variances $\sigma_{\text{gt}}^2 + \sigma_{\text{PSI}}^2$ at all reference pixels with regard to the covariance of the SCN, the weights of the reference pixels increasingly align at each query point. In the special case that the measurement variance is similar at all sample points and much larger than the covariances of the SCN, the interpolation approaches the mean of all K samples with estimation variance $(\sigma_{\text{gt}}^2 + \sigma_{\text{PSI}}^2)/K$ at each query point.

The prediction covariance between query points x_0 and x_1 with weight vectors $\mathbf{w_0}$ and $\mathbf{w_1}$ and Lagrange multipliers μ_0 and μ_1 is

$$C_{\text{ck}}(x_0, x_1) = E \left\{ [r_n(x_0) - \hat{r}_n(x_0)] \, [r_n(x_1) - \hat{r}_n(x_1)] \right\}$$
$$= \mu_1 + C_{\text{scn}}(\Delta_{x_0 x_1}) - \mathbf{w_1}^T C_{\text{scn}} \, (\mathbf{x}_{\text{ref}}, x_0) \tag{4.25}$$
$$= \mu_0 + C_{\text{scn}}(\Delta_{x_0 x_1}) - \mathbf{w_0}^T C_{\text{scn}} \, (\mathbf{x}_{\text{ref}}, x_1) \, .$$

The equation elucidates that the residual noise in interferograms after subtraction of the interpolated SCN screens $\hat{r}_n$ is no longer stationary, but has a covariance which

is depending on the particular location of the considered pixels with regard to the reference PSs.

The consideration of the uncertainty propagation of the sampled SCN in the proposed referencing method allows to give an approximation of the final covariance matrix of the PSI derived displacement results of all L pixels:

$$\hat{C}_{\text{final}} = \text{diag} \left\{ \sigma^2_{\text{PSI},1}, ..., \sigma^2_{\text{PSI},L} \right\} + C_{\text{ck}} \tag{4.26}$$

where C_{ck} is the prediction variance-covariance matrix of the error cokriging. We refer to the diagonal of this matrix as the estimated displacement variance $\hat{\sigma}^2_d = \sigma^2_{\text{PSI}} + \sigma^2_{\text{ck}}$. The variances σ^2_{PSI} could again be approximated based on the estimated coherence of the pixels, for example. However, it has to be kept in mind that phase deviations from the functional model assumed in the PSI phase noise estimation step [(Section 3.1)] lead to inaccuracies in the coherence estimation. Further inaccuracies in $\hat{C}_{\text{final}}$ are unconsidered unwrapping errors, a falsely assumed stationarity of the residual SCN and insufficient modelling of the spatial covariance based on the mean variogram of small-baseline interferograms.

In case that displacement rates v are estimated by means of a least-squares inversion, the variance of the displacement estimation can be used to derive the variance of the rate estimation σ^2_v for each pixel using the following expression:

$$\hat{\sigma}^2_v = \left(A^T \hat{\sigma}^{-2}_d A \right)^{-1}, \tag{4.27}$$

where A denotes the design matrix of the inversion which contains the temporal baselines of the interferogram network. Note that no temporal covariance is estimated and included in the stochastic model. The variance of the displacement rate estimation is underestimated when temporal correlations persist in the residual SCN.

4.5.2. Simulation Study

We conducted a simulation study to test the applicability and performance of the proposed method. We simulated randomly distributed PSs characterized by variable phase noise in 30 interferograms covering an area of $100 \, \text{km} \times 100 \, \text{km}$. The wavelength was set to $5.5 \, \text{cm}$ in order to simulate a C-band SAR system like Sentinel-1. The atmospheric delay was again simulated as temporally uncorrelated and spatially correlated with the power-law characteristics described in Hanssen (2001) with a standard deviation of $3 \, \text{cm}$ at the longest wavelengths, using the software SyInteferoPy (Gaddes et al., 2019). No displacements were simulated in the interferograms.

An example of a simulated interferogram is displayed in Figure 4.8 (a). It mainly consists of spatially correlated atmospheric noise with amplitudes of up to $3 \, \text{cm}$ and to a much smaller degree of individual pixel noise. The single variograms and the mean variogram of the simulated interferograms are plotted in Figure 4.8 (b). The single variograms are characterized by increasing variogram values with increasing distances
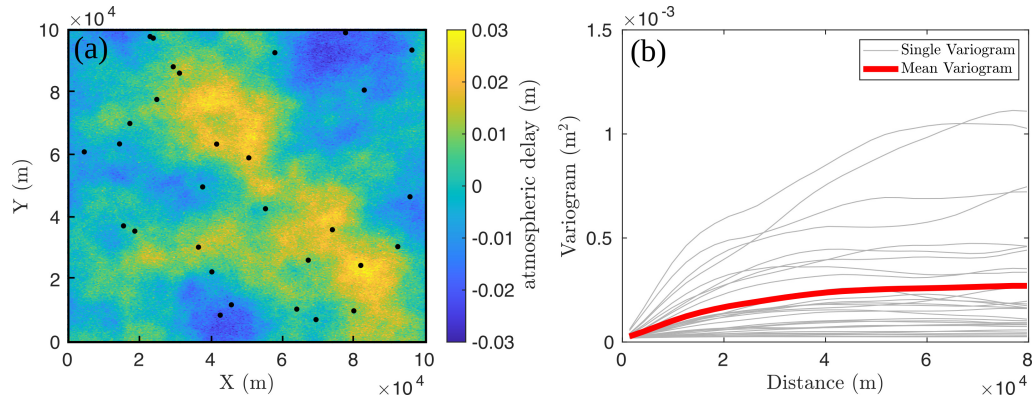
Figure 4.8.: (a) Example of a simulated interferogram mainly consisting of spatially correlated atmospheric noise. The black dots represent the reference PSs used for the SCN interpolation example shown in Figure 4.9. (b) Single variograms and mean variogram of the interferograms of the simulation study in Section 4.5.2.

and almost all asymptotically approach a flat level which is usually referred to as sill. The mean variogram represents the estimated average covariance characteristics of the interferogram noise, even if there are variograms with much higher values at all distances. As stated before, we want to reduce the impact of possible short-time displacements with high amplitudes in practice by averaging variograms of small-baseline interferograms.

An exemplary set of interpolations of the sampled SCN in the interferogram in Figure 4.8 (a) and the associated prediction variances are displayed in Figure 4.9 for different ground truth variance scenarios. The results in Figure 4.9 (a)/(d) and (b)/(e) are based on the interpolation of the sampled SCN with the ground truth variance of all reference pixels set to $\sigma_{\mathrm{gt}}^2 = 0$ and $\sigma_{\mathrm{gt}}^2 = 1\,\mathrm{cm}^2$, respectively. The subfigures (c)/(f) display the results of the last interpolation run when the ground truth variance was set to $\sigma_{\mathrm{gt}}^2 = 2\,\mathrm{cm}^2$ for half of the reference pixels and $0\,\mathrm{cm}^2$ for the others. The interpolation results in (a) are a proper prediction of the true atmosphere in Figure 4.8 based on the set of reference PSs. The prediction variance is overall low and obviously lowest in the vicinity of references. The interpolation results in (b) represent a worse prediction, which is smoothed compared to the results in (a). The prediction variance is overall larger compared to those in (d), also in the vicinity of the reference PSs. The reason behind is the large ground truth variance at all reference PSs which leads to similar interpolation weights of all references at each query location, i.e. an interpolation result similar to the mean of the sampled SCN. The results of the last simulation run represent a combination of the former two. The interpolation results represent a good prediction of the true simulated atmosphere near the reference PSs with zero ground truth variance, whereas they are strongly smoothed in the southern part of the study area where a large ground truth variance of the reference PSs was simulated. This is also visible in the prediction variance, which is low near the reference PSs with zero ground truth variance and large in the southern part of the area.

47
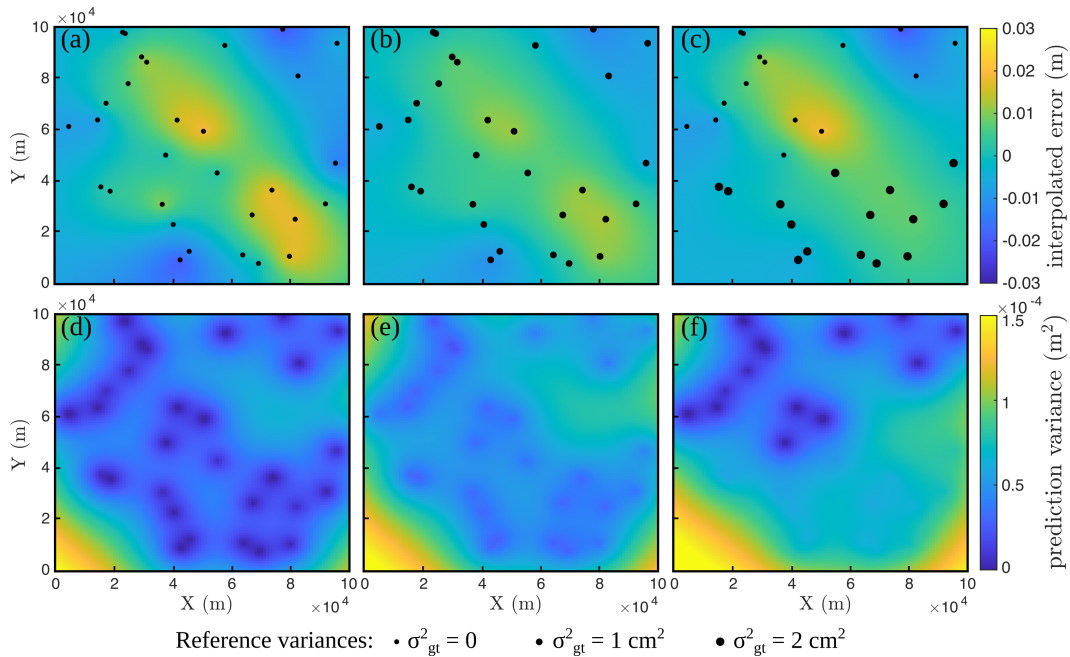
Figure 4.9.: (a)-(c) Interpolated SCN of the simulated interferogram shown in Figure 4.8 with different ground truth variance scenarios. The size of the black dots indicates the ground truth variance of the particular reference pixel. (d)-(f) Prediction variances of the scenarios in (a)-(c).

In order to compare the proposed method to existing referencing methods, we calculated the root-mean-square error (RMSE) of the different predictions of the SCN in the interferograms as function of the number of reference PSs and two ground truth variance scenarios. The referencing methods are: referencing to the sampled SCN at a single reference PSs, to the mean sampled SCN, referencing based on quadratic polynomial surface fitting of the sampled SCN (Neely et al., 2020) and our proposed referencing method using error cokriging interpolation. The ground truth variances were simulated as $\sigma^2_{\mathrm{gt}} = 0$ and $\sigma^2_{\mathrm{gt}} = 1\,\mathrm{cm}^2$ for all reference PSs in the two scenarios. The results are displayed in Figure 4.10. The RMSE is largest for the single PS referencing in both scenarios. The RMSE of the mean referencing is approximately 9.5 mm in both scenarios and for all tested numbers of reference PSs. The RMSE of the surface fit is large for a small number of reference PSs but decreases with increasing number of reference points and approaches about 8 mm in both scenarios. The RMSE of our proposed method is lowest in both scenarios. It decreases to less than 5 mm and about 6 mm, respectively, at a reference PS number of 120, corresponding to an improvement of 40 % and 25 % compared to the surface fitting approach. It can be seen that the RMSE of our proposed method is increased in the second scenario, since the ground truth variance of all reference PSs is in the same order as the covariances of the SCN at large distances. As stated before, the kriging interpolation approaches the mean with increasing ground truth variances of all reference PSs.
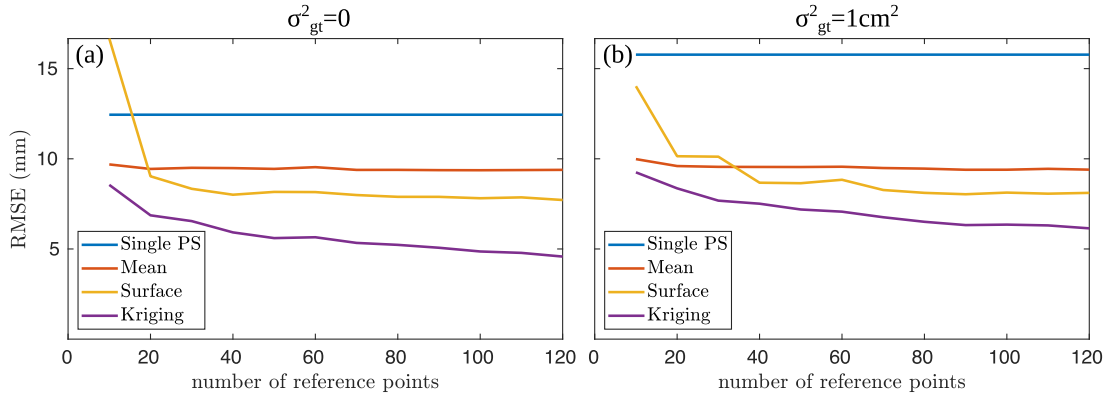
Figure 4.10.: (a) Comparison of the RMSE of the SCN prediction in all simulated interferograms for different referencing methods as function of the number of reference PSs and a ground truth variance of $\sigma^2_{\mathrm{gt}} = 0$ for all reference PSs. (b) Same as (a) with $\sigma^2_{\mathrm{gt}} = 1\,\mathrm{cm}^2$ for all reference PSs. The referencing methods are referencing to the sampled SCN at a single reference PS (Sinlge PS), to the mean sampled SCN (Mean), referencing based on quadratic polynomial surface fitting of the sampled SCN (Neely et al., 2020) (Surface) and our proposed referencing method based on kriging interpolation (Kriging).

The proposed referencing method shows a superior performance in the simulation study with regard to the compared referencing methods. In the following, a real data study is carried out to test and compare the proposed method with a real Sentinel-1 SAR data stack.

4.5.3. Real Data Study

For the real data study, we used 30 Sentinel-1 SAR scenes acquired in ascending orbit over the northwestern part of the Vietnamese Mekong Delta (Figure 6.1 (b)). The study area is about $100\,\mathrm{km}{\times}80\,\mathrm{km}$ and characterized by several large solid rock outcrops being embedded in the sedimentary delta. We applied the M-SBAS-2-StaMPS algorithm to the data stack and corrected the interferograms for modelled tidal displacements and tropospheric delays (Section 4.4). Variograms of LOS phases, which were converted to displacements in interferograms with short temporal baselines, before and after the correction are displayed in Figure 4.11. It can be seen that variogram values at large distances are reduced in some interferograms, but the mean variogram is not improved considerably at most distances. It is $5.8\,\mathrm{cm}^2$ and $5.56\,\mathrm{cm}^2$ at $80\,\mathrm{km}$ without and with correction, respectively. There is a considerable variogram gain provided by the corrections at larger distances so that the mean variogram is $8.2\,\mathrm{cm}^2$ and $5.9\,\mathrm{cm}^2$ at $90\,\mathrm{km}$, respectively. Still, the corrections do not reduce the uncertainty at large distances to a reasonable magnitude. The reason behind is probably a low performance of the atmospheric delay modelling based on the ERA-5 model due to the low-latitude location of the study area, direct connection to the sea and flat topography, leading to a high water vapor variability in the troposphere.
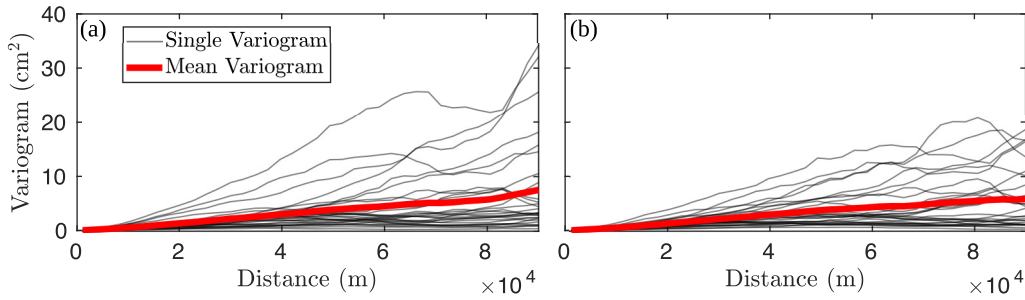
Figure 4.11.: Empirical variograms of interferograms with short temporal baselines, described in Section 4.5.3, prior to (a) and after (b) correction of modelled tidal and atmospheric noise.

We compared our proposed method to reduce residual SCN in the interferograms with the mean and surface referencing methods. For this purpose, we assumed that the solid rock outcrops are stable in the considered time series and selected PSs on them as reference PSs with presumably zero displacements $d^{\text{gt}}(t) = 0$ and zero ground truth variance $\sigma^2_{\text{gt}} = 0$. The spatial distribution of reference pixels was good in north-south direction, while quite bad in east-west direction as a result of the location of the solid rock outcrops. Variograms of interferograms with short temporal baselines after applying the different methods were used for comparison. However, as the residuals are no longer stationary after referencing (see Section 4.5.1), we only calculated variograms between pairs of non-reference and reference PSs to get a measure of the residual SCN as a function of the distance to reference PSs. The single and mean variograms are displayed in Figure 4.12. The mean variogram after referencing to the mean sampled SCN is $6.6\,\text{cm}^2$ at 90 km, while there are single variograms reaching up to $31\,\text{cm}^2$ at large distances. The variograms after referencing based on quadratic polynomial surface fitting of the sampled SCN(Neely et al., 2020) are on average increased at most distances, compared to the variograms after referencing to the sampled mean, and feature a hole effect, i.e. non-monotonic behavior. The mean variogram approaches $9.3\,\text{cm}^2$ at 90 km, while there are single variograms reaching up to $67\,\text{cm}^2$ at large distances. The mean variogram after applying our proposed referencing method approaches about $2\,\text{cm}^2$ at large distances, with single variograms reaching up to $8.1\,\text{cm}^2$.

In order to provide a proper quantitative comparison of the surface fitting and our approach with regard to referencing to the mean sampled SCN, we use the mean variogram gain from Parizzi et al. (2021)

$$G(\Delta) = 10 \log_{10} \left(\frac{\bar{\Gamma}(\Delta)}{\bar{\Gamma}_{\text{ref}}(\Delta)} \right), \tag{4.28}$$

where $\bar{\Gamma}(\Delta)$ is the mean variogram at distance Δ after applying one of both former methods and $\bar{\Gamma}_{\text{ref}}$ the reference variogram which is in this case the mean variogram after referencing to the mean sampled SCN. The mean variogram gain for the surface fitting undulates between -1.5 and 4 dB but is positive at most distances. This indicates a worse performance of the referencing based on quadratic polynomial surface fitting
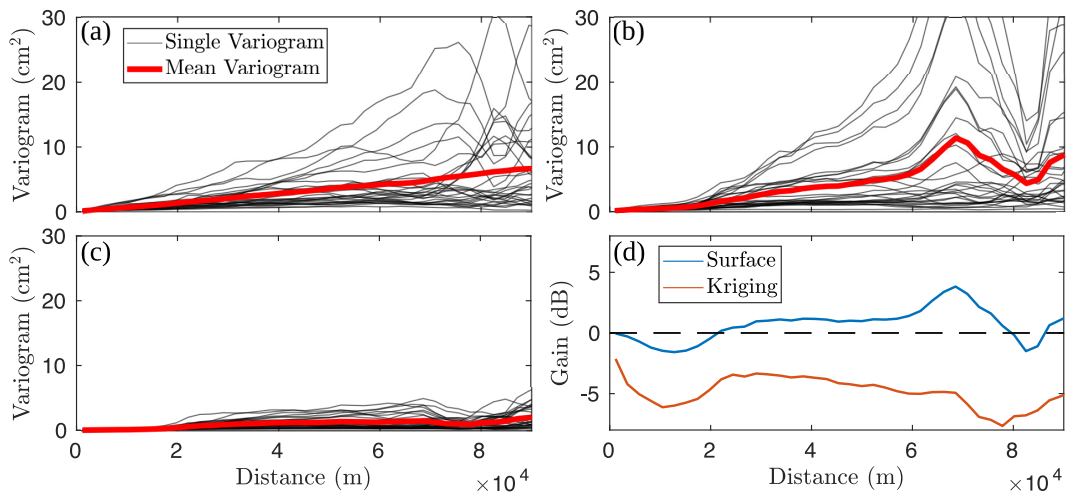
Figure 4.12.: Single and mean empirical variograms for pairs of non-reference and reference PSs after interferogram referencing based on (a) the mean sampled SCN, (b) quadratic polynomial surface fitting of the sampled SCN (Neely et al., 2020) and (c) our proposed kriging interpolation. (d) Mean variogram gains of (b) and (c) with respect to (a).

compared to referencing to the mean sampled SCN in the real data study. The reason behind is probably the modest spatial distribution of the reference PSs across the study area, leading to a bad conditioning of the quadratic polynomial fit. The mean variogram gain of our proposed method is consistently negative with a negative trend, reaching its minimum pf $-7.6\,\mathrm{dB}$ at $78\,\mathrm{km}$. This indicates a superior performance of our proposed method over the compared ones.

Residual SCN in interferograms might not only be spatially correlated but also temporally correlated, propagating into the estimation of displacement rates of PSs. In order to study this, we compared the RMSE of the estimated displacement rates at reference PSs in the solid rock outcrops, which are presumably stable in the study period, for the different methods. It is $2.8\,\mathrm{mm/yr}$ for referencing to the mean sampled SCN, $2.1\,\mathrm{mm/yr}$ for the surface fitting approach and $1.4\,\mathrm{mm/yr}$ for our proposed approach. Consequently, there is indeed residual SCN in the interferograms which is not only spatially but temporally correlated and most effectively mitigated by our approach. The proposed method leads to reduced uncertainty in the displacement time series of PSs and to a correction of noise in the estimated displacement rates as well.

4.6. Conclusion

In this chapter, extensions of M-SBAS were presented which integrate the approach into robust large-scale PSI. At the beginning of the chapter, an improved estimation of long-wave phase contributions in multi-master interferograms of small spatial size was presented. We showed on the basis of a simulation and a real data study that

the proposed method improves the estimation of long-wave phase contributions in interferograms considerably up to a standard deviation of the displacement rates of reference PSs of 15 mm/yr. The latter scenario is unlikely to occur in real applications with study area sizes of few square-kilometer. The coherence estimation of PSCs is significantly improved by means of the proposed method, thus the PS identification. This way, the applicability of the approach is extended to areas which are characterized by diverging displacements and to rural areas where only few PSs are located in.

Subsequently, the expansion of M-SBAS to large-scale areas was described, which is based on running the algorithm in small spatial patches and merging the results afterwards. Integrating the estimated displacement rates spatially across all patches is necessary for the latter step. The integration is implemented as a weighted least-squares adjustment in a network of connected patches. For this purpose, the displacement differences along the connecting edges have to be determined, which is carried out on the basis of the interferogram reference phases, which represent long-wave phase contributions of the patches. We tested the proposed large-scale M-SBAS algorithm in a simulation study. Nearly all simulated PSs were identified, and the simulated displacement field could be properly estimated.

An essential part of full PSI approaches which are applied for geoscientific research is phase unwrapping, which is necessary to derive displacement time series of identified PSs. The original M-SBAS approach was developed to study small-scale urban displacements and did not include phase unwrapping. We extended M-SBAS into a full PSI approach by integrating the results into the StaMPS framework to make use of its unwrapping algorithm.

At the end of the chapter, the focus was put on the minimization of SCN in interferograms, which is especially relevant for large-scale displacement monitoring. The SCN is the sum of various contributions. We implemented the subtraction of modelled phase noise due to tropospheric delays, tidally induced displacements and tectonic plate motions. The estimation and subtraction of ionospheric delays was not considered in this thesis and is the subject of future work. Afterwards, a covariance-based integration method of reference pixels with known displacement time series to estimate residual SCN in interferograms was proposed. The method is based on sampling the residual SCN at the reference pixels and interpolating it onto the PS locations. Error cokriging is applied for the interpolation, which considers the spatial covariance of the sampled SCN. We compared the proposed method to alternative methods, which aim at reducing SCNs by integrating reference pixels, in a simulation and a real data study. Our proposed method showed superior performance of reducing residual SCN over the compared methods in both studies. An additional advantage of the method is that the prediction (co)variance of the interpolation is provided, which can be used to estimate the final subsidence time series (co)variance. A requirement for proper performances of the method is a good distribution of reference pixels across the study area.

5. Fully Integrated Temporary Persistent Scatterer Interferometry

Physical changes of the land surface and changes in the acquisition geometry can cause PSs to fade or appear in periods of the available SAR time series (Ferretti et al., 2004; Perissin and Ferretti, 2007). Such scatterers are referred to as TPSs which are coherent in one or several segments of the time series. Simulated amplitude and phase time series of different kinds of TPSs are displayed in Figure 5.1. Fading TPSs fade during the considered SAR time series, which could be caused by a teardown of a building, while the construction of buildings on formerly natural surfaces can trigger appearing TPSs. Visiting TPSs appear and fade during the time series, whereas recurring TPSs repeatedly appear and fade, or vice versa. The latter could be periodically inundated PSs in coastal and recurringly flooded areas.

It is desirable to integrate TPSs into PSI algorithms in order to establish flexible displacement measurement systems which are able to handle land surface changes during the time series, thus provide the best possible PSI-based measurement point networks. It can be assumed that the number of TPSs increases with increasing time series length as result of ongoing land surface changes, while the number of continuously coherent PSs decreases. For this reason, the integration of TPSs into PSI is a necessary add-on of PSI for long-term and continuous displacement monitoring, which is increasingly in demand in times of SAR missions which were designed for long-term operations, such as Sentinel-1.

In this chapter, the full integration of TPSs into the M-SBAS-2-StaMPS algorithm is presented. The detection of TPSs and their change dates is based on the approach by Hu et al. (2019). Subsequently, the initially estimated change dates are iteratively refined during the phase noise estimation process, using a newly developed phase-based change detection method. The phases of identified PSs and TPSs are jointly unwrapped in a modified version of the unwrapping algorithm in StaMPS. At the end, the temporal datum of those TPSs has to be re-defined whose coherent lifetime does not cover the selected master scene. The proposed method is tested with a Sentinel-1 data stack acquired over city of Ca Mau, which is located in the VMD (see Figure 6.1) and affected by considerable land subsidence. The high construction activity in the VMD makes the city a suitable test area for studying TPSs. At the end of the chapter, the relevance of the TPS integration for long-term monitoring is examined by analyzing the ratio of identified numbers of TPSs to PSs in Sentinel-1 time series as a function of the covered time series length in two urban and two rural areas in the VMD. Furthermore, the lifetime of identified TPSs is analyzed to study their actual
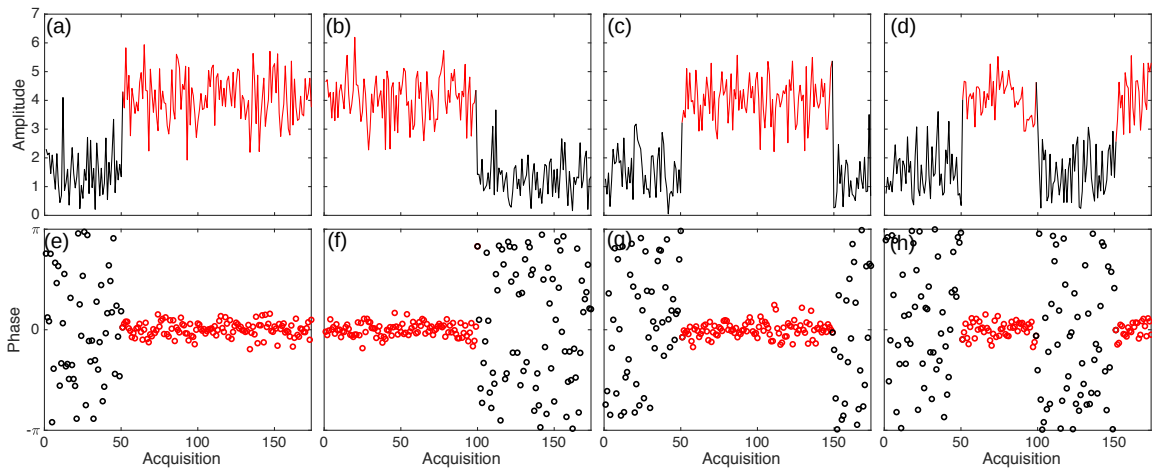
Figure 5.1.: Simulated amplitude (a-d) and phase (e-h) time series of different types of TPS: (a), (e) appearing TPS, (b), (f) fading TPS, (c), (g) visiting TPS, (d), (h) recurring TPS. The red parts of the time series mark the coherent periods of the pixels. © 2022 IEEE.

contribution to the geodetic observation network. This chapter includes material which was published in Dörr et al. (2022a), marked in blue, and Dörr et al. (2022b), marked in green.

5.1. Related Work

The identification of the coherent interval(s) of TPSs can be described as a change point estimation problem. The change point estimation of Temporary Persistent Scatterer Candidates (TPSCs) is a crucial part of incorporating TPSs into PSI algorithms because it should be avoided to include noisy interferometric phase observations into the parameter and coherence estimation. Various approaches have been proposed to identify the coherent interval(s) of TPSCs based on the SAR amplitude and/or phase. The motivation of using solely the amplitude time series is the assumption that abrupt changes in the phase of a pixel correspond to abrupt changes in its amplitude (Ferretti et al., 2004; Perissin and Ferretti, 2007). Compared to coherence analyses, amplitude analyses do not depend on additional error-prone processing steps and are computationally faster. Ferretti et al. (2004) applied a Bayesian step detector assuming Gaussian statistics for the amplitude returns. Brcic and Adam (2013) presented different parametric change point estimators for TPSs and concluded that the Gaussian maximum-likelihood estimator was the most suitable among the considered estimators regarding performance and speed. Ansari et al. (2014) used a Bayesian TPS identification and change point estimation assuming that DS and PS periods in amplitude time series follow Rayleigh and Rice distributions, respectively. Dogan and Perissin (2014) detected change points in the TPS amplitude time series using the analysis of variance (ANOVA) technique. Hu et al. (2019) applied a χ^2-test for TPS identification and a stepwise F-test for change point estimation under the

assumption that the DS and PS periods are characterized by significantly different Rayleigh distribution parameters. The proposed F-Test showed more robust results compared to ANOVA. A coherent change detection for PS and DS considering amplitude and phase was presented in Monti-Guarnieri et al. (2018). Yang and Soergel (2018) identified TPSs and their change date by splitting the time series in different subsets, running a PSI algorithm for these and examining the differences in phase coherence between the subsets. Zhang et al. (2011) chose an image-pair based method in which they identify TPSs by means of pixel offset statistics.

The purpose of identifying TPSs and their change points includes change detection (Ansari et al., 2014; Yang and Soergel, 2018; Monti-Guarnieri et al., 2018) and increasing the PS density for displacement monitoring (Hu et al., 2019). For the latter, the incorporation of TPSs into a PSI algorithm is necessary. Hu et al. (2019) presented a method of incorporating TPSs into the integer least-squares algorithm DePSI (Kampes and Hanssen, 2004) to jointly estimate the linear displacement rate of PSs and TPSs. To our knowledge, there has not been any publication on incorporating TPSs into a PSI approach [... including] unwrapping to receive displacement time series.

5.2. TPS Detection

The TPS detection approach and initial change point estimation used in this work was proposed by Hu et al. (2019) who test if parts of the amplitude time series of SAR pixels can be described by different Rayleigh distributions. Even though the amplitude of PSs can be best described by Rice distributions, it still is expected that the amplitudes of incoherent and coherent periods of TPSs can be described by Rayleigh distributions with significantly different Rayleigh parameters. Additionally, the change point estimation of Rayleigh parameters within a time series is much faster and less complex than identifying multiple segments following different Rice and Rayleigh distributions within a time series, because the parameter estimation of the Rice distribution is very costly (Brcic and Adam, 2013). The PDF of the Rayleigh distribution is [... given in Equation 2.5]. The unbiased estimator of σ^2 for an amplitude time series with M independent observations is

$$\hat{\sigma}^2 = \frac{1}{2M} \sum_{m=1}^{M} A_m^2. \tag{5.1}$$

Hu et al. (2019) use a sequential F-test to find change points in a time series which separate segments following different Rayleigh distributions. Given a pixel's time series of length M, the approach successively tests each acquisition m as a potential change point. The null hypothesis H_0 is tested that the two segments follow the same Rayleigh distribution against the alternative hypothesis H_1 that they follow different Rayleigh distributions. Under the null hypothesis, the ratio of the scale parameters F follows a central F-distribution with $2m$ and $2M - 2m$ degrees of freedom. This is used
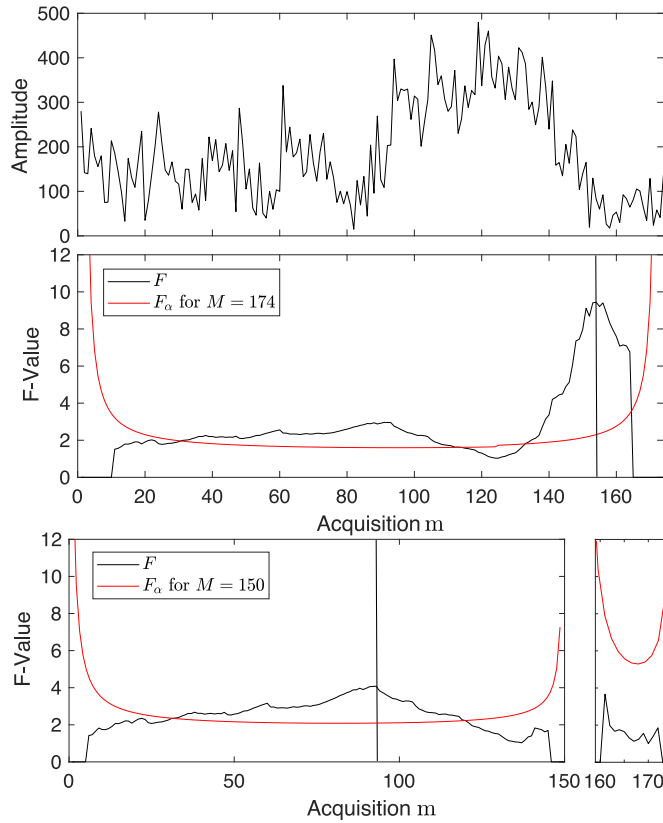
Figure 5.2.: Change point detection of a Sentinel-1 SAR pixel. (a) Normalized amplitude time series. (b) F-Test for the whole time series with the threshold shown as red line. A change point is identified and the time series is separated at that point into two segments. (c) and (d) F-Test for the two segments. Another change point is identified in the first segment. The last part of the change point estimation is not displayed, in which the first segment is again separated into two sub-segments which are searched for further change points. No further change points were identified. © 2022 IEEE.

to compute the threshold F_α, given a significance level α, which has to be exceeded in order that H_0 is rejected, i.e. that this potential date is selected as change point:

$$F = \frac{\hat{\sigma}_1^2}{\hat{\sigma}_2^2} \underset{H_0}{\overset{H_1}{\gtrless}} F_\alpha. \tag{5.2}$$

If the F-Value series exceeds the threshold at more than one potential change point, the date which yields the highest F-Value is selected as change point.

The test is a recursive test in order to enable the detection of multiple change points in a time series. If a change point is detected, the time series is split at this point into two smaller segments, which are then again searched for further change points. This process is repeated until no further change points are detected. A pixel is selected as TPSC if at least one change point has been detected in its time series.

The procedure of the TPSC detection and change point estimation is displayed in Figure 5.2 using the example of a real SAR pixel. The amplitude time series (Figure 5.2 (a)) can be visually segmented into three parts, in which the second part is approximately located between the 90th and 154th acquisition and characterized by an increased amplitude. The maximum F-value for the whole time series (Figure 5.2 (b)) is located at the 154th acquisition and above the threshold. As a result, this pixel is classified as TPSC and the 154th acquisition is identified as the first change point. The time series is split into two shorter segments at this change point and further change points are searched in the two shorter segments with adapted thresholds (Figure 5.2 (c), (d)). One more change point is identified in the first segment at acquisition 92. The last iteration of the change point estimation is not shown in Figure 5.2, in which the first segment was again split into two smaller segments and these sub-segments were searched for further change points. No further change points were identified in this example.

5.3. Incorporation of TPSs into the PSI Algorithm

The incorporation of the identified TPSs into our PSI algorithm is described in the following. The flowchart of the proposed method is shown in Figure 5.3. The main parts are the parameter estimation of TPSs, the phase-based change date refinement, the joint unwrapping of PSs and TPSs and the phase inversion and temporal datum reformulation for certain TPSs.

5.3.1. Parameter Estimation

The parameter estimation of a TPS based on periodograms (Equation 3.9) must be limited to the interferograms inside the TPS lifetime. In order to efficiently estimate the parameters of PSs and TPSs jointly, we introduce a weight w into the periodogram [(Equation 3.9)], as done in (Perissin and Wang, 2012):

$$\gamma(k_r^*) = \frac{1}{N} \left| \sum_{n=1}^{N} w_n \exp\left(j\tilde{\phi}\right) \exp\left(j\omega_n^{(k)} k_r^*\right) \right|^2 . \tag{5.3}$$

The weight is zero for interferograms outside and one for interferograms inside the lifetime of TPSs.

5.3.2. Change Point Refinement

The change point estimation solely based on amplitude statistics can be inaccurate. We found that the amplitude-based F-Test sometimes detects the construction start of new buildings as appearing date, while the coherent lifetime of TPSs on those buildings begins with the completion of the buildings. An example of a falsely estimated change point of an appearing TPS is displayed in Figure 5.4. The TPS is
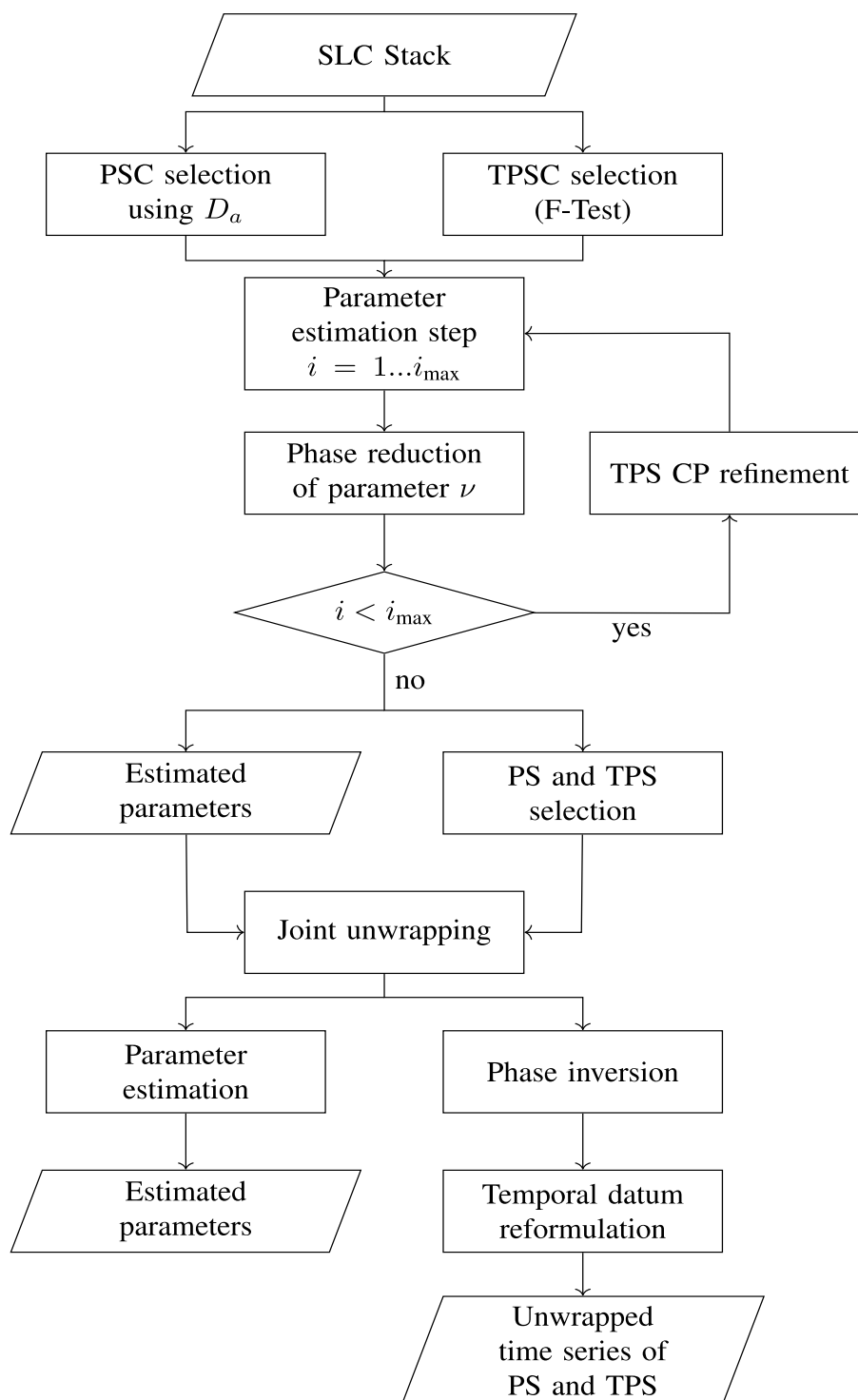
Figure 5.3.: Flowchart of the proposed method to fully integrate TPSs into the PSI approach. © 2022 IEEE.
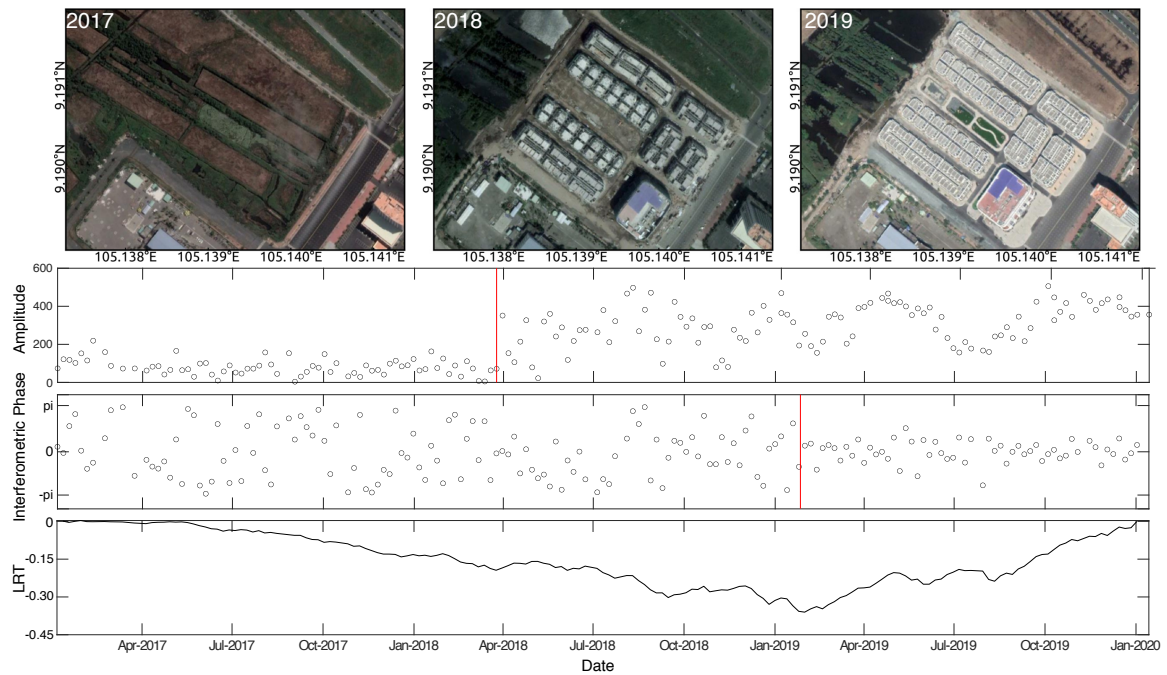
Figure 5.4.: Visualization of the need to refine the initial change point estimation at the example of a TPS in a development area in Ca Mau City, Vietnam. (Top Row) Optical imagery of the development area. The left image was acquired before the construction start in 2018, the center image in 2018 during constructions and the right image in 2019 after completion of the constructions. (Upper Center Row) Amplitude time series of a TPS pixel in the development area. The red line indicates the location of the change point estimated by the F-Test. (Lower Center Row) Interferometric phases of the TPS between temporally sequential SAR acquisitions. The red line indicates the location of a change point detected using the phase-based likelihood ratio test (LRT). (Bottom) Test statistic of the phase-based LRT for change point detection. Imagery data: Google Earth, © 2021 Maxar Technologies. © 2022 IEEE.

located in a development area which was in construction during 2018 and finished in late 2018. The change point estimated by the amplitude-based F-Test is located at the beginning of the construction phase in 2018 when the amplitude of the pixel increased considerably (Figure 5.4 (b)). However, the coherent phase of the TPS only starts at the completion of the constructions in late 2018. This can be seen in the plot of the phases of time-sequential interferograms which are characterized by a considerable gain in coherence after completion of the constructions. In this case, the assumption that abrupt changes in the coherence of a pixel are accompanied by abrupt changes in its amplitude still holds true, but there is a temporal offset between both events. This temporal inconsistency demonstrates the need to refine the initial change point estimates on the basis of the phase coherence of TPSs.

The reason why we initially estimate the change points based on amplitude statistics is that the interferometric phases can, prior to the parameter estimation, be disturbed as shown in Equation 2.16 so that the coherent and non-coherent segments of a TPS

cannot be separated in interferometric phases. We here present a method to iteratively update the change point estimates during the iterative parameter estimation in the M-SBAS approach. After each parameter estimation step, the change point estimates are refined with the goal to avoid noisy phase observations in the following parameter estimation steps and subsequent unwrapping.

The marginal PDF of the interferometric phase [... is given in Equation 2.30].We use this PDF to construct a likelihood ratio test (LRT) to test if two sets of interferometric phases are characterized by significantly different coherent values, given that the expected phases are known.

A set of phases $\boldsymbol{\phi_0} = (\phi_1, \phi_2, ..., \phi_M)$ can be separated into two segments $\boldsymbol{\phi_1} = (\phi_1, ..., \phi_l)$ and $\boldsymbol{\phi_2} = (\phi_{l+1}, ..., \phi_M)$ at point l. The absolute coherence values $|\hat{\gamma}_0|$, $|\hat{\gamma}_1|$ and $|\hat{\gamma}_2|$ for the whole set and the two segments, respectively, can be estimated using the temporal coherence estimator (Ferretti et al., 2001)

$$|\hat{\gamma}| = \frac{1}{N_i} \left| \sum_{n=1}^{N_i} \exp\left(j\phi_n\right) \right|, \tag{5.4}$$

where N_i denotes the number of phase measurements in the particular set or segment. The LRT tests the null hypothesis H_0 that the two segments are characterized by the same coherence against the alternative hypothesis H_1 that they have significant different coherence values. The logarithmic LRT can be expressed as

$$
\begin{aligned}
L(n) &= \log\left(p\left(\boldsymbol{\phi_0}|\hat{\gamma}_0, \boldsymbol{\phi_0^0}\right)\right) \\
&\quad - \left[\log\left(p\left(\boldsymbol{\phi_1}|\hat{\gamma}_1, \boldsymbol{\phi_1^0}\right)\right) + \log\left(p\left(\boldsymbol{\phi_2}|\hat{\gamma}_2, \boldsymbol{\phi_2^0}\right)\right)\right] \\
&= \log(p_0) - (\log(p_1) + \log(p_2)) \underset{H_1}{\overset{H_0}{\gtrless}} T,
\end{aligned}
\tag{5.5}
$$

where $p(\boldsymbol{\phi_i}|\hat{\gamma}_i, \boldsymbol{\phi_i^0}) = p_i$ is the likelihood that the observations in $\boldsymbol{\phi_i}$ can be described by coherence $\hat{\gamma}_i$ with a given expected phase vector $\boldsymbol{\phi_i^0}$ and T is some threshold. We construct a phase-based change point detection algorithm based on the LRT similar to the amplitude-based F-test change point detection. We take every acquisition of a SAR time series as a potential change point and separate the phase time series at that change point into two segments. We then form interferograms within the two segments and apply the LRT. If the LRT series is below the threshold at more than one potential change point, the date which yields the lowest LRT value is selected as change point. The test is implemented iteratively like the amplitude-based F-Test to detect multiple change points, i.e. if one change point is identified, the phase time series is split at this point into two smaller segments which are then again searched for further change points.

The choice of interferograms to use for the LRT is crucial in the test. Interferometric phases are usually disturbed, as shown in Equation 2.16. We have to suppress the phase contributions due to the considered parameters as much as possible to be able to properly estimate the coherence of TPSC segments. Furthermore, we want to be

able to get an estimate of the expected value of the phases $\boldsymbol{\phi^0}$ which is necessary to evaluate the PDF in Equation 2.30. For these purposes, we integrate the LRT into the parameter estimation in M-SBAS to iteratively refine the change points of TPSCs after each parameter estimation iteration. In the following, we assume that the initial change point estimation is sufficiently accurate, which means that there are significantly more coherent than noisy interferograms exploited in the first iteration of the parameter estimation. After a parameter estimation step, we reduce the phase contribution due to that parameter from the phase observations. We then build small-baseline interferograms within the segments with regard to the parameters not yet estimated. For example, if the height of a TPSC was estimated in the first parameter estimation step, we reduce the phase due to the estimated height and subsequently build interferograms with small temporal and thermal baselines in the segments to apply the LRT. This way, the phase contributions due to the parameters height, linear displacement rate and thermally induced displacement rate are reduced as much as possible for the coherence estimation. Additionally, the expected phase of these interferograms is assumed to be *zero*.

In theory, it would be desirable to use a redundant small-baseline network for the coherence estimation (Schenk, 2015), but this is too costly in the change point detection algorithm. We instead use a minimum spanning tree (MST) to find appropriate small-baseline interferograms. For this purpose, we have to define a weight (distance metric) for each multi-master interferogram depending on the baselines, which have to be small in the particular case. We can use the Euclidean distance between the acquisitions in the baseline space as weight, but we first have to define a ratio between the axis units of the particular baselines. We follow the approach of Pepe and Lanari (2006) and just divide the baselines by their range, for example $B'_\perp = B_\perp / (\max(B_\perp) - \min(B_\perp))$. Obviously, the weights could also be defined in a different way, depending on the SAR sensor and the conditions in the study area. The MST selects the path of interferograms with the minimum total weight. As soon as two parameters have been estimated in the iterative parameter estimation process, the MST equals the set of sequential interferograms with regard to the given remaining baseline.

The threshold T of the LRT can be determined using simulations of interferometric phases or by applying the test to phases of PS points in real SAR stacks and setting the threshold with regard to a maximum number of false positive change detections. In order to make the threshold independent of the time series length, we normalize the LRT by the number of phase observations N_i in the segments:

$$L(n) = \frac{\log(p_0)}{N_0} - \frac{\log(p_1) + \log(p_2)}{N_1 + N_2} \underset{H_1}{\overset{H_0}{\gtrless}} T, \qquad (5.6)$$

where $N_0 = N_1 + N_2$ for non-redundant interferogram networks like in the MST approach described above.

The presented test provides change points dividing segments of significantly different coherence values. However, we still have to decide whether a segment is accepted as a coherent segment. The test could, for example, identify a change point between two

segments which both do meet the requirements of a coherent segment. In this case, we want to decide that both segments are coherent and combine both again. For this purpose, we estimate the coherence of the TPSCs in each of their segments and apply a coherence threshold to decide if the segment is coherent or not.

The coherence threshold depends on the time span of the segments. Decorrelation effects lead to a loss of coherence over time both in segments which are considered as incoherent or coherent, which is why the coherence value should be defined to decrease with increasing segment length. We use an empirical, data-driven approach to estimate the relationship between segment length and coherence threshold. We assume that we observe both coherent and incoherent segments with the same segment length. The empirical PDF of the coherence of segments with a given length is thus the weighted sum of the PDF of coherent segments $p_c(|\hat{\gamma}|)$ and the PDF of incoherent segments $p_{ic}(|\hat{\gamma}|)$ of that length:

$$p(|\hat{\gamma}|) = w p_c(|\hat{\gamma}|) + (1 - w) p_{ic}(|\hat{\gamma}|), \tag{5.7}$$

where $0 \leq w \leq 1$. If we are able to describe both PDFs separately in a mathematical way, we can derive the probability P_c that a segment with that length and a given estimated coherence value belongs to the coherent population:

$$P_c(|\hat{\gamma}|) = \frac{w p_c(|\hat{\gamma}|)}{p(|\hat{\gamma}|)}. \tag{5.8}$$

This approach is similar to the coherence threshold determination in Hooper et al. (2007). The adaptive coherence threshold estimation allows to set the LRT threshold the way that the false positive change detection rate is significantly higher than the false negative change detection rate as adjacent segment of the same type are again merged later.

In practice, we bin the TPSC segments in bins with a certain time span in order to get a critical mass of segments to derive the relationship between segment length and coherence threshold. Normalized histograms of the estimated coherence values for TPSC segments with a time span between 200 and 320 days and between 680 and 800 days for TPSCs in a Sentinel-1 data stack are displayed in Figure 5.5. It can be seen that the probability densities in both cases can be described by the sum of two scaled probability densities, as expected, and that the coherence values are generally higher for the shorter segments. We fit a Beta mixture model to the observed coherence values to describe the probability densities of incoherent and coherent segments and their weights. The Beta distribution is a flexible two-parameter distribution defined on the interval (0,1) which we consider suitable to describe the probability density of the observed coherence values. It has been used before to describe InSAR coherence statistics (Zhang et al., 2016). For each segment bin, we fit the mixture model to the observed coherence values and use Equation 5.8 to find the particular coherence threshold under a defined probability P_c. The estimated thresholds for bins of different segment time spans for the study case based, demanding a probability $P_c = 0.5$, are also displayed in Figure 5.5. They are decreasing with
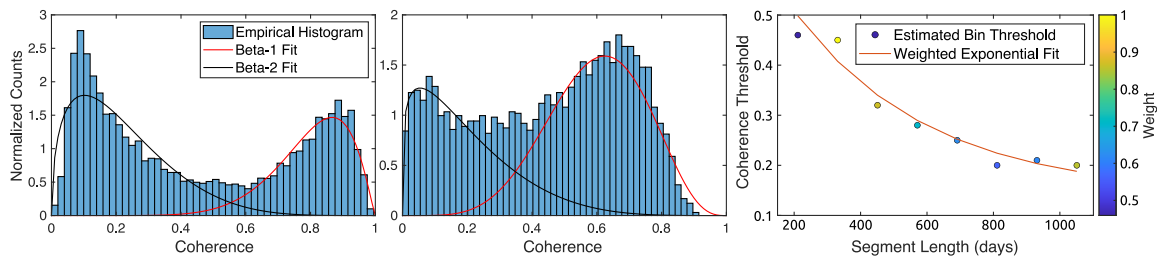
Figure 5.5.: Normalized histograms of estimated coherence values for TPSC segments with a time span between 200 and 320 days (left) and between 680 and 800 days (center) for TPSCs in a Sentinel-1 data stack. The two single densities of the fitted Beta mixture models are plotted in red (coherent segments) and black (incoherent segments). The estimated coherence thresholds for bins with different time spans are shown on the right with a weighted exponential fit.

increasing segment length and approximately approach a coherence value of 0.2 at long segment lengths in the given example. We fit an exponential function to the estimated coherence thresholds to get a description of the relationship between the segment length and the coherence threshold using weighted nonlinear regression. The weights of the bins are the integrated differences between the empirical and the fitted cumulative distribution functions.

In case that the initially and refined change points differ for a TPSC, we estimate its coherence for the differently estimated coherent intervals and choose the set of change points leading to the larger coherence value. For the example in Figure 5.4, the test statistic of the LRT is minimized in early 2019 after the end of the constructions. The TPS segment was identified to be coherent from this date on. The appearing date of the particular TPS was shifted by more than nine months, leading to an avoidance of 50 noisy SAR scenes in the following steps of the PSI analysis.

5.3.3. TPS Selection

After the parameter estimation, we select TPSs accordingly to the PS selection procedure based on the phase coherence thresholds we determined before. However, the coherence is now estimated using all available multi-master interferograms inside the lifetime of the TPSCs.

5.3.4. Unwrapping

As mentioned in Section 3.2, we make use of the unwrapping algorithm implemented in the StaMPS software (Hooper, 2010) in the M-SBAS approach. The incorporation of TPSs into the PS unwrapping with the purpose to jointly unwrap PSs and TPSs is described in the following. After the selection of PSs and TPSs, we export their interferometric phases and metadata into the StaMPS specific *Matlab* format. We include a mask which flags the interferograms outside the TPS lifetime.
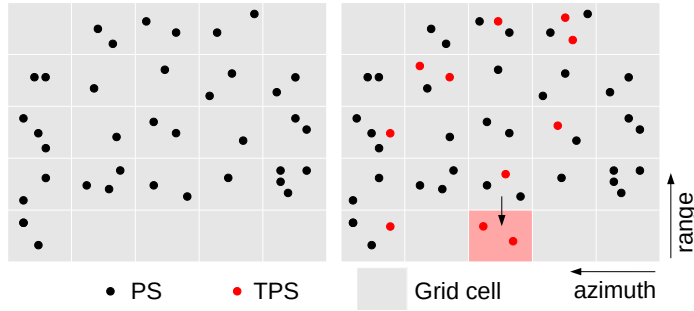
Figure 5.6.: Visualization of the phase gridding before the unwrapping. (Left) Only PS points were considered in the original PSI approach. (Right) PSs and TPSs are now considered for the unwrapping, leading to a densification of the observation point network. If there are grid cells which are only occupied by TPSs that are all not active in certain interferograms (red grid cell), the particular grid cells are interpolated in these interferograms by filled grid cells using nearest neighbor interpolation. © 2022 IEEE.

The incorporation of TPSs into the unwrapping requires the unwrapping of multi-master interferograms like small-baseline interferograms and a subsequent phase inversion. The reason behind is that the use of single-master interferograms would rigorously exclude TPSs whose lifetime does not cover the selected master scene. The use of multi-master interferograms allows every TPS, including those which are not active at the selected master scene.

The unwrapping algorithm in StaMPS works with spatially gridded phases (Hooper, 2010) which are formed by summing up the phases of PSs located within the grid cells. We modify this by also adding the phases of TPSs which are located in the grid cell and active in the given interferogram. This is easily done by multiplying the TPS mask, which flags the interferograms outside the TPS lifetime with a *zero*, with the TPS phases and also passing them to the gridding algorithm.

Grid cells which are exclusively occupied by TPSs might be empty in certain interferograms when these interferograms are outside the lifetime of all contained TPSs. We refer to these grid cells as partly empty cells. They are interpolated in the given interferograms by filled grid cells using nearest-neighbor interpolation (Figure 5.6). All other interferogram phases of the concerned grid cells are conventionally formed by summing up the coherent TPS phases. The nearest-neighbor interpolation is carried out, since we expect the residual signal to be smooth in space after reduction of the [phase due to the] parameters estimated in M-SBAS. With the help of this approach, the StaMPS unwrapping algorithm can be utilized to jointly unwrap PSs and TPSs. The unwrapped values of the interpolated grid cells in the given interferograms will not be used later, the interpolation is only done in order to enable the joint unwrapping of PSs and TPSs based on the available unwrapping algorithm.

We conducted the following experiment in order to test if the proposed method is able to handle partly empty cells influences the unwrapping of neighboring filled grid

cells. We applied the PSI method presented in Section 3.2 to a Sentinel-1 stack of 225 scenes covering the Vietnamese city of Ca Mau (see Section 5.4) and unwrapped small-baseline interferograms phases using the StaMPS unwrapping. We then emulated the presence of partly empty cells for further unwrapping runs and compared the results. The partly empty cells were randomly chosen, and their share was $5\,\%$ of the total number of grid cells. We divided the partly empty cells into two groups which were characterized by randomly selected appearing and fading dates, respectively. The selection of cells and appearing/fading dates and subsequent unwrapping was carried out 50 times. The average relative number of unwrapped phase values diverging from those from the reference unwrapping run was $0.03\,\%$, neglecting the interferograms outside the lifetime of the partly empty cells. We conclude that the proposed method to handle partly empty cells has no negative influence on the unwrapping results of filled neighboring cells. In practice, we expect the incorporation of TPSs to rather enhance the unwrapping due to a densification of the observation point network (Figure 5.6).

5.3.5. Single-Master Phase Inversion and Temporal Datum

The unwrapped multi-master interferometric phases $\boldsymbol{\varphi_{mm}}$ have to be inverted in order to get integrated phase time series $\boldsymbol{\varphi_{sm}}$ for each PS and TPS with respect to the selected spatial and temporal reference. The functional model describing the relationship between $\boldsymbol{\varphi_{mm}}$ and $\boldsymbol{\varphi_{sm}}$ is given by

$$\boldsymbol{\varphi_{mm}} = A\boldsymbol{\varphi_{sm}}, \tag{5.9}$$

where A denotes the matrix describing the multi-master interferogram network. The inversion is solved in StaMPSs in a least-squares sense (Hooper, 2008), which is, however, only feasible if there are no separated interferogram subsets in the network. We are facing two problems with the TPS phase inversion. First, recurring TPSs are characterized by separated lifetime segments, i.e. separated subsets in the interferogram network. Second, the flexible handling of TPSs with different lifetimes prevents the selection of a master scene which is included in the lifetime of all TPSs and thus the referencing of all PSs and TPSs to a common temporal datum. The approaches to both problems, which are interconnected, are described in the following. The second one is treated first for the sake of an easier understanding.

Consider TPSs with a single lifetime which does not include the selected master scene. We invert the phase of these TPS using their first acquisition of presence as temporary defining temporal datum. Subsequently, their temporal datum is re-defined on basis of the displacement time series of neighboring PSs which behave similarly. In case of spatially correlated displacement fields, one could interpolate the displacement time series of surrounding PSs onto the TPS positions, e.g. by using Kriging (Wackernagel, 2013) or Least-Squares-Collocation (Moritz, 1978), and use the predicted displacement time series for datum definition. As the assumption of spatially correlated displacements does not necessarily hold true [...], we chose another approach for datum definition of these TPSs. We compare their time series of TPSs
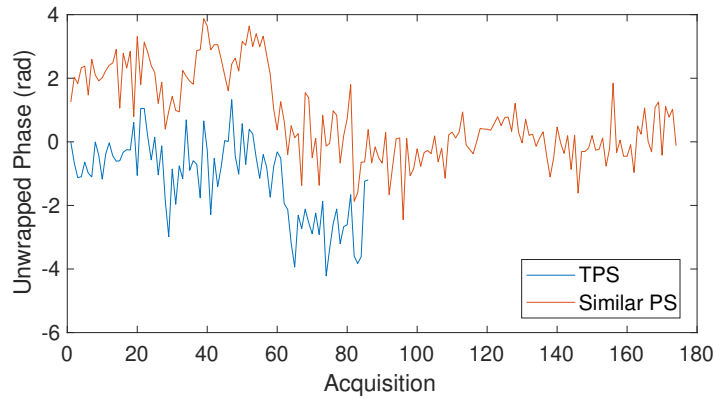
Figure 5.7.: Phase time series of a fading TPS whose datum is the first acquisition and a nearby PS which is referenced to the master acquisition 117. The PS was found to behave similarly as the TPS by means of the Ljung-Box test. © 2022 IEEE.

with those of neighboring PSs with the purpose to find PSs which show a similar behavior in the displacement time series, i.e. PSs whose displacement is likely to be generated by the same process as the displacement of the given TPS. This is carried out by calculating the difference between the displacement time series of the TPSs and all of their neighboring PSs and applying the Ljung-Box-Test (Ljung and Box, 1978). The Ljung-Box test statistically tests if the time series of differences are stationary with no autocorrelation exhibited by checking the overall significance of autocorrelation based on a number of lags. It was originally developed to test a lack of fit in autoregressive-moving average models. The test statistic Q is defined as

$$Q = M(M+2) \sum_{k=1}^{L} \frac{\rho(k)^2}{M-k}, \tag{5.10}$$

with M denoting the sample size, L the number of autocorrelation lags and $\rho(k)$ the sample autocorrelation at lag k. Under the null hypothesis H_0 that the residuals exhibit no autocorrelation for the fixed number of lags, the asymptotic distribution of Q is the χ^2-distribution with L degrees of freedom. H_0 is discarded if $Q > \chi^2_{L,1-\alpha}$ given a significance level α.

The PSs which meet the null hypothesis are selected as PSs whose displacement are probably generated by the same underlying process as that of the considered TPS. The displacement time series of a TPS and a PS which were found to behave similarly using the Ljung-Box-Test are displayed exemplarily in Figure 5.7. The datum of the TPS is re-defined by minimizing the difference of the time series of the TPS to the averaged time series of all selected PSs. In case there are no neighboring PSs showing similar displacement as the TPS, there is no information on the link of the TPS displacement time series to the temporal datum. The TPS displacement time series is then shifted by the mean difference of its displacement time series to that of neighboring pixels whose lifetimes include the selected master scene.

The issue of TPSs having separated lifetime segments is approached as follows. One way of solving the problem of separated subsets in the inversion is to use a regularization method like the SVD as in the classical SBAS method (Berardino et al., 2002) or imposing temporal constraints (Doin et al., 2011; Morishita et al., 2020). In our initial approach presented in Dörr et al. (2022a), we inverted the phases of recurring TPS by adding the constraint of linear displacements to the inversion, like in the NSBAS (Doin et al., 2011) and LiCSBAS methods (Morishita et al., 2020). In this case, temporal gaps in the interferogram network of recurring TPSs are connected assuming a linear displacement rate. While this constraint might be reasonable for short temporal gaps, it heavily impacts the inversion of recurring TPSs with long temporal gaps between their separated lifetimes in a negative way if the assumption of linear displacement rate does not reflect reality. Instead, we separately invert the segments of recurring TPSs and separately re-define their temporal datum as described before.

5.4. Experiment with Sentinel-1 Data

5.4.1. Data and Study Area

We applied the proposed method to a stack of 225 VV-polarized Sentinel-1 SAR scenes, acquired in descending orbit between November 2016 and November 2020 in the Interferometric Wide Swath Mode over the City of Ca Mau in the Vietnamese Mekong Delta (Figure 5.8a). The study area is about $9.5 \times 9\,\text{km}^2$. The interferometric pre-processing included SAR image coregistration to the selected geometrical master scene by means of Enhanced Spectral Diversity as well as the subtraction of simulated reference and topographic phase based on the TanDEM-X global DEM with a grid size of 90 m. The Vietnamese Mekong Delta, which is only 0.8 m above sea-level on average (Minderhoud et al., 2019), has recently been affected by subsidence of rates up to several centimeters per year (Erban et al., 2014; Minderhoud et al., 2020). At the same time, the region has been characterized by high construction activity and land use change (Minderhoud et al., 2018) for the last decades, which makes it a suitable area to evaluate the proposed method.

5.4.2. Results

We carried out three different processing runs to test the proposed method: (i) the original M-SBAS approach, (ii) M-SBAS incorporating TPSs without change point refinement, i.e. only using the amplitude-based change date detection from (Hu et al., 2019), and (iii) the full approach incorporating TPSs with change point refinement. The thresholds used in the processing were chosen as follows: the amplitude dispersion threshold for the PSC selection was set to 0.47, the significance level α in the amplitude-based F-Test was 0.001 and the threshold T in the LRT was set to $-0.03 - 3.5/N_0$ where N_0 is the length of the segment to be checked for change points. The asymptotic threshold of -0.03 was determined using simulation studies. The reciprocal term was introduced with the goal to suppress noise in the change date detection by requesting

Table 5.1.: Results of three processing runs with Sentinel-1 data over the city of Ca Mau: (i) original M-SBAS approach, (ii) M-SBAS incorporating TPSs without and (iii) M-SBAS incorporating TPSs with change point refinement. The average coherence was computed using all accepted PSs and TPSs. © 2022 IEEE.

Processing run	(i)	(ii)	(iii)
# accepted PSs	46 553	27 370	27 334
# accepted TPSs	-	87 478	93 698
# appearing TPSs	-	26 418	27 381
# fading TPSs	-	18 265	18 989
# visiting TPSs	-	10 513	15 837
# recurring TPSs	-	32 282	31 067
Avg. coherence	0.54	0.57	0.6
Avg. coherence TPSs	-	0.57	0.61

higher confidence for change dates to be accepted in shorter segments. The coherence threshold for the (T)PS selection was empirically determined as described in Section 5.3.2. The (T)PS identification and parameter estimation for the three runs took 25 min, 97 min and 181 min, respectively, on a machine with a 12-core CPU (Dual Intel Xeon X5680 3.3 GHz).

The number of accepted measurements points and their average coherence in the three runs are displayed in Table 5.1. The observation points encompass both PSs and TPSs. The three approaches yielded 46 553, 114 848 and 121 032 accepted observation points, respectively. The estimated linear displacement rate in LOS of the identified observation points in approaches (i) and (iii) are displayed in Figure 5.8. The density of observation points is increased throughout the whole study area, while the TPSs are, like the PSs, virtually exclusively located at man-made structures. The spatial distribution of linear displacement rates is consistent in both results. The block of buildings, which was built within the exploited time series (Figure 5.4), is a striking example where no PSs are identified at all, but many TPSs (Figure 5.8 d-f). The TPSs on the buildings are [...] stable whereas TPSs on the surface ground exhibit high displacement rates. This is similar to the building south of the new block, which is stable compared to its surrounding surface ground. Another example of an area which changed considerably during the time series is displayed in Figure 5.8 g-i, where buildings were torn down to be replaced by a street. The density of observation points is increased throughout the whole area, but the increase in identified points can be seen especially in the mentioned section where the street was built. No PSs but many fading TPSs were identified here.

In the original approach, 46553 PSs were identified, while in both other approaches only little more than 27300 PSs were identified. This discrepancy is due to the fact that a portion of the pixels which were identified as PSs in the original approach were identified and treated as TPSs in the other two approaches. We refer to these pixels as Ambivalent Persistent Scatterers (AmPSs). The average a-posteriori coherence of these was 0.5 in approach (i), thus lower than the average coherence of 0.54 of all PSs
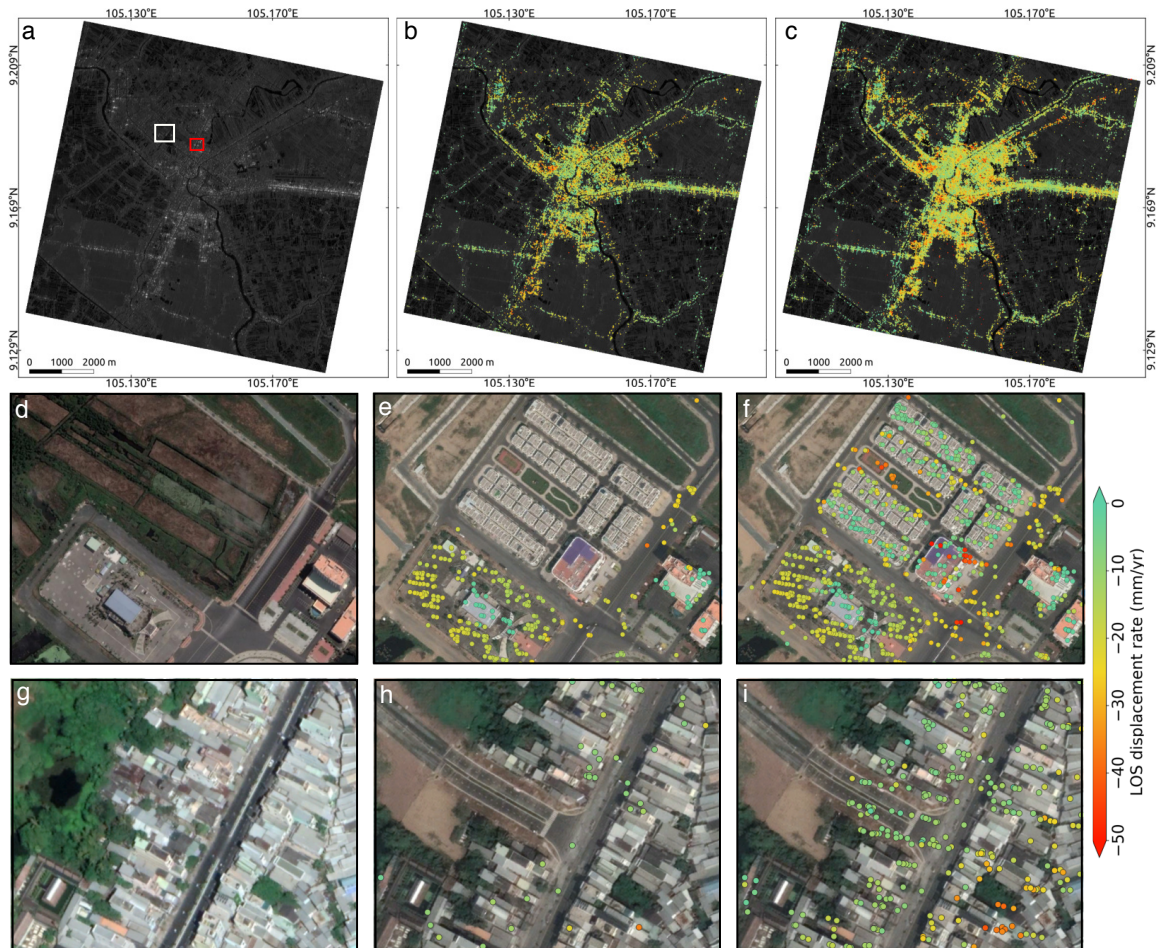
Figure 5.8.: (a) Mean amplitude of the Sentinel-1 SAR stack in the study area. (b), (c) Linear displacement rate in LOS for accepted observation points in the standard M-SBAS and the M-SBAS incorporating TPSs processing runs, respectively. (d) Optical image of the areas in the white rectangles in (a) from 2017, the beginning of the considered time series. (e), (f) Linear displacement rate in LOS of accepted observation points for both processing runs, respectively, in the white rectangles, overlaid on optical imagery from the end of the time series. (g), (h),(i) same as (d), (e), (f) for the red rectangle in (a). Imagery data: Google Earth, © 2021 Maxar Technologies. © 2022 IEEE.
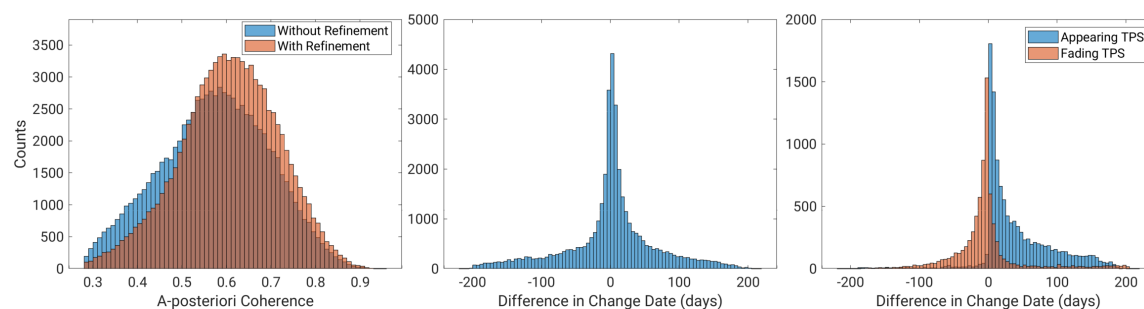
Figure 5.9.: (Left) Estimate of the a-posteriori coherence of TPSs in the test study without and with change point refinement. (Center) Shift in the change date of TPSs whose change dates have been refined. (Right) Shift in the change date of appearing and fading TPSs whose change dates have been refined. © 2022 IEEE.

in the approach. When applying approach (iii), the average number of acquisitions in their lifetime decreased from 225 to 170. However, their mean coherence increased to 0.6. The average coherence of all observation points was 0.54, 0.57 and 0.6 in the three approaches.

The number of accepted TPSs for the approaches (ii) and (iii) are 87 478 and 93 698, meaning that more than three times more TPSs than PSs were identified for the Sentinel-1 time series of four years length. In approach (iii), 7.1 % more TPSs were accepted as a result of the change point refinement. The change point refinement can lead to a change of the number of change dates for a TPS, thus potentially to a change of the TPS type. The change dates of 43.7 % of the TPSs were refined in approach (iii). The number of change dates changed for 53 % of the refined points. It can be seen that the number of identified recurring TPSs decreased a little bit.

A histogram of the a-posteriori coherence values of all TPSs in approaches (ii) and (iii) is shown in Figure 5.9. The average coherence of TPSs increased by 7 % and the standard deviation of the coherence decreased as result of the change date refinement. The difference between refined and initial change dates of refined TPSs is also displayed in Figure 5.9. It is between -200 and 200 days with a mean of about *zero*. If only considering appearing and fading TPS types, it can be seen that the change dates of appearing TPSs were postponed in most cases, whereas change dates of fading TPSs were brought forward in most cases.

The initial and refined change dates of appearing TPSs in the block of new houses (Figure 5.4) are displayed in Figure 5.10. The initial change dates of many TPSs were in early or mid of 2018, when the construction was started (see also example in Figure 5.4). The refined appearing dates are much more consistent and mostly shifted to early 2019, when the constructions were finished. The unwrapped displacement time series of a PS next to the block and two TPSs within the block are also shown in Figure 5.10 for the approaches (ii) and (iii). The red TPS is located on a building and the green TPS is located on the surface ground besides the building. We concluded their location from their position and estimated height. The PS was linearly moving
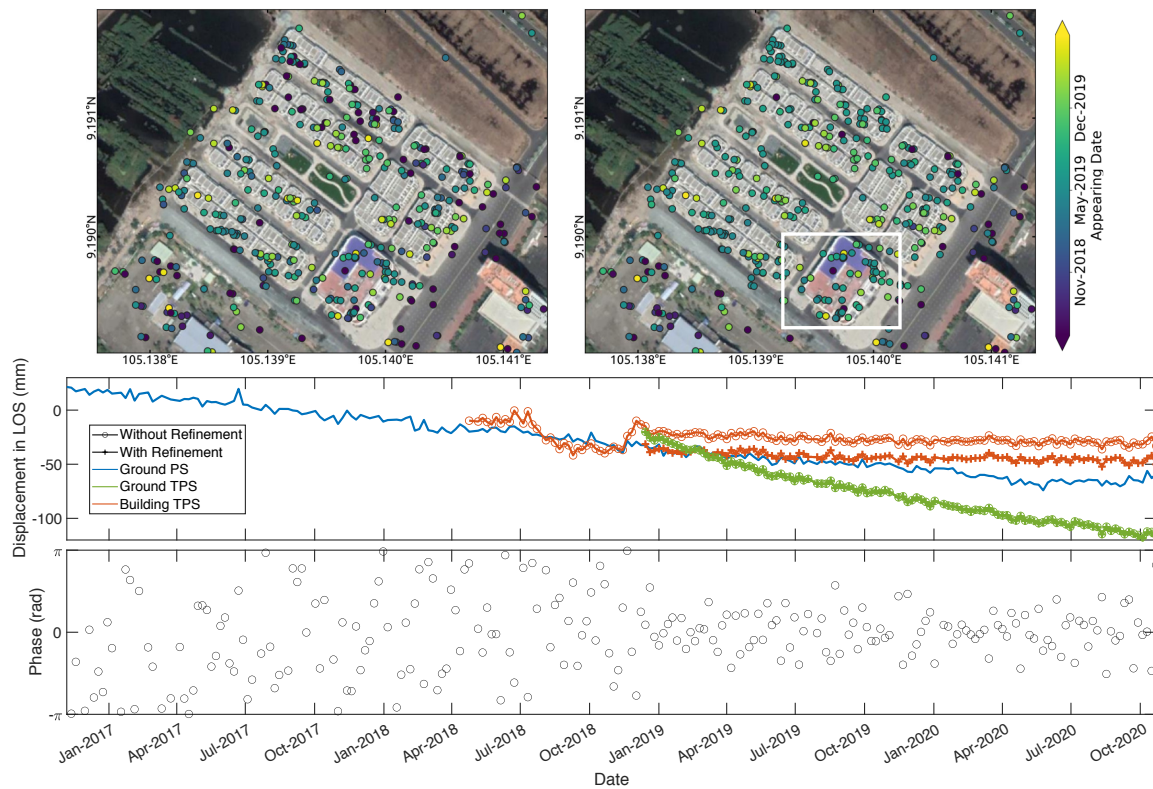
Figure 5.10.: (Upper) Appearing dates of TPSs without (left) and with refinement (right) in a block of buildings which was built during the exploited Sentinel-1 time series (see Figure 3) and finished in early 2019. (Center) Displacement time series of a TPS on the building in the study area and a TPS on the surface ground besides the building in the white rectangle in upper right with and without change point refinement, as well as a PS on the street next to the building. The master scene was on 22 July 2017. (Lower) Sequential, wrapped phase time series of building TPS shown in the center subfigure. Imagery data: Google Earth, © 2021 Maxar Technologies. © 2022 IEEE.

away from the sensor over time. The building TPS was initially estimated to appear in April 2018. The unwrapping of the red TPS without refinement lead to an undulating movement away from the sensor and back before the TPS stays almost stable. The refined appearing date of this TPS is exactly when the stable phase of the TPS begins. We also plotted the wrapped time series of sequential phases of this TPS which considerably gains coherence at the refined appearing date of the TPS. The time series of the TPS in the two approaches are shifted due to the different appearing date, which are used to re-define the temporal datum of the TPS, since it is not active at the selected master scene on 22 July 2017. The appearing date of the green TPS in Figure 5.10 was not changed during the refinement, which leads to the fact that its estimated displacement time series is identical in approaches (ii) and (iii). The TPS was moving away from the sensor with a slightly decreasing rate over time.

5.4.3. Discussion

The proposed method builds on the approach to detect TPSs in Hu et al. (2019) by incorporating it into our multi-stack PSI method with an iterative phase-based change date refinement of TPSs and subsequent unwrapping to receive their displacement time series. The absolute number of identified observation points was increased significantly from 46553 applying the original PSI approach to 114848 and 121032 by incorporating TPSs into the PSI approach without and with change date refinement, respectively, in the Sentinel-1 time series of four years in the Vietnamese city of Ca Mau. Some pixels which were identified as PSs in the original approach were identified and treated as TPSs in the proposed method, which lead to a significant increase of 0.11 in their average coherence. We conclude that they were falsely identified as PSs in the original approach, probably as their incoherent segment was quite short compared to their coherent lifetime. The parameter estimation still obtained reasonable results, and their coherence estimate exceeded the requested threshold. This shows that PSs transform into TPSs over time, which is why the number of identified TPSs increases with increasing time series length to compensate for the loss of PSs, as will be also shown in Section 5.5. In other words, the consideration of TPSs and their incorporation into PSI allows to critically reject time intervals where a stable backscatter point is losing coherence. Thus, the incorporation of TPSs is essential for long-term PSI monitoring in order to keep the network of observation points as dense as possible. This helps to better detect and understand displacement phenomenons on the Earth's surface, especially in heterogeneous displacement scenarios like in urban areas, and can potentially lead to more robust unwrapping results. We showed two examples of areas in Ca Mau whose surface characteristics changed considerably in different ways during the time series, as seen in optical imagery from different years in Figure 5.8. A new block of houses was built in the first example, and buildings were torn down to be replaced by a street in the second. Only a few points were identified in the original PSI approach, but many appearing TPSs could be identified by the proposed method in the first and many fading TPSs in the second example. This illustrates that different kinds of TPSs with different appearing or fading dates are jointly examined in the proposed method. Another advantage of incorporating TPSs is that their change dates provides additional information, e.g. for the purpose of change detection in the study area (Yang and Soergel, 2018; Ansari et al., 2014). Appearing TPSs can furthermore be evaluated to study the initial settlement of newly constructed buildings, which is important information when trying to separate different causes of displacements.

The proposed change date refinement procedure lead to a considerable [mean] increase of 7 % in the a-posteriori coherence of TPSs (Figure 5.9) and to an increase of 7 % in identified TPSs in our experiment, compared to the pure use of the amplitude-based change date detection from Hu et al. (2019). The change date refinement improves the quality of the results by avoiding noisy SAR scenes to be falsely included in the estimated lifetime of TPSs. This potentially leads to an improved parameter and coherence estimation of TPSs, as indicated by the increased a-posteriori coherence, and a more robust unwrapping. The early displacement time series of the red TPS in Figure 5.10 is characterized by undulating movements in LOS when not applying

the change date refinement. The time series is more or less stable after the refined appearing date. The wrapped phases of sequential interferograms after reduction of the estimated parameters indicate that the coherence only increases considerably after the refined appearing date. We conclude that the unwrapping algorithm outputs an apparent signal for the noisy input phases which is characterized by long-wave noise but could be falsely interpreted as a real signal. The refined appearing date, which corresponds to the completion of the constructions as seen in the optical imagery, is the exact one after which the signal is almost stable. As a result, the proposed method yields more reliable results compared to the amplitude-based TPS change date detection approach in Hu et al. (2019), which in turn was shown to provide more robust results compared to ANOVA.

It is striking that the appearing date of most refined appearing TPSs was postponed, while the fading date of most refined fading TPSs was brought forward. We showed an example of this in Figure 5.4 where the amplitude-based change date detection yielded an appearing date of a TPS which marked the start of the construction of the block of buildings, whereas the actual appearing of the TPS was the completion of the block, as seen in the interferometric phases. We assume that the change date refinement of fading TPSs could be caused by the reversed case when a building is torn down. In that case, the coherence is probably already lost when the demolition work starts, but the amplitude of the pixels potentially only declines when the building is completely gone.

The change date refinement can lead to a change in the number of identified change dates, thus also to a change in the TPS type. The increased coherence of TPSs by means of the change point refinement indicates that the change dates are more precisely estimated than before. The decreased number of identified recurring TPSs hints that the proposed change date refinement is a conservative but reliable approach. It has to be kept in mind, that the refined change dates are only accepted if the resulting coherence is increased compared to the coherence estimated from the initial change dates. In case of doubt, segments which were initially assumed to be coherent are discarded during the change date refinement. However, the average false positive and false negative detection rates of the amplitude- and phase-based change detection approaches cannot be quantified without ground truth. This could be subject in future research, for example when applying the proposed method to areas which are periodically inundated, like water reservoirs where the change dates of possible TPSs could be known based on the fluctuating water level.

Previous TPS approaches which aimed at studying displacements did not include unwrapping (Hu et al., 2019; Zhang et al., 2011), but only estimated displacement rates. The proposed unwrapping algorithm allows us to study the displacement time series of PSs and TPSs, hence deviations of the displacements from the model assumed during the parameter estimation. This is important when studying causes of displacements and the effectiveness of countermeasures. The time series of the green TPS in Figure 5.10 shows, for example, a slight decrease in the displacement time series over time. The re-definition of the temporal datum for TPSs whose lifetime

does not include the datum-defining master scene is important in order to consider their displacement time series in a spatial context and compare them to different observation points. However, it has to be kept in mind that a time series does not describe absolute height time series, but displacement time series with respect to the datum, and the re-definition of the datum is not strictly necessary in this geodetic application. In the example in Figure 5.10, it can be seen that the datum of the TPSs is defined depending on their appearing date and the displacement time series of the neighboring PS points.

In the proposed method, we do not consider recurring TPSs to change their parameters over time. This could potentially be the case if a building is torn down and a new building is built at the same place, leading to a recurring TPS to form which is characterized by a different displacement rate, height or thermally induced displacement rate in its different lifetime segments. In that case, the estimated a-posteriori coherence of the TPS would be underestimated if only estimating the parameters for all segments together, leading to a possible rejection of the TPS. Estimating the parameters in different segments of TPSs and studying its effects on the a-posteriori coherence is a topic for follow-on research.

The proposed method with change date refinement of TPSs takes almost twice as long as the method without change date refinement. The major portion of the additional processing time can be attributed to the identification of the MST interferogram connection described in Section 5.3.2. While we find the absolute processing time of $3\,\mathrm{h}$ acceptable for the size of the study area (about $85\,\mathrm{km}^2$) and the SAR stack of 225 scenes regarding the improved results, the change date refinement could also be sped up in the future by implementing efficient approaches for dynamic MSTs (Cattaneo et al., 2010) or using alternative small-baseline interferogram selections for the change date refinement.

The mutual visualization of linear displacement rates over PS and TPS pixels is non-trivial because the visualized rates are only valid for the differing lifetime of the scatterers. We displayed the displacement rates of PSs and TPSs together in Figure 5.8 to illustrate the increase in identified observation points by means of the TPS incorporation, but in general suitable visualization approaches should be developed to display the displacements of TPSs considering their lifetime, in order to avoid misinterpretations. This could be done in the form of time-lapse movies where the displacement rate of observation points is only visible during their lifetime or by displaying yearly displacement rate maps where only points are shown which were active most of the time in the particular year. Another aspect to consider is that the variance of displacement rate estimates depends on the number of scenes in the lifetimes of TPSs (see Equation 4.27). The rate variances of all (T)PSs should be displayed in case that their displacement rates are jointly displayed.

Table 5.2.: Area, number of $1 \times 1\,\mathrm{km}^2$ patches and average number of identified PSs per km^2 in the one-year time series slices in the four study areas.

Study Area	Center Coordinates	Area (km²)	Nr. of Patches	Nr. of PS/km²
Ca Mau	9.172° N, 105.151° E	88.4	121	471
Can Tho	10.027° N, 105.77° E	108.6	143	817
Rural1	10.186° N, 105.897° E	85.1	117	92
Rural2	8.957° N, 105.093° E	78.4	110	72

5.5. Relevance of TPSs for Long-Term PSI Monitoring

In the preceding section, the TPS integration into M-SBAS-2-StaMPS was presented and tested with a Sentinel-1 stack covering the time period of 2016 to 2020. Significantly more TPSs than PSs were identified with the proposed method: the ratio of identified TPSs to PSs was 3.2 and 3.4 in the approaches without and with change date refinement. This section aims at studying the ratio of identified TPSs to PSs as a function of the length of the considered SAR time series in two urban and two rural areas in the VMD. The lifetime of identified TPSs is also analyzed in order to study their actual contribution to the geodetic observation network during the whole observation period. The identification of lots of TPSs which, however, are all characterized by really short lifetimes would not improve the observation network considerably.

The study bases on SAR a data stack consisting of 318 Sentinel-1 SAR scenes which were acquired between April 2016 and April 2022 in descending orbit over the VMD. The characteristics of the data and the applied pre-processing coincide with the data description in Section 5.4.1. The study areas cover the cities of Ca Mau and Can Tho (Figure 6.1) and two rural areas. The center coordinates and the size of each study area are given in Table 5.2. The study area Rural1 is located north of Can Tho and characterized by rice cultivation, while Rural2 is located south of Ca Mau and characterized by aquafarming. All study areas are rectangular and range from 78.4 to $108.6\,\mathrm{km}^2$ in size.

To study the ratio of identified TPSs to PSs with regard to the time series length, we sliced the available time series into segments with lengths of one to six years, always beginning and ending in April. We used all possible slices (i.e. 04/2016-04/2017, 04/2017-04/2018, 04/2016-04/2018 etc.) to increase the sample number, resulting in six one-year slices, five two-year slices, four three-years slices and so on. [... Our PSI] approach was carried out for each time series slice and study area with and without the incorporation of TPSs. For the analysis of the ratio of identified TPSs to PSs, we subdivided the study areas in small patches of $1 \times 1\,\mathrm{km}^2$ to be able to describe the results in a proper statistical way. The number of these patches in each study area is listed in Table 5.2.

This study is only based on the TPS integration without change date refinement due to the huge computational cost for analyzing each time series slice separately. The change date refinement lead to an increase of 7 % in the number of identified TPSs in the study in Section 5.4, so we assume that the numbers of identified TPSs are consistently slightly underestimated in this study. The change date refinement partly also lead to considerable changes in the lifetime length of TPSs in the study in Section 5.4, however the mean change among different kinds of TPSs was negligible (see Figure 5.9).

5.5.1. Results

We identified PSs, TPSs and AmPSs in each study area and time series slice. AmPSs are pixels which were identified as PSs in the PS-only processing, but as TPSs in the joint processing. We assume that they are in most cases TPSs whose lifetime is only marginally shorter than the available time series so that they could still be identified as PSs in the applied multi-stack PSI approach, i.e. false positive PSs. Alternatively, they could also be false positive TPS detections.

The average number of identified PSs per km^2 for the six one-year time series slices in the different study areas is displayed in Table 5.2. It is largest in Can Tho with 817 PS/km^2 and lowest in Rural2 with 72 PS/km^2. In order to enable a comparison of the number of identified PSs, TPSs and AmPSs for the different time series length, we computed a reference number of TPSs $N_{\mathrm{ps,ref}}$ for each $1 \times 1\,\mathrm{km}^2$ patch in each study area. It is the number of identified PSs in the respective patch, averaged over the six one-year time series slices. We then calculated the ratios of identified PSs, TPSs and AmPSs in each patch for each time series slice and the respective reference number. Box plots of the resulting ratios for the two cities and the two rural areas are displayed in Figure 5.11 and Figure 5.12, respectively. The results are similar for in the four study areas. The number of identified PSs decreases steadily with increasing time series length after two years, and the median PS ratio is below 50 % for a time series of six years in all study areas. On the contrary, the number of identified TPSs steadily increases with increasing observation length. The median TPS ratio is below 90 % for a time series of two years and above 220 % for a time series of six years in each area. The number of AmPSs slightly increases with increasing time series length. The median AmPS ratio is below 45 % in each area for a time series length of six years.

The so far addressed ratios do not provide information on the actual lifetime of the identified TPSs. For this purpose, we introduce a measure called the effective lifetime ratio *ELR*. We refer to the effective lifetime *EL* as the sum of number of acquisitions in the lifetime of all *K* available observation points [(PS-only or sum of PSs and TPSs)] Δt_{on} divided by the total number of available acquisitions in the time series M_{acq}:

$$EL = \frac{\sum_{k=1}^{K} \Delta t_{k,\mathrm{on}}}{M_{\mathrm{acq}}}. \tag{5.11}$$
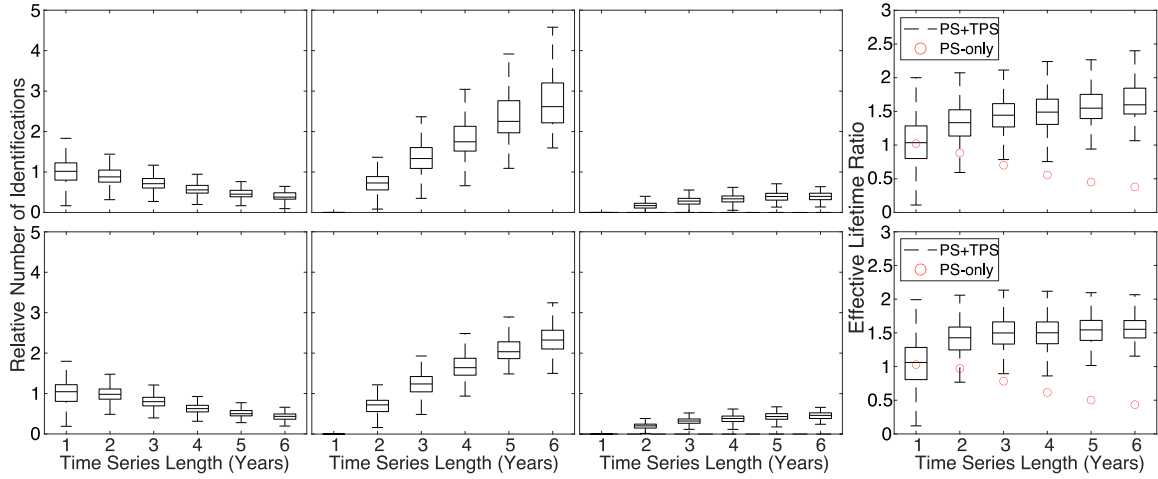
Figure 5.11.: Ratios of identified PSs (left), TPSs (center-left) and AmPSs (center-right) to the reference number of PSs and effective lifetime of PS+TPS and PS-only processing (right) in the cities of Ca Mau (upper) and Can Tho (lower). The outliers of the boxplots are not plotted. © 2022 VDE.

[...]. For a PS-only processing run, the effective lifetime equals the number of identified PSs since the lifetime of PSs always equals the number of acquisitions in the time series. The effective lifetime ratio is the ratio of the *EL* of a given processing result to the *EL* of the reference PSs:

$$ELR = \frac{\sum_{k_1=1}^{K} \Delta t_{k_1,\text{on}}}{M_{\text{acq}}} \bigg/ \frac{\sum_{k_2=1}^{K_{\text{ps,ref}}} \Delta t_{k_2,\text{on}}^{\text{ref}}}{M_{\text{acq}}^{\text{ref}}} = \frac{\sum_{k_1=1}^{K} \Delta t_{k_1,\text{on}}}{M_{\text{acq}} K_{\text{ps,ref}}}. \tag{5.12}$$

The effective lifetime ratio of PS-only processing results equals the ratio of identified PSs to the reference PSs. The *ELR* of PS+TPS runs for the different time series slices are displayed in Figures 5.11 and 5.12. In order to enable a better comparison with the effective lifetime of PS-only runs, the median *ELR* of the PS-only results are also displayed in the Figures. The results show a considerable decrease of the *ELR* with increasing time series length for the PS-only runs, which reflects the decreasing number of PSs with increasing observation time. In contrast, when considering TPSs and PSs, the *ELR* first increases to more than 1.5 with increasing time series length in all study areas and roughly stays at that level in case of Can Tho and Rural1 or even increases further on in case of Ca Mau and Rural2. It is consistently below 0.5 for the PS-only runs.

5.5.2. Discussion

[... The] number of identified PSs decreases steadily with increasing Sentinel-1 observation length in urban as well as rural areas in the VMD. Due to location-dependent differences in urban development and other factors like vegetation growth, the determined ratios are representative for the VMD but can only to a limited extent
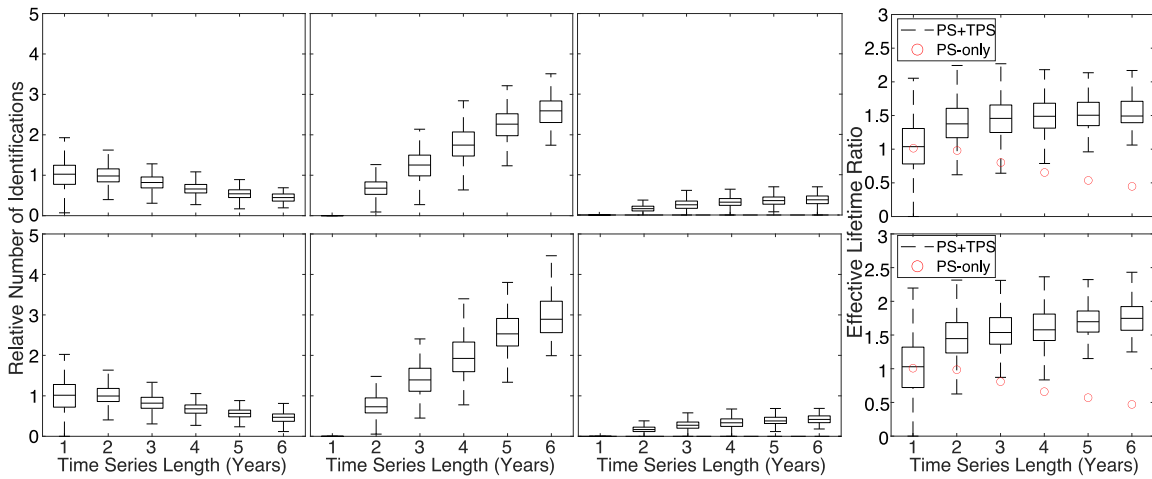
Figure 5.12.: Same as Figure 5.11 in the study areas Rural1 (upper) and Rural2 (lower). © 2022 VDE.

be transferred to other areas. However, the consistent results between urban and rural areas despite large differences in absolute numbers of identified PSs still suggest that the number of PSs will also decrease with increasing time series length at other locations. The main reasons for the decrease in identified PSs are decorrelation, an insufficient assumption of the PS displacement by a simple linear model and construction activities.

The number of identified TPSs compensates in all study areas for the loss of identified PSs with increasing observation lengths. The number of identified TPSs is higher than the reference number of PSs starting with a time series length of three years. This results from the fact that not only fading TPSs are identified, which are assumed to be included in the reference number of PSs, but also other kinds of TPSs which lead to an increase of the total number of observation points on the Earth's surface.

The effective lifetime ratio is the ratio of the effective lifetime of all observation points to the number of reference PSs. It is a measure to describe the relative information content of an observation network. In contrary to the PS-only runs, it first increases for the PS+TPS runs with increasing time series and then stays over 1.5 in all study areas. This shows that the incorporation of TPSs to PSI not only leads to an obvious increase of observation points, but in fact adds a considerable contribution to the PSI based geodetic observation network compared to PS-only runs. If only considering PSs without the AmPSs, the *ELR* drops below 0.5 in all study areas after six-years. In conclusion, we strongly recommend the incorporation of TPSs into PSI algorithms in order to maintain the number of observation points and information content at the highest possible level for long-term monitoring studies.

Depending on the chosen thresholds and confidence levels, there is always a number of AmPSs, i.e. observation points which occur as PSs in the PS-only runs and as TPSs in the joint processing. This set of points describes the intersection between PSs and TPSs where only a small number of acquisitions is discarded. The incorporation

of TPSs in the PSI framework allows to work with a conservative but more reliable network of observation points, where points are temporarily discarded in case of doubt about the temporal coherence.

5.6. Conclusion

TPSs are scatterers which are coherent only in segments of the considered SAR time series. In this section, a robust method was proposed to fully integrate TPSs into M-SBAS. The method extends the previously proposed change date detection algorithms for TPSs, which are solely based on amplitude-statistics, by refining the change dates using a phase-based LRT. The phases of identified PSs and TPSs are jointly unwrapping in a modified version of the unwrapping algorithm in StaMPS. At the end, the temporal datum of those TPSs is re-defined whose lifetime does not cover the selected master scene, which is realized by referencing them to surrounding pixels whose displacement is probably generated by the same underlying process.

We tested the proposed method with a Sentinel-1 data stack of four years length, which was acquired over the city of Ca Mau in the VMD. The integration of TPSs into the PSI algorithm lead to a significant increase in identified observation points. The change date refinement lead to an average increase in the a-posteriori coherence of TPSCs by 0.04 and, in consequence, to an increase of identified TPSs by 7 %. It can be concluded that this step improves the change date detection, thus leads to a robust suppression of noisy scenes in the examined time series of TPSs. An interesting finding is that the change dates of appearing TPSs were almost exclusively postponed by the change date refinement, while those of fading TPSs were almost exclusively were brought forward. The displacement time series of exemplary TPSs after the re-definition of the temporal datum were presented and discussed.

The relevance of the TPS integration for long-term PSI monitoring was examined at the end of the chapter. For this purpose, the ratio of the numbers of identified TPSs to PSs was analyzed as a function of the time series length. Additionally, the lifetime of TPSs was included in the analysis in order to study their actual contribution to the observation point network during the whole observation period. The study was carried out with a Sentinel-1 stack of six years length, acquired over two urban and two rural areas in the VMD. The results agreed very well in all study areas. The number of identified PSs decreased with increasing time series length, while the number of TPSs steadily increased to exceed the number of PSs by far for a time series length of six years. The analysis of the lifetime of the identified TPSs showed that the integration of TPSs not only leads to an increase in identified observation points, but to a significant improvement of the observation network during the whole observation period. In conclusion, we strongly recommend the TPS integration into PSI approaches for long-term monitoring to develop flexible displacement monitoring systems which handle land surface changes and this way provide the best possible PSI-based geodetic observation networks.

6. Application to Subsidence Monitoring in the Vietnamese Mekong Delta

Land subsidence is a global geological phenomenon characterized by a gradual or sudden sinking of the Earth's surface. Major causes are of both man-made and natural origins, namely extraction of fluids leading to sediment and aquifer system compaction (Poland and Davis, 1969; Galloway and Burbey, 2011), underground mining (Bell et al., 2000), oxidation and consolidation of organic soils (Stephens et al., 1984; Deverel and Rojstaczer, 1996), dissolution of carbonate or evaporite rocks leading to sinkholes (Martinez et al., 1998), natural compaction (Meckel et al., 2006; Teatini et al., 2011) and thawing permafrost (Nelson et al., 2001). It can have direct consequences in the form of structural damage (Phien-wej et al., 2006; Wit et al., 2021) as well as indirect environmental consequences as result of the accelerated relative sea level rise, like an increased vulnerability of the affected area to salinization of water resources (Don et al., 2006; Smajgl et al., 2015), flooding (Abidin et al., 2015; Miller and Shirzaei, 2019), erosion (Zou et al., 2016) and finally permanent inundation. Latter problems particularly concern [low-lying] coastal areas [... affected by subsidence]. Syvitski et al. (2009) gave an overview of the relative sea level rise and causes of subsidence in sinking deltas worldwide. Prominent examples are Bangkok, which has been subsiding for the last couple of decades with peak rates of 12 cm/yr (Phien-wej et al., 2006; Aobpaet et al., 2013), Jakarta where the rates are up to 10 cm/yr (Abidin et al., 2015) and the VMD [where rates of up to 5 cm/yr have been reported (Erban et al., 2014; Minderhoud et al., 2020)].

The geodetic monitoring of surface movements, preferably with a high spatial and temporal sampling rate, is crucial for investigating the causes and associated risks of land subsidence and supporting the development and monitoring of reasonable countermeasures. Measured subsidence time series are used to analyze spatial and temporal characteristics of the subsidence and help to better understand the underlying geology and drivers of the subsidence. For example, Wit et al. (2021) have shown that infrastructure with piled foundations is on average characterized by significantly smaller subsidence than their surrounding surface ground in three cities across the VMD, indicating shallow soil compaction above the foundation depth. Subsidence measurements can furthermore be used to enhance, initialize or validate physical subsidence models (Hoffmann and Zebker, 2003; Galloway and Burbey, 2011; Minderhoud

et al., 2017). Finally, the success of countermeasures can be assessed by studying progressing subsidence time series, as shown for Bangkok in Phien-wej et al. (2006).

Different geodetic tools have been used to measure subsidence. Galloway and Burbey (2011) gave an overview of previously used methods and case studies. Most of the mentioned studies evaluated measurements from levelling (Phien-wej et al., 2006; Tosi et al., 2009; Wang et al., 2009), GNSS (Tosi et al., 2009; Abidin et al., 2015) and/or InSAR (Galloway et al., 1998; Hoffmann and Zebker, 2003; Erban et al., 2014). The preferred method nowadays is spaceborne MT-InSAR such as PSI [or DS interferometry] as it is characterized by high spatial sampling, large coverage and usually a sufficiently high temporal sampling rate of several days. Furthermore, there are several sources of free SAR data, such as data from the Sentinel-1 mission, which is run by the European Space Agency (ESA) and designed as a long-term monitoring mission.

Two of the main challenges of PSI have been tackled in this thesis by means of extensions which enable long-term and large-scale displacement monitoring in areas with complex atmospheric conditions. In the following, results from the application of the proposed M-SBAS-2-StaMPS algorithm to subsidence monitoring in the VMD are presented [1]. First, the VMD and regional environmental challenges are introduced. The exploited data and parameter settings of the algorithm are described in the following. Subsequently, the results are presented and discussed in detail, as well as compared to alternative subsidence measurements. At the end of the chapter, a special use case of the TPS integration is presented, in which new buildings are automatically detected and their initial subsidence time series systematically analyzed.

6.1. The Vietnamese Mekong Delta

The VMD is a low-lying delta with an average elevation of 0.8 m above sea level (Minderhoud et al., 2019), which has been prograding for more than 4500 years as a consequence of sediment deposition of the Mekong River into the South China Sea and the Gulf of Thailand (Van Nguyen et al., 2000). Today it is home to about 17 million people and of large significance for the Vietnamese economy due to the local rice production and aquafarming (Cosslett and Cosslett, 2014). A satellite image composite, a map showing the surface normal heights and a land cover/land use map of the VMD are displayed in Figure 6.1. Almost all of the displayed area is covered by sedimentary deposits except for few solid rock outcrops in the north-western part and at the western coast which are elevated above the sedimentary plains. The land use has been changing considerably in the last three decades across the delta (Phan et al., 2021). In 1990, the whole delta was used primary for rice production and crops, while today the delta coast is mainly used for aquafarming.
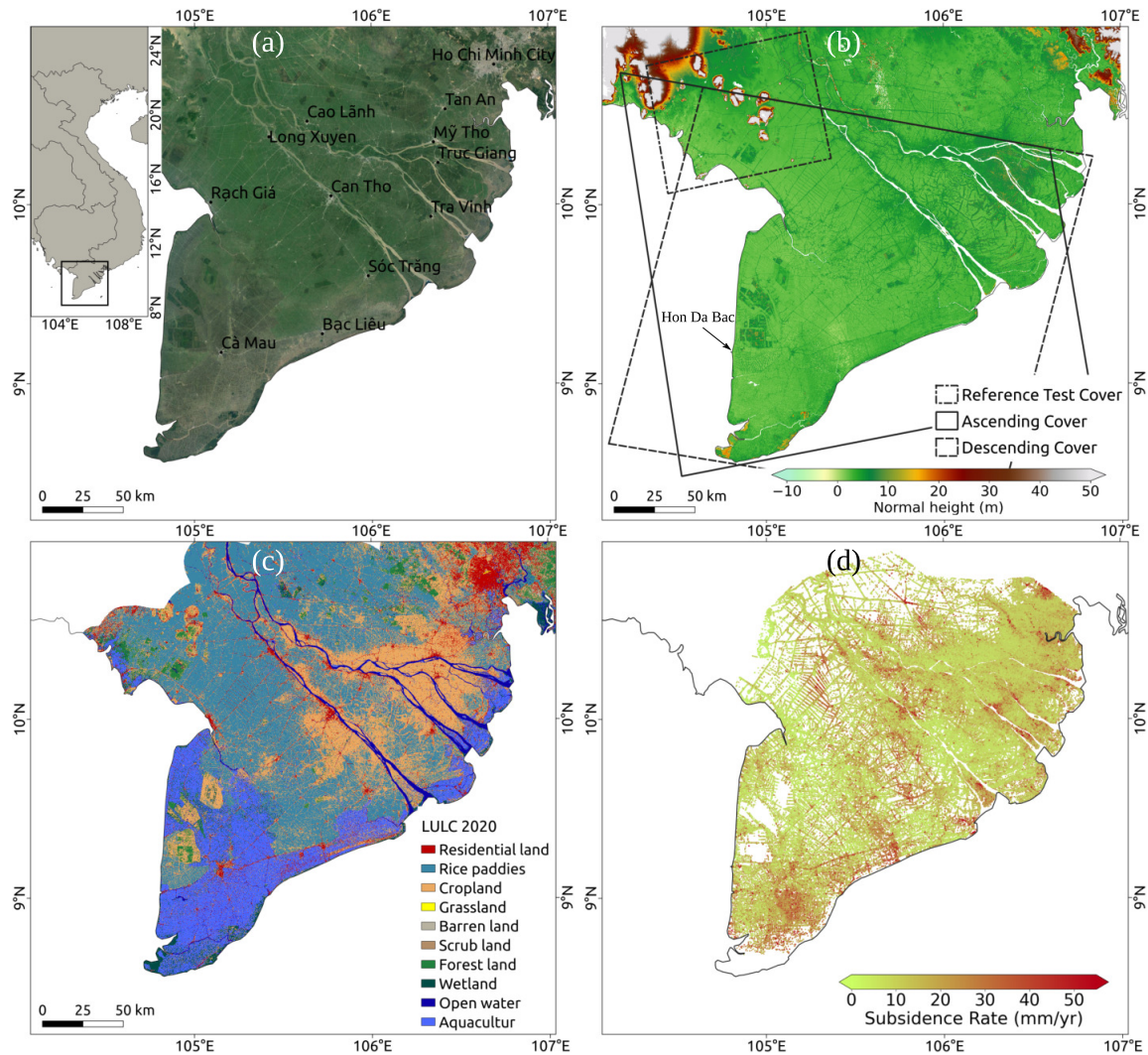
Figure 6.1.: (a) Optical satellite image composite of the VMD with location and names of important cities. Imagery data: Google Earth, © 2023 Maxar Technologies. (b) Normal heights in the VMD calculated with the global TanDEM-X 90 m DEM (Rizzoli et al., 2017) and the EGM2008 gravitational model (Pavlis et al., 2012). The covered area of ascending and descending stacks and the study area used in the referencing test in Section 4.5.3 are also displayed. (c) Land Use/Land cover map of the VMD in 2020 after Phan et al. (2021). (d) Estimated subsidence rates between November 2014 and January 2019 by the company GISAT after an activation of the Copernicus Emergency Management Service (Copernicus, 2019; Minderhoud et al., 2020).

The delta has recently been affected by different environmental challenges, including a decrease of sediment supply due to climatological causes (Darby et al., 2016) as well as anthropogenic causes in the form of dam constructions in the upper Mekong (Kondolf et al., 2014). Further challenges are increased riverbank and coastal erosion (Anthony et al., 2015), as well as saltwater intrusion into surface- and groundwater (Gunnink et al., 2021; Eslami et al., 2021). A major problem is land subsidence [with rates of up to several centimeters per year (Erban et al., 2014; Karlsrud et al., 2020; Minderhoud et al., 2020)], which has been affecting the VMD for more than 15 years. This represents a severe environmental hazard considering the low elevation of the VMD and the additional regional sea level rise of about 3.3 mm/yr (Hak et al., 2016).

Subsidence has been examined based on different methods in order to get the recent magnitude of subsidence and to carry the study of causes of subsidence forward. Erban et al. (2014) presented the first delta-wide subsidence estimates by means of ALOS PALSAR InSAR for the time period of 2006 to 2010 which showed subsidence rates of up to 4 cm/yr over large regions. They compared the measured InSAR rates with modelled compaction rates from a 1D hydrogeological model on the basis of measured hydraulic head drawdown rates in different aquifers, which averaged to 26 cm/yr among the delta. Both results agreed well at head drawdown monitoring stations, and they concluded that the measured subsidence can be attributed to groundwater over-exploitation. These findings were supported by Minderhoud et al. (2017) who developed a delta-wide 3D hydrogeological model with an integrated subsidence module. Their model showed an average subsidence of about 18 cm across the delta between 1991 and 2015 with increasing subsidence rates which amounted up to more than 2.5 cm/yr in 2015. Minderhoud et al. (2018) showed on basis of the results from Erban et al. (2014) that highest subsidence rates are found in land use classes with high human impact, further indicating anthropogenic causes of subsidence.

A more recent Sentinel-1 InSAR study with data acquired between November 2014 and January 2019 was conducted by the company GISAT [... following a Copernicus Emergency Management Service - Mapping activation by the German International Cooperation Agency GIZ and the German Federal Institute for Geosciences and Natural Resources (Copernicus, 2019; Minderhoud et al., 2020)]. The results from that study are displayed in Figure 6.1. They show subsidence rates of up to 5 cm/yr, with the largest rates mainly found in urban areas. Furthermore, they exhibit more variability of subsidence rates at short distances compared to the rather smoothed results by Erban et al. (2014). In general, differential subsidence on short distances can be related to many factors, including loading of structures, previous land cover/land use, local geology and different foundation depths of buildings. Wit et al. (2021) studied differential subsidence in three cities across the VMD and showed that examined buildings with deep foundations going down to 50 m showed on average lower subsidence rates than their surroundings. This indicates significant compaction in shallow sediment layers above the foundation depth of these buildings.

First results from three subsidence monitoring stations on the Ca Mau peninsula were presented in Karlsrud et al. (2020) which measured depth-dependent soil layer

settlement with regard to benchmarks situated in 100 m depth. The maximum subsidence rate from these monitoring stations was 31 mm/yr, which is almost three times larger than the estimated typical settlement rate of ~13 mm/yr in layers below 100 m. They also attributed the measured subsidence to groundwater over-exploitation. A further contribution to subsidence has been discussed in Zoccarato et al. (2018) who showed in a model study that natural compaction rates of young Holocene soil layers can reach up to 20 mm/yr at the coast. This potentially leads to a large additional amount of subsidence as a result from a reduction of sediment supply by the Mekong River.

The exact shares of the various contributions to subsidence and their spatial variations are still not known due to a number of reasons. These include a lack of properly distributed land subsidence observation wells which measure the depth-dependent compaction down to deep soil layers, inaccurately known groundwater extraction rates due to a possible large number of unregistered groundwater extraction wells and insufficient knowledge on the complex geology.

6.2. Data

This study is based on Sentinel-1 data which was acquired in VV-polarization between 2016 and 2022 over the VMD. The data set contains 315 scenes acquired between April 2016 and April 2022 in descending orbit and 115 scenes acquired between April 2017 and March 2022 in ascending orbit. The mean temporal difference between consecutive scenes is 7 days in the descending stack and 15.8 days in the ascending stack. Two consecutive Sentinel-1 swaths, recorded in the Interferometric Wide Swath Mode, were assembled in each orbit to cover a large part of the VMD. The footprint on land of both stacks is displayed in Figure 6.1 and is about 250 km×230 km in both stacks. The incidence angle varied approximately between 30 ° and 45 ° in the covered area in both stacks. The SNAP software by the ESA was used for the interferometric preprocessing, which included coregistration with Enhanced Spectral Diversity (Yague-Martinez et al., 2016) as well as the subtraction of simulated flat-earth and topographic phase based on the global TanDEM-X 90 m DEM (Rizzoli et al., 2017).

The selected master scenes of descending and ascending stacks are February 1st, 2021 and December 22, 2020, respectively. The mean perpendicular baseline $B_\perp$ of the scenes with respect to the master scenes as well as the surface temperature in the city of Can Tho (Figure 6.1) at the acquisitions, taken from the ERA-5 reanalysis, are displayed in Figure 6.2. The local time at descending and ascending acquisitions was 5:45 am and 6:11 pm, respectively. The standard deviations of the interferometric baselines (Table 6.1) determine the Cramér-Rao Lower Bound (CRLB) of the estimation of the parameters considered in M-SBAS, which are the residual height h, the linear displacement rate v and the thermally induced displacement rate α of (T)PSs. The functional models of the phase due to these parameters are given in Equations 2.23,
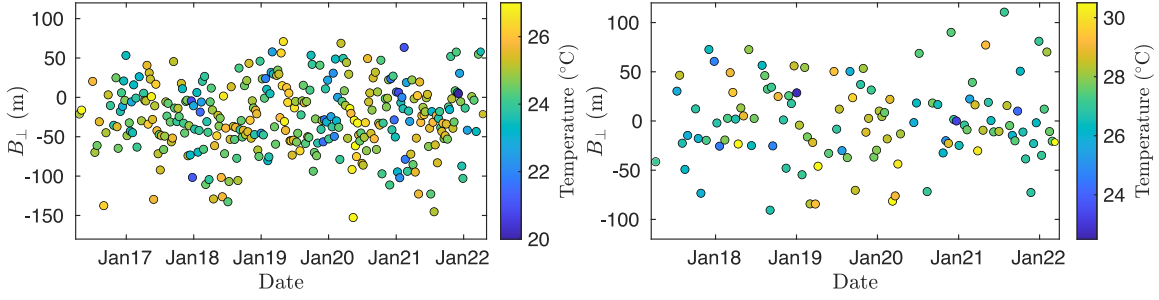
Figure 6.2.: Mean perpendicular baseline $B_\perp$ with respect to the master scene and surface temperature at acquisition of (a) descending and (b) ascending stack in the city of Can Tho. The temperature was taken from the ERA-5 reanalysis.

Table 6.1.: Magnitude of the expected maximum of the parameters v, h and α, standard deviation of the three associated baselines τ, $B_\perp$ and ϑ in both stacks and CRLB of the estimations of the parameters for a PS with SNR = 2. The values are based on sensor parameters and surface temperatures in the city of Can Tho.

Parameter	h	v	α
Expected maximum	$10^2\,\mathrm{m}$	$10^2\,\mathrm{mm/yr}$	$10^0\,\mathrm{mm/K}$
Associated baseline	$B_\perp$	τ	ϑ
Standard deviation of baselines	$\sigma_{B_\perp}^{\mathrm{DESC}} = 42.8\,\mathrm{m}$ $\sigma_{B_\perp}^{\mathrm{ASC}} = 40.5\,\mathrm{m}$	$\sigma_\tau^{\mathrm{DESC}} = 567\,\mathrm{d}$ $\sigma_\tau^{\mathrm{ASC}} = 512\,\mathrm{d}$	$\sigma_\vartheta^{\mathrm{DESC}} = 1.2\,\mathrm{K}$ $\sigma_\vartheta^{\mathrm{ASC}} = 1.4\,\mathrm{K}$
CRLB of parameter estimation	$\sigma_{\hat{h}}^{\mathrm{DESC}} = 1.6\,\mathrm{m}$ $\sigma_{\hat{h}}^{\mathrm{ASC}} = 2.9\,\mathrm{m}$	$\sigma_{\hat{v}}^{\mathrm{DESC}} = 0.08\,\frac{\mathrm{mm}}{\mathrm{yr}}$ $\sigma_{\hat{v}}^{\mathrm{ASC}} = 0.15\,\frac{\mathrm{mm}}{\mathrm{yr}}$	$\sigma_{\hat{\alpha}}^{\mathrm{DESC}} = 0.11\,\frac{\mathrm{mm}}{\mathrm{K}}$ $\sigma_{\hat{\alpha}}^{\mathrm{ASC}} = 0.15\,\frac{\mathrm{mm}}{\mathrm{K}}$

3.4 and 3.5. The CRLB of the height estimation of PSs in M SAR acquisitions is given by (Bamler et al., 2009)

$$\sigma_{\hat{h}} = \frac{\lambda R \sin\theta_0}{4\pi\sqrt{M}\sqrt{2\mathrm{SNR}}\sigma_{B_\perp}}, \tag{6.1}$$

where $\sigma_{B_\perp}$ denotes the standard deviation of the perpendicular baseline distribution. The CRLBs of the two other parameter estimations can be derived accordingly, taking their particular functional model into account. The CRLB of the height estimation is depending on the pixel location as results of the dependency on the range and satellite look angle. The CRLB of all parameter estimations are listed in Table 6.1 for a PS with SNR = 2 and the two stacks, considering the sensor parameters as well as surface temperatures in the city of Can Tho. It is $1.3\,\mathrm{m}$ and $2.2\,\mathrm{m}$ for the height estimation, $0.08\,\mathrm{mm/yr}$ and $0.15\,\mathrm{mm/yr}$ for the displacement rate estimation and $0.11\,\mathrm{mm/K}$ and $0.15\,\mathrm{mm/K}$ for the estimation of the thermally induced displacement rate, respectively. Relating these values to the anticipated order of magnitude of each parameter, the estimation of the displacement rate is expected to exhibit the highest performance. The uncertainties of the height and the thermally induced

displacement rate estimations are larger due to the small diameter of the orbital tube of the Sentinel-1 mission and the small temperature variability in the study area.

The estimation of the thermally induced displacement rate in M-SBAS is only necessary if the phase variance due to thermally induced displacement rates is large so that it leads to considerable noise and compromises the PS identification if not accounted for. In our case, the interferometric phase variance due to thermally induced displacements is small. Considering the standard deviation of $1.4\,\mathrm{K}$ in the ascending stack and assuming a pixel with a thermally induced displacement rate of $\alpha = 1\,\mathrm{mm/K}$, the resulting phase standard deviation would be

$$\sigma_{\varphi_\alpha} = \frac{4\pi}{\lambda}\alpha\sigma_\vartheta = 0.31\,\mathrm{rad}. \tag{6.2}$$

The assumed rate of $1\,\mathrm{mm/K}$ is a rather large value for thermally induced displacement rates and only found on large infrastructure with large coefficients of thermal expansion (Monserrat et al., 2011; Fornaro et al., 2013). This means that the phase standard deviation due to thermally induced displacement rates is expected to be in the range between 0 and $0.31\,\mathrm{rad}$. As a result, we do not expect this signal to lead to considerable noise and substantially compromise the PS identification and neglect its estimation, resulting in a reduction of the computational costs by $1/3$ during the phase noise estimation.

The first step of reducing SCN in unwrapped interferograms in M-SBAS-2-StaMPS is the correction of modelled tropospheric delays, tidally induced displacements and plate motions. Variograms of interferograms with short temporal baselines in both data stacks before and after the corrections of modelled tropospheric delays and tidally induced displacements are compared in Figure 6.3. The difference in the variograms before and after the correction of plate motions is not shown here, as the signals are negligible at short temporal baselines. The mean variograms applying no corrections approach $6.7\,\mathrm{cm}^2$ and $12.2\,\mathrm{cm}^2$ at large distances in the descending and ascending stack, respectively. Single variograms go up to $93\,\mathrm{cm}^2$ and $84\,\mathrm{cm}^2$ in the stacks. The mean variograms after the correction of modelled tidal displacements approach $5.9\,\mathrm{cm}^2$ and $11.8\,\mathrm{cm}^2$ at large distances, while the mean variograms after the correction of modelled tidal displacements and tropospheric delays approach $5.2\,\mathrm{cm}^2$ and $7.8\,\mathrm{cm}^2$ at large distances. Single variograms after the full correction go up to $62\,\mathrm{cm}^2$ in the descending stack, whereas only up to $23\,\mathrm{cm}^2$ in the ascending stack. The mean variogram gain (Equation 4.28) provided by the corrections is displayed in Figure 6.3 (d). It can be seen that while the [... mean] variogram before and after the corrections is lower at all distances in the descending stack compared to the ascending stack, the gain provided by the corrections is larger in the ascending stack. The gain from the full correction reaches about -1.2 and $-1.9\,\mathrm{dB}$ at $150\,\mathrm{km}$ in the descending and ascending stack, respectively. The larger variogram values in the ascending stack are probably related to high water vapor content and variability at local acquisition time. Solar radiation leads to evaporation during the day and the diurnal rain cycle in the rainy season is usually characterized by an increased frequency of rainfall events in the evening in the lower Mekong Basin (Kumiko et al., 2008). Additionally, Liang et al.
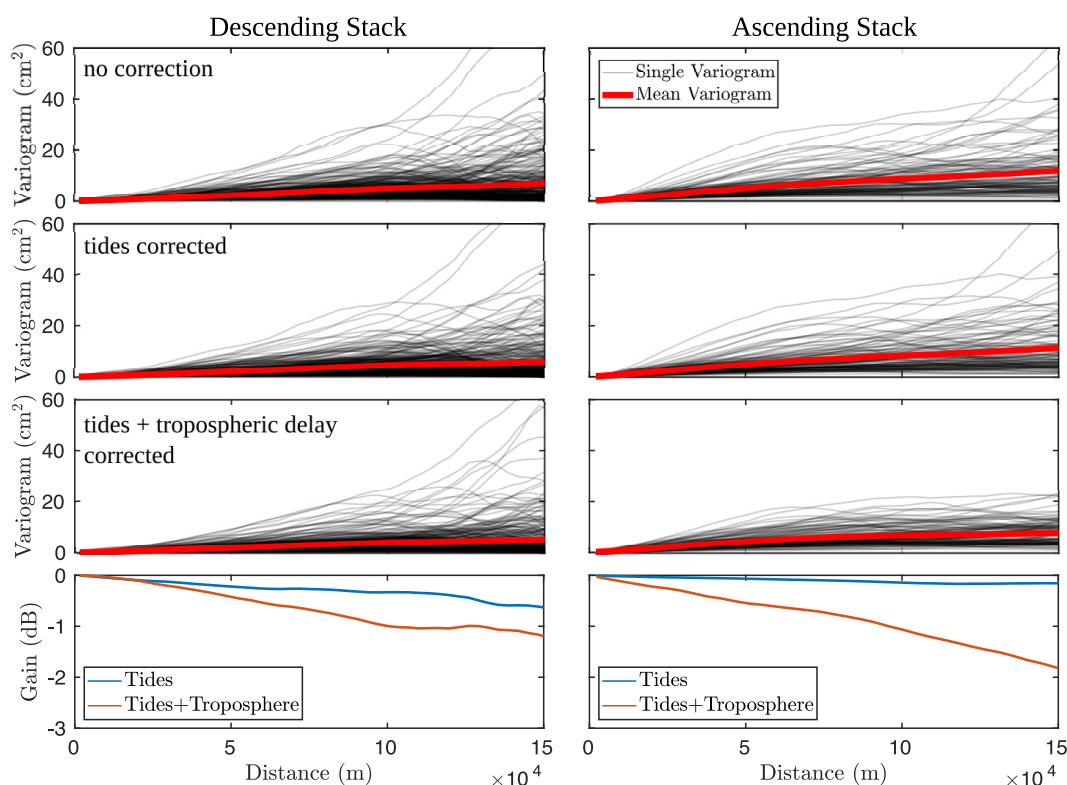
Figure 6.3.: Single and mean variograms of interferograms with small temporal baselines before and after geodetic corrections in the descending and ascending stack, as well as mean variogram gain provided by the corrections.

(2019) showed that ionospheric effects on MT-InSAR can be strong for ascending data acquired in low-latitude areas such as the VMD, while descending data is largely unaffected. The different impact of the ionosphere on the stacks originates in the different times of day at acquisition. However, a visual inspection of the interferograms revealed that the residual noise is mainly characterized by smaller wavenumbers than expected from ionospheric delays. This led us to the conclusion that differences in the residual noise in both stacks is mainly due to insufficient tropospheric delay modelling.

6.3. Methods and Parameter Settings

The proposed M-SBAS-2-StaMPS algorithm was applied with following essential parameter settings. The amplitude threshold for PSCs to be selected was set to 0.47. A minimum duration of 25 consecutive acquisitions was demanded for a coherent or incoherent TPS segment to be identifiable. The coherence threshold for the PS and TPS selection was empirically determined as described in Section 5.3.2. For the joint phase unwrapping of selected TPSs and PS, an unwrapping grid size of 500 m was chosen.

The unwrapped phases of selected PSs and TPSs were neither filtered nor detrended. The interferometric phases in LOS were projected to the vertical, making use of the local incidence angle. This projection was done under the assumption that displacements in the VMD are exclusively vertical, as also assumed in Erban et al. (2014) and Copernicus (2019). At the end, the phase time series were converted to displacement time series as described in Equation 2.24. In the following, downward vertical displacement is defined as positive subsidence.

6.4. Reference Areas

The considered geodetic corrections, comprising the correction of modelled tidal displacements, tropospheric delays and plate motions, reduce the SCN in interferograms on average, but not to a reasonable magnitude in order to be able to properly monitor displacements with an expected maximum magnitude of $10\,\text{cm/yr}$. This is probably due to a mediocre performance of the tropospheric delay modelling based on the ERA-5 reanalysis, as a consequence of the low latitude and flat topography of the study area(Cong et al., 2018; Liu et al., 2009). We presented a method to reduce residual SCN in interferograms by integrating reference points with known displacement time series in Section 4.5. However, displacement ground truth is sparse in the VMD. To our knowledge, there is only one permanent GNSS station located in Bac Lieu (Vu et al., 2020) whose data is not freely available. Measurements from repeated levelling campaigns are also not freely available. The only areas with presumably zero subsidence during the considered time period are solid rock outcrops located in the north-western part of the delta and a small outcrop island which is called Hon Da Bac and located at the western coast of the VMD (Figure 6.1). The spatial distribution of these outcrops is poor, and there are pixels which are located more than $160\,\text{km}$ away from the nearest outcrop. The variograms indicate that points at this distance are not spatially correlated, i.e. the application of the noise kriging method from Section 4.5 will not improve the uncertainty at these pixels, compared to removing the mean phase of all pixels located on the outcrops.

For the mentioned reason, we selected additional reference PSs which are located on large bridges with lengths over 250 m. The motivation behind consists of several factors:

- Large bridges feature deep piled foundations with pile length of up to $73\,\text{m}$ (personal communication from Renck, A., 2021), thus should be only affected by potential subsidence originating from deeper soil layers. Wit et al. (2021) showed that buildings with pile foundations are more stable than their surroundings in three cities in the VMD, indicating a considerable contribution of shallow soil layer compaction to the total subsidence. It has to be kept in mind that solely subsidence above the foundation depth of the bridges can be measured if pixels on these bridges are selected as reference, with zero displacements assumed.

Figure 6.4.: Photograph of a bridge in the VMD featuring the characteristic street bump at its border. The photograph was kindly provided by Andreas Schenk.

- Relative movements of the bridges at acquisition, e.g. induced by vehicle crossings, can be canceled out by averaging the sampled interferogram noise over multiple PSs distributed along the bridges. Residual relative movements as well as potential unmodelled thermally induced displacements lower the coherence of PSs on the bridges. As a result, these effects are considered in the stochastic model of the noise screen estimation in the form of variances of the PSI derived displacements σ_{PSI}^2 of the reference points (Section 4.5.1).

- Subsiding or horizontally moving bridges can be identified in a triangulation network between all selected reference areas and a combination of ascending and descending stacks. They are removed from the set of reference bridges.

The fact that many larger bridges are more stable than their surroundings can be experienced in the field when driving by car onto the bridges. Their onset usually features a characteristic street bump, which has been caused by the surroundings of the bridge being subsiding at a higher rate than the bridges themselves. An example of such a bump can be seen in Figure 6.4. We systematically examined this in a preliminary study by evaluating the differential subsidence between bridges and their surroundings. The study was first presented in Dörr et al. (2021) with a preliminary PSI approach and was repeated with the M-SBAS-2-StaMPS for this thesis.

For the study, (T)PS pixels located on the solid rock outcrops were selected as reference pixels and only data from the descending stack was used. The location and length of bridges in the VMD was extracted from Open Street Map (OSM), which provides the geolocation of bridges as polyline vector features. We extracted bridges with a length greater than 50 m as we expect those bridges to have a pile foundation. We computed buffers of 10 m around the polyline features with flat end-caps, which we refer to as bridge polygons [...]. The data set partly covers both roadsides of bridges separately, which we automatically corrected by dissolving overlapping bridge polygons. Larger buffers of 500 m were created to define the surroundings of the bridges. (T)PSs located in the bridge polygons were selected as Bridge-(T)PSs, while (T)PSs located in the larger polygons with an estimated height of less than 10 m above ground were selected
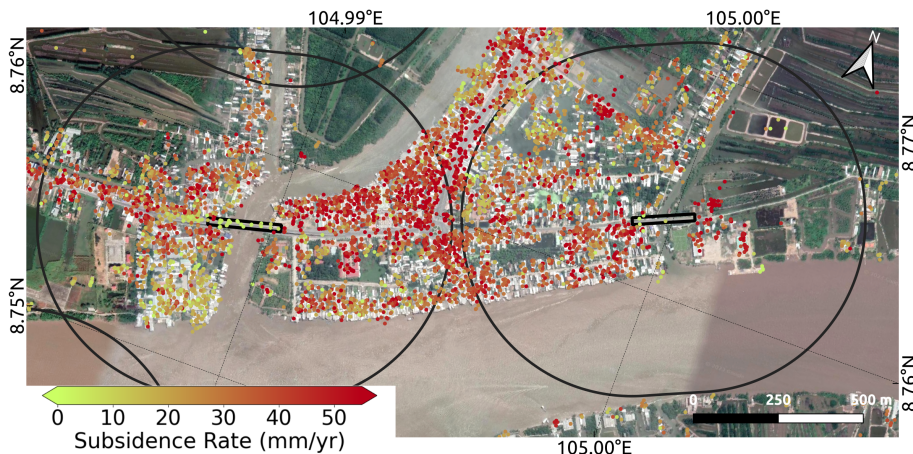
Figure 6.5.: Polygons of two bridges and their 500 m radius surroundings on the Ca Mau Peninsula overlaid by estimated subsidence rates of identified observation points, referenced to the solid rock outcrops. Map data: Google, © CNES/Airbus, Maxar Technologies.

as surrounding Ground-(T)PSs. The height threshold was introduced to filter out PSs on higher buildings which are likely to have a foundation themselves. Two examples of bridge polygons and their surroundings are displayed in Figure 6.5. Identified (T)PSs on both bridges feature significantly lower subsidence rates than the mean of their surroundings.

We only considered bridges which more than three Bridge-PSs were identified on. The subsidence rate of the bridges was estimated using the weighted median of all Bridge-(T)PSs, with weights proportionally to the inverse of their distance to the bridge center. The weighting was carried out because the probability of surrounding (T)PSs being falsely located within the bridge polygons increases towards the edges of the polygons. The subsidence of the surrounding ground was calculated using the median of the identified Ground-(T)PS. We refer to the difference between the subsidence rates of the bridge and the surrounding ground surface as differential subsidence rate.

The OSM data set features 52417 bridges in the VMD with 2506 being longer than 50 m. 397 bridges were selected for the study of differential subsidence rates, as more than three Bridge-(T)PSs were identified on these. The estimated subsidence rates of the bridges and their surroundings as well as a histogram of the differential subsidence rates are displayed in Figure 6.6. 86 % of the bridges are characterized by lower estimated subsidence rates than their surroundings. The minimal differential subsidence rates is -37 mm/yr. 72 % of the bridges exhibit subsidence rates of less than 5 mm/yr, while this only applies to 17 % of bridge surroundings. It has to be mentioned that the estimated absolute subsidence rate has considerably higher uncertainty than the differential subsidence rate in most cases due to the distance of the bridges to the solid rock outcrops. The 5 % quantile of the estimated bridge subsidence rates is -4.1 mm/yr, indicating an uplift for some bridges which we do
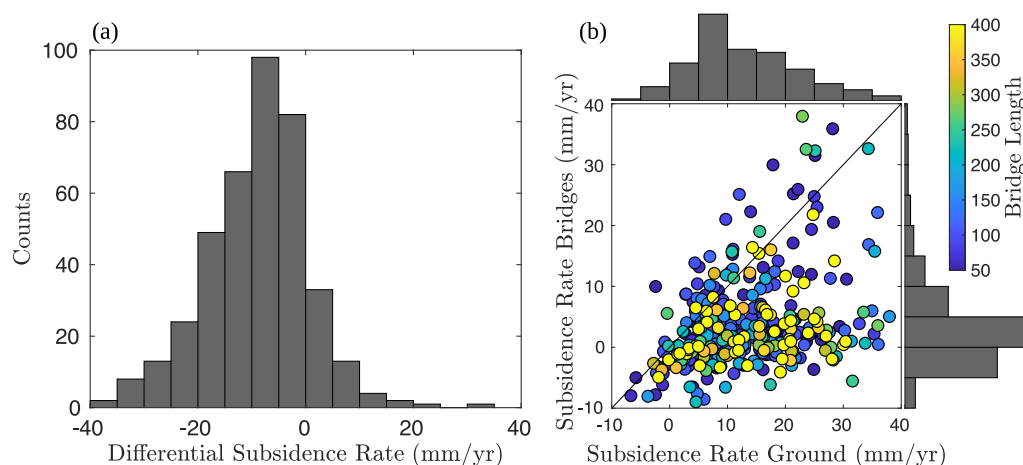
Figure 6.6.: (a) Histogram of differences in estimated subsidence rates of selected bridges and their surrounding ground surface using the solid rock outcrops as reference areas. (b) Comparison of estimated subsidence rates with respect to bridge length.

not expect in the region. We assume that this is caused by temporally correlated residual SCN in the data and partially by horizontal movements of the bridges, such as tilts toward the LOS direction. A few bridges exhibit higher subsidence rates as their surroundings. Possible reasons for that are: (i) The bridge has no or shallow foundation and the additional load of the bridge leads to an increased subsidence rate. (ii) Buildings with deep foundations were included in the set of Ground-(T)PSs which decreased the averaged subsidence rate of the bridge surrounding. (iii) (T)PSs were falsely classified as Bridge-(T)PSs.

The observation that most of the bridges are characterized by a lower estimated subsidence rate than their surroundings fits those from Wit et al. (2021). This indicates that a substantial part of the total subsidence originates in soil layers above the foundation depth of the bridges. For this reason, we selected bridges with lengths longer than 250 m as potential reference areas in the following. The median of the estimated subsidence rate of these bridges is 1.5 mm/yr, while the median subsidence of their surroundings is 15.4 mm/yr. The length threshold was set considering the trade-off between proper distribution of references in the study area and length of the bridges, which we assume to be correlated with the foundation depth up to a certain degree.

For the selection of the final reference (T)PSs on the bridges, various statistical tests were carried out with the goals to (i) identify and remove (T)PSs which are actually not located on the bridges or located on parts of the bridges which are actually moving over time, (ii) identify and remove bridges which are subsiding or moving horizontally. Parts of the tests were realized in triangulation networks which were spanned between the potential reference areas. Horizontal movements were studied by combining measurements from descending and ascending orbits. The detailed list of the statistical tests is given in the Appendix A.1.
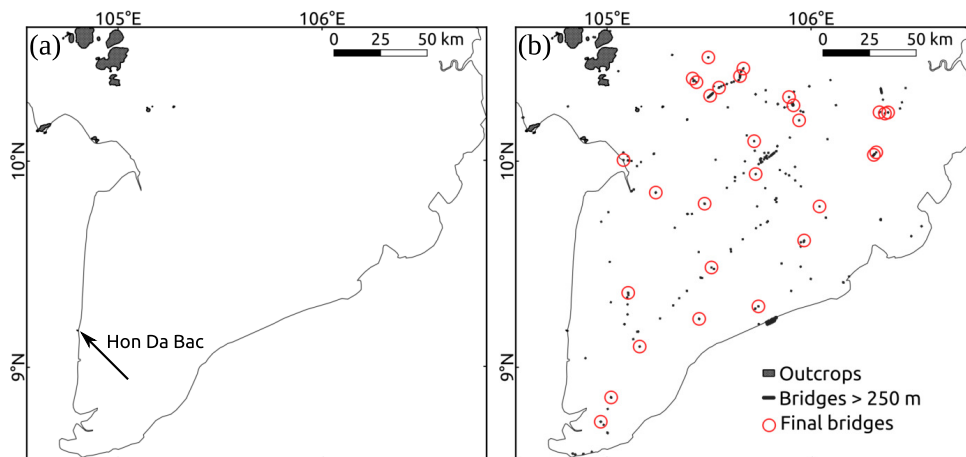
Figure 6.7.: Reference areas in the two referencing scenarios. (a) Referencing scenario 1 only consists of solid rock outcrops. (b) Referencing scenario 2 includes additionally selected bridges with lengths of more than 250 m. The island Hon Da Bac was removed from the set of reference areas in the hypothesis tests for referencing scenario 2.

In the following section, the results from two referencing scenarios will be compared. The reference areas in both scenarios are displayed in Figure 6.7. In referencing scenario 1, the set of reference areas only comprised the solid rock outcrops, while selected bridges were added to the reference areas in scenario 2. The observation points on the outcrop island Hon Da Bac were removed from the set of reference pixels in reference scenario 2, because they did not pass the statistical tests which checked the stability of the potential reference areas. This might be related to the physical origin of the scatterers on the island. They are located on the rocky coast of the island, which is potentially affected by displacements due to waves, tides or wind.

6.5. Results

The proposed algorithm with the mentioned parameter settings identified a high density of observations points across the study area. It identified 7 918 109 observation points in the descending stack, which is the sum of 6 475 848 TPSs and 1 442 261 PSs, while 5 705 582 measurement points were identified in the ascending stack from which 3 109 055 and 2 596 527 are TPSs and PSs, respectively. The numbers of identified TPSs with regard to their TPS type are listed in Table 6.2. The share of appearing TPSs in the total number of identified TPSs is largest in both stacks, which is probably due to the high construction activity in the VMD. The ratio of identified TPSs to PSs in the descending stack is comparable with the findings in Section 5.5, which were based on descending data of six years length in the cities of Can Tho and Ca Mau and two rural areas. The ratio differs in the ascending stack. We assume that the difference in the number of identified (T)PSs in both stacks is due to [... three] reasons. First, the noise level in the ascending stack is on average higher than in

Table 6.2.: Number of identified PSs, TPSs and specific TPS types in the descending and ascending data stacks.

	Descending	Ascending
# PSs	1 442 261	2 596 527
# TPSs	6 475 848	3 109 055
# appearing TPSs	2 531 320	1 755 916
# fading TPSs	1 189 116	948 933
# visiting TPSs	1 399 540	294 934
# recurring TPSs	1 355 872	109 272

the descending stack, which is described in Section 6.2 and potentially leads to a decreased number of identified observation points. Second, the covered time period by the ascending stack (April 2017 - April 2022) is one year shorter than that by the descending stack (April 2016 - April 2022). TPSs which were active only until April 2017 could not be identified in the ascending stack. About 106,200 fading TPSs were identified in the descending stack, whose coherent segment only lasted until April 2017. [... The last reason is that] the ascending stack only consists of 115 SAR scenes with an average temporal difference of 15.8 days between consecutive scenes, compared to the descending stack, which consists of [... 315] scenes with an average temporal difference of 7 days between consecutive scenes. One processing parameter of the TPS identification is the minimum number of consecutive acquisitions that a TPS has to be coherent or incoherent in order that the change dates describing this segment can be identified. This parameter was set to 25 in the analysis. As a result, a coherent TPS segment has to be, on average, at least 395 days in the ascending stack in order to be identifiable, compared to 175 days in the descending stack. About 1.3 million TPSs with a total coherent period of less than 395 days were identified in the descending stack. We assume that the different PS to TPS ratios in both stacks are also constituted in that fact, since TPSs with short incoherent segments are more likely to be falsely identified as PSs in the ascending stack compared to the descending stack.

In the following, the estimated subsidence rates in both stacks are compared. The temporal evolution of the subsidence rates is examined and exemplary subsidence time series are shown. Subsequently, a special use case of the TPS integration into PSI is presented. It is shown that the TPS integration not only significantly improves the observation point network, but provides additional information by means of change dates of TPSs, which can be used for change detection. The time series of appearing TPSs after their appearance is exploited to systematically analyze the initial settlement of automatically identified new buildings.

6.5.1. Overview of Estimated Subsidence

The estimated subsidence rates in both stacks for the time period between April 2017 and April 2022 are displayed in Figure 6.8, using only the solid rock outcrops as

Table 6.3.: Basic statistics of the results in the overlapping area of descending and ascending stack for the two referencing scenarios: (1) referencing solely to solid rock outcrops and (2) adding selected bridges as additional reference areas. The statistics of the estimated rates are based on the overlapping time period of April 2017 until April 2022.

	Desc. (1)	Asc. (1)	Desc. (2)	Asc. (2)
5 % Rate Prctile (mm/yr)	-1.6	-5.4	-1.5	-3.1
Median Rate (mm/yr)	8.6	6.3	8.0	6.8
Mean Rate (mm/yr)	10.8	9.0	10.3	9.1
95 % Rate Prctile (mm/yr)	30.5	32.3	29.7	29.2
Mean Std. Rate Est. (mm/yr)	1.2	2.3	0.5	1.2
Mean Std. Sub. Est. (mm)	28.1	35.6	10.9	17.5

reference areas (referencing scenario 1) as well as using the modified reference area set, characterized by selected bridges as additional reference areas and the removal of Hon Da Bac from the reference (referencing scenario 2). The estimated standard deviation of subsidence (Equation 4.26) and rate estimates (Equation 4.27) are also displayed in that Figure. For the sake of consistency in the displayed results, only (T)PSs which cover the whole period of April 2017 to April 2022 are displayed. Furthermore, the observation points were thinned out to a maximum density of 50 points per square kilometer. Lastly, the points were sorted in the way that those with highest subsidence rates overlay points with smaller rates. Table 6.3 provides basic statistics of the results in the overlapping area of ascending and descending stack, in addition to their spatial visualization.

The estimated subsidence rates are characterized by a high heterogeneity on short as well large scales. In referencing scenario 1, small-scale variations in the estimated subsidence fields feature similar characteristics in both stacks, with highest rates of more than 6 cm/yr mainly found in urban areas such as the cities of Can Tho, Bac Lieu and Ca Mau. There are, however, significant long-wave differences between the results of both stacks, which are especially noticeable on the southern peninsula. The estimated rates of observation points south of 9.18 ° N are on average 8 mm/yr larger in the ascending than in the descending stack. The median and mean estimated subsidence rates in the whole spatial overlap of both stacks are 8.6 mm/yr and 10.8 mm/yr in descending and 6.3 mm/yr and 9 mm/yr in the ascending stack. The 5 %- and 95 % percentiles of the estimated subsidence rates are -1.6 mm/yr and 30.5 mm/yr in the descending and -5.4 mm/yr and 32.3 mm/yr in the ascending stack. The estimated negative subsidence rates at parts of the observation points suggest an uplift, which we do not expect in the area. This could be a result of residual temporally correlated SCN, unwrapping errors or large outliers, leading to a biased rate estimation. Horizontal movements of sporadic pixels towards the sensor also potentially contribute to this observation, e.g. caused by tilts of buildings. The estimated standard deviations of the subsidence estimates increase with increasing distance from the solid rock outcrops, and their mean is 28.1 mm in the descending
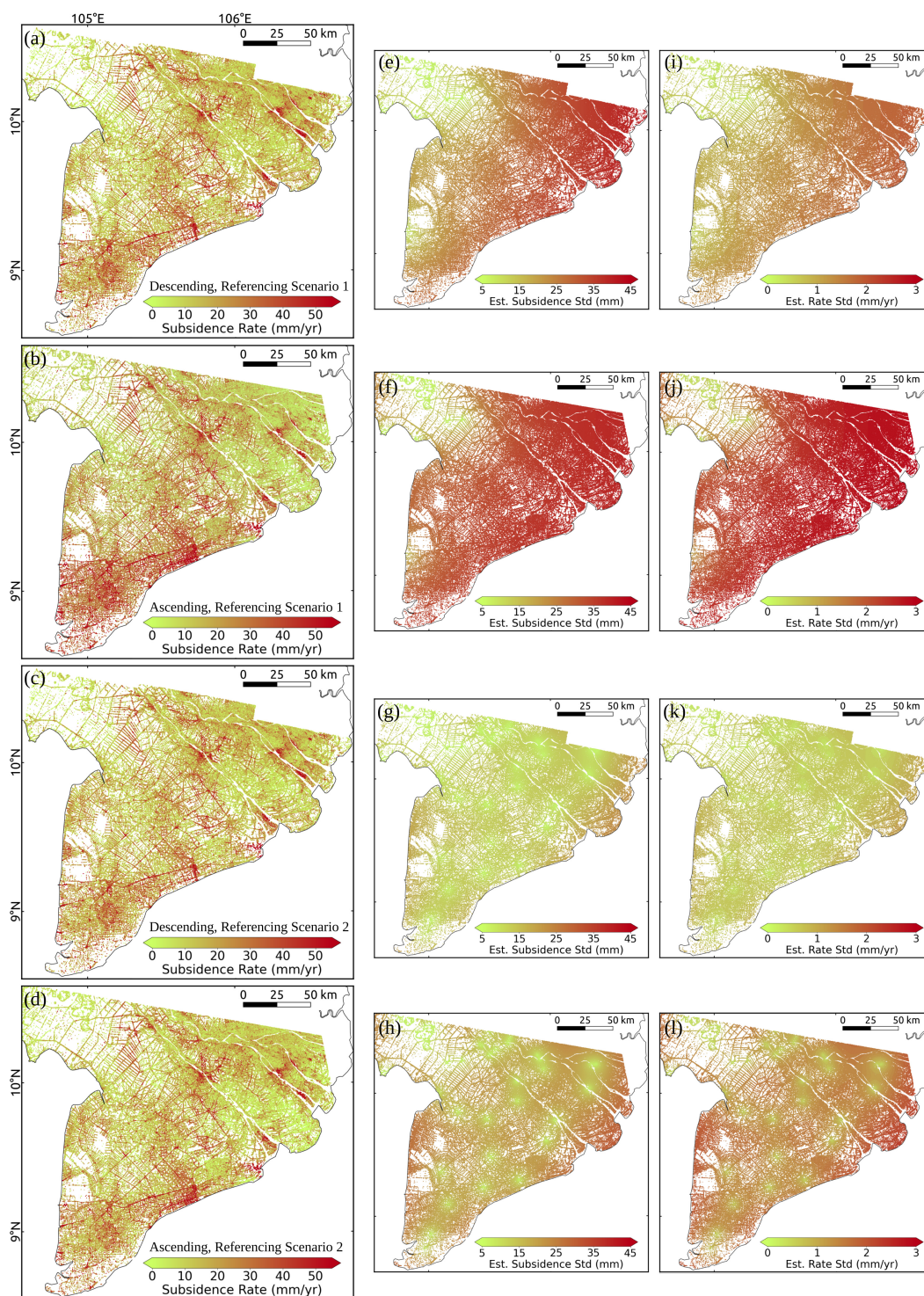
Figure 6.8.: (a)-(b) Estimated subsidence rates between April 2017 and April 2022 in the descending and ascending stack, respectively, using only solid rock outcrops as reference areas. (c)-(d) Same as (a)-(b) but using selected bridges as additional reference areas. (e)-(h) Estimated subsidence standard deviations. (i)-(l) Estimated standard deviation of the subsidence rates. Only (T)PSs which cover the whole period of April 2017 to April 2022 are displayed in all subfigures.

and 35.6 mm in the ascending stack. The error propagation into the rate estimation yields mean standard deviations of the rate estimation of 1.2 mm/yr and 2.4 mm/yr in the stacks, respectively. The difference has its origin in the different noise levels and the different number of acquisitions in the stacks.

The estimated subsidence rates in both stacks agree to a much higher degree in referencing scenario 2 compared to referencing scenario 1. The rates south of 9.18 ° N diverge only by 0.15 mm/yr on average between both stacks. The median and mean estimated subsidence rates in the whole spatial overlap of both stacks are 8.0 mm/yr and 10.3 mm/yr in the descending and 6.8 mm/yr and 9.1 mm/yr in the ascending stack. The 5 %- and 95 % percentiles of the estimated rates are -1.5 mm/yr and 29.7 mm/yr in the descending and -3.1 mm/yr and 29.2 mm/yr in the ascending stack. As a result, the percentage of observation points characterized by negative subsidence rates decreased by adding the selected bridges as reference areas. The estimated mean standard deviation of the subsidence estimates is 10.9 mm and 17.5 mm in the stacks, respectively, and the mean standard deviations of the subsidence rate estimation are reduced to 0.5 mm/yr and 1.2 mm/yr, i.e. are approximately halved compared to referencing scenario 1.

In order to study the difference between the results from both stacks in more detail, we calculated the difference between gridded subsidence rates for the time period between April 2017 and April 2022. The gridding was realized by calculating the median rates of all (T)PSs, which were active in the considered time period, in grid cells of 500 m × 500 m size. The differences between the estimated rates from both stacks are displayed in Figure 6.9. The differences feature a linear trend in ground range direction of the ascending geometry in referencing scenario 1, which ranges from about -8 mm/yr in the south-west to 10 mm/yr in the north-east and is removed in referencing scenario 2. This indicates that the residual SCN in the data stack in referencing scenario 1 contains temporally correlated signals, leading to a bias of the estimated rates and a spatial ramp in the differences between the results from the descending and ascending stack. An alternative reason behind the trend in referencing scenario 1 would be horizontal movements. A combination of the observations from both stacks to separate vertical displacements and horizontal displacements in east-west direction (Fuhrmann and Garthwaite, 2019) would suggest a trend of horizontal displacements ranging from about -10 mm/yr in the south-west to 7 mm in the north-east, which is very unlikely on these spatial scales in a sedimentary delta after the a-priori reduction of plate motions. As stated before, the variances of the rate estimation are underestimated if unconsidered temporal correlations persist in the residual SCN, which explains why the spatial trend in the differences is outside the estimated 2σ uncertainty interval, even if the trend is caused by noise. The 2σ uncertainty interval is based on the estimated standard deviations of the rate difference estimation, which were calculated by propagating the estimated standard deviations of the rate estimates (Figure 6.8) into the calculation of the rate differences. They are also displayed in Figure 6.9.

The temporally correlated noise can be effectively mitigated in large parts of the study area in referencing scenario 2, leading to the removal of the trend in the differences.
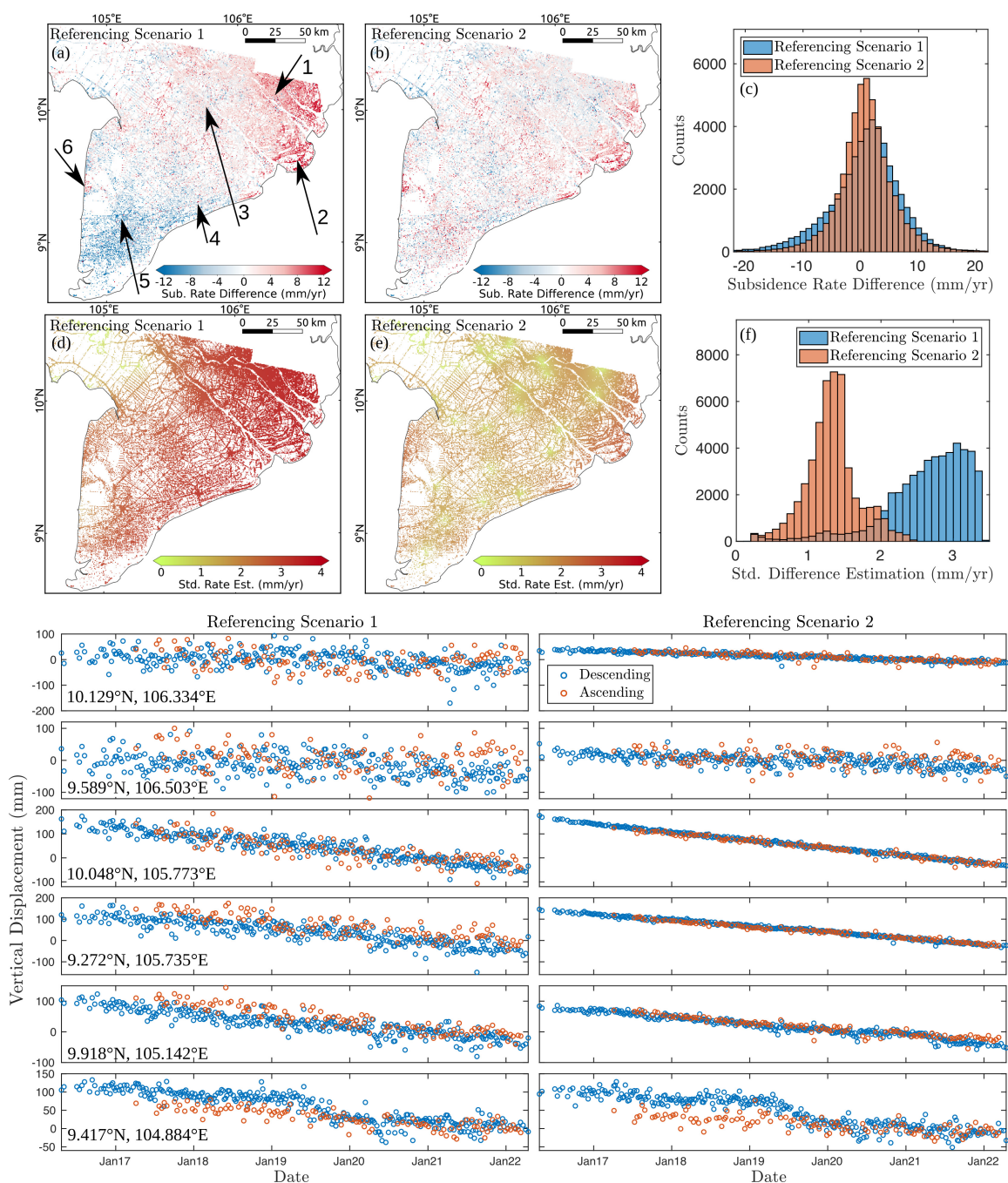
Figure 6.9.: (a)-(c) Differences in estimated subsidence rates from descending and ascending stack for both referencing scenarios. The rates were spatially gridded by calculating the median of estimated rates of observation points inside grid cells of $500\,\mathrm{m} \times 500\,\mathrm{m}$. (d)-(f) Estimated standard deviation of the rate difference estimations between both stacks in both referencing scenarios. Below: Mean subsidence time series for all (T)PSs in a radius of $500\,\mathrm{m}$ around the six locations indicated by arrows in (a) in both referencing scenarios.

However, there are still some locations where the differences between the results in both stacks are outside the estimated 2σ uncertainty interval in referencing scenario 2, e.g. on the west- and east-coast. Averaged subsidence time series of (T)PSs in a radius of 500 m around six exemplary locations are displayed in Figure 6.9 for a detailed visualization of the results from both stacks. The overall trend of the time series agrees at most locations for both referencing scenarios, while the time series in referencing scenario 2 are characterized by considerably lower noise. Furthermore, the results from both stacks agree to a much higher degree in referencing scenario 2 compared to scenario 1. Location 6 is an exception, where the time series of descending and ascending stack do not agree in either of the referencing scenarios until the end of 2019. In referencing scenario 2, the differences in the first half of the time series are even higher than in scenario 1. Here, the differences have to be examined in more detail in the future, in order to attribute them to processing errors, noise or localized horizontal movements. At location 2, the noise in scenario 2 is still considerable, especially in the ascending stack, due to the large distance to reference areas. We assume that there is temporally correlated SCN at that location in both scenarios, leading to biased rate estimations in both stacks.

The estimated subsidence time series can be exploited to study the temporal evolution of the subsidence. The difference between the estimated subsidence rates in referencing scenario 2 between the periods October 2019 - April 2022 and April 2017 - October 2019 are displayed in Figure 6.10. The estimated standard deviations of the rate difference calculations are also plotted, which were calculated by propagating the rate estimation variances in both segments into the difference calculation. In both stacks, subsidence rate differences have an approximate mean of 0 with standard deviations of ~ 8.5 mm/yr, and there are locations where the differences agree well (for example Arrows 1 and 2 in Figure 6.10). However, they diverge in many parts of the delta, with differences being largely spatially correlated. For example, the results in the ascending stack indicate a large-scale decrease in subsidence at the most eastern part of the study area, while those in the descending stack indicate a slight increase in subsidence in large parts of the same area. The estimated standard deviations of the difference calculation are largest in that area, with values of up to 4.1 mm/yr and 9.4 mm/yr in the descending and ascending stack, respectively. However, the rate differences in the ascending stack are still outside the estimated 2-sigma uncertainty interval, indicating a significant decrease in subsidence rates over time. This is the same area which was already examined above, as it features differences in the estimated subsidence rates between both stacks for the whole time period of 2017-2022. We assume that temporally correlated noise is responsible for the differently estimated subsidence rate evolution. The results of referencing scenario 1 are displayed in the Appendix in Figure A.2. They are characterized by large spatial trends in ground range direction in both stacks.

In order to study the temporal evolution of the estimated subsidence in both stacks in more detail, the averaged subsidence time series of (T)PSs in a radius of 500 m around five locations are displayed in Figure 6.10 (e)-(n) for the two referencing scenarios. The time series comparison of the two referencing scenarios allows the same conclusions
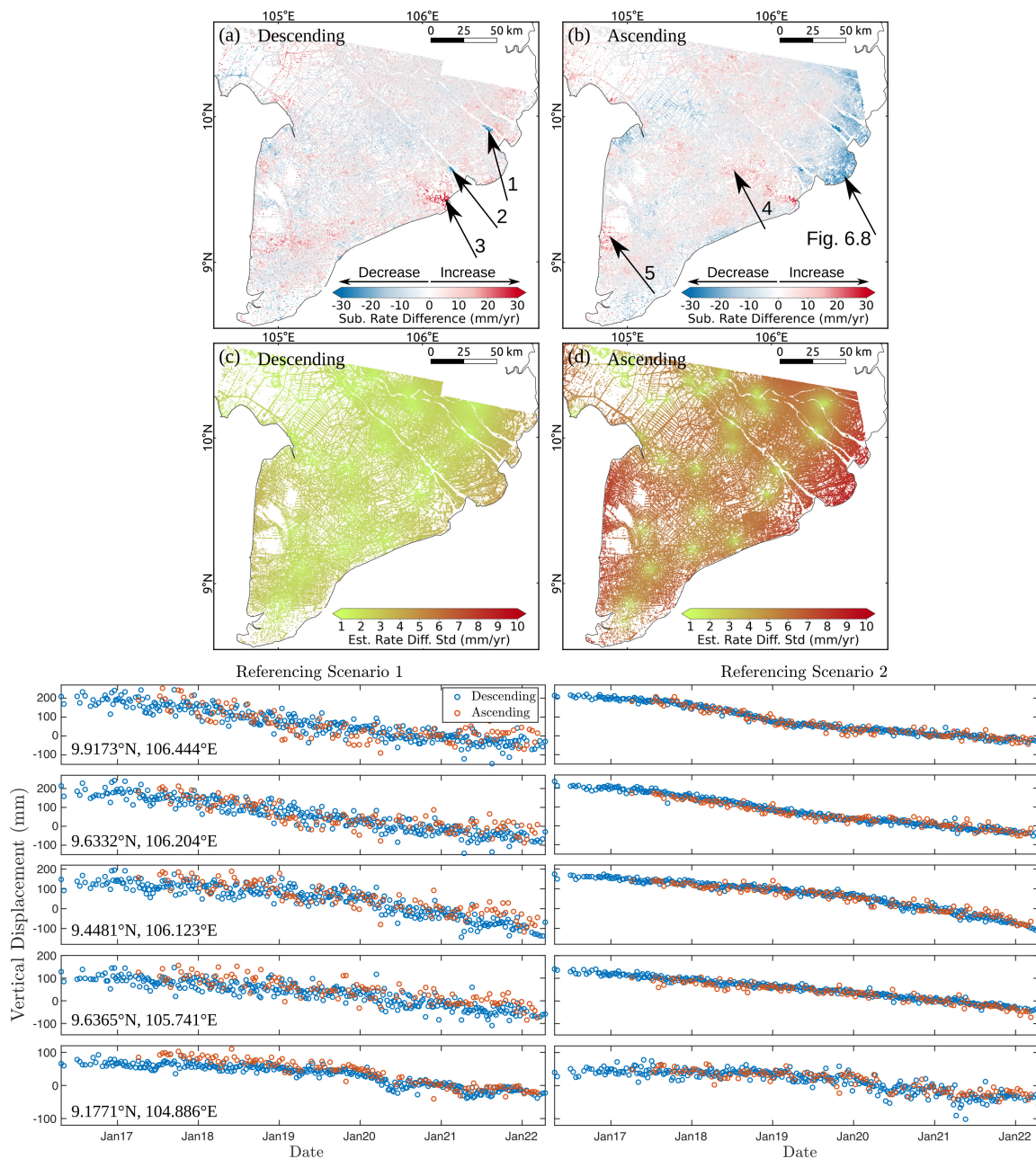
Figure 6.10.: (a)-(b) Difference in estimated subsidence rates between the periods Oct. 2019 to Apr. 2022 and Apr. 2017 to Oct. 2019 in the descending and ascending stack, respectively. (c)-(d) Estimated standard deviation of the rate difference calculation in (a)-(b). Only (T)PSs which cover the whole period of Apr. 2017 to Apr. 2022 are displayed in (a)-(d). Results in (a)-(d) are based on the referencing scenario 2. Below: Mean subsidence time series for all (T)PSs in a radius of 500 m around the five locations indicated by arrows in (a) and (b) in both referencing scenarios.

as the comparison of the time series in Figure 6.9. The time series of both stacks agree to a much higher degree with considerably lower noise level in the referencing scenario 2 than in scenario 1. Only at location five, the residual noise is higher for referencing scenario 2 than scenario 1, which is due to the proximity of the location to the island Hon Da Bac which was removed from the set of reference areas in scenario 2. The time series of both stacks, however, are characterized by different trends at that location in scenario 1, which is contrary to the results in scenario 2.

An interesting feature of the results is that the estimated subsidence time series at location 3 is characterized by apparent undulating movements with an approximate frequency of 1/yr in referencing scenario 1. These undulations are almost completely removed in referencing scenario 2, while the overall trend of the time series stays the same. There are two possible reasons for the observed differences. First, it could be possible that there are undulating vertical displacements originating in depths below the foundation depth of the reference bridges, caused by seasonal undulations of groundwater levels in the aquifers below. However, Duy et al. (2021) studied the groundwater dynamics across the VMD and found that significant seasonal variations of groundwater levels in coastal areas are mainly found in the Holocene and upper Pleistocene aquifers, which are expected to be located above the foundation depth of the bridges. We rather assume that the differences in both referencing scenarios are due to seasonally correlated residual SCN in the results of [... referencing scenario 1] at the eastern coast of the VMD, which is effectively reduced in [... referencing scenario 2].

Summing up, applying our proposed method to reduce SCN in the data with selected bridges as additional references leads to a significant alignment of the estimated subsidence rates and a significant reduction in their uncertainties. We assume that the differences in the estimated subsidence rates between the results in both stacks in referencing scenario 1 are due to temporally correlated SCN, which is largely suppressed by adding the bridges to the reference areas. As pointed out before, it has to be kept in mind that only subsidence originating from above the foundation depth of the selected bridges is measured this way. However, we see that the averaged differences between the estimated subsidence rates in the two referencing scenarios are small. The estimated subsidence rates in the descending stack are on average only 0.5 mm/yr higher in referencing scenario 1 than in referencing scenario 2, with a standard deviation of 1.3 mm/yr. The mean difference between both scenarios is 0.12 mm/yr in the ascending stack, with a standard deviation of 3.6 mm/yr. Consequently, there is no considerable change in the average subsidence rates when adding the bridges as reference areas, and we conclude that the largest part of the subsidence originates from depths above the foundation level of the selected bridges. The piled foundations of all bridges are assumed to be similar due to the similar length of the bridges and to go down to a maximum depth of 73 m (personal communication from Renck, A., 2021).

Table 6.4.: Measured subsidence rates in the upper 100 m at two subsidence monitoring stations between February 2017 and July 2019 (Karlsrud et al., 2020) and mean estimated subsidence rates of all (T)PSs, which were active in the given time period, in a radius of 200 m around the stations in the two referencing scenarios.

	Station 1	Station 2
Coordinates	8.89 ° N, 104.86 ° E	8.09 ° N, 105.0 ° E
Karlsrud et al. (2020) (mm/yr)	4	24
Desc (1) (mm/yr)	6.4	27.5
Desc (2) (mm/yr)	4.5	25.5

6.5.2. Comparison with Alternative Measurements

There have been various subsidence observations made in the VMD, which were conducted with different measurement techniques and partly observed subsidence in different subsurface depths. Minderhoud et al. (2020) give an overview of the existing observations. Two of the accessible subsidence observations are suitable to be compared with our subsidence estimates since they describe subsidence in approximately the same subsurface depths and share a temporal overlap with our observations. These include measurements from subsidence monitoring stations on the Ca Mau peninsula (Karlsrud et al., 2020) and the PSI observations from the company GISAT in the scope of the Copernicus Emergency Service (Copernicus, 2019). These observations are compared to the results from M-SBAS-2-StaMPS in the following. At the end of the section, latter results are also compared with results obtained with the StaMPS algorithm in a representative part of the VMD.

Comparison with Subsidence Monitoring Stations

Karlsrud et al. (2020) presented measurements from three subsidence monitoring stations on the Ca Mau peninsula which were founded at 100 m depth, thus were only able to measure subsidence in the upper 100 m of the subsurface. For the three stations, which are approximately located at 8.89 ° N, 104.86 ° E, 8.09 ° N, 105.0 ° E and 9.177 ° N, 105.10 ° E, subsidence rates of 4, 24 and 31 mm/yr were measured between February 2017 and July 2019. Since there are inconsistencies in their publication between the specified subsidence rate and plotted subsidence time series at station 3, we excluded that station from the comparison. We compared the rates with the median subsidence rate of all (T)PSs in the given time period which were identified in a radius of 200 m around the stations. We solely considered the results from the descending stack, since only this stack completely covers the given time period. The results are shown in Table 6.4. Our estimated subsidence rates at location 1 are 6.4 and 4.5 mm/yr for the two referencing scenarios with estimated standard deviations of the rate estimate of 2.5 and 1.6 mm/yr, respectively. At location two, our estimated rates are 27.5 and 25.5 mm/yr with estimated standard deviations of 3 and 0.9 mm/yr. Consequently, our results agree with those from the subsidence monitoring stations, with deviations of 2.4 and 0.5 mm/yr at station 1 and 3.5 and 1.5 mm/yr at station 2

for both referencing scenarios, respectively. The fact that the results from referencing scenario 2 better fit their observations is expected to be related to two factors. First, both observations only measured subsidence in the upper subsurface, while the results in referencing scenario 1 provide an estimate of the total subsidence. In case that part of the subsidence originates from depth below the foundation depth of the bridges and the subsidence monitoring stations, it is only measured in our results from referencing scenario 1. The second factor is the reduced temporally correlated noise in scenario 2 compared to scenario 1.

Comparison with PSI-Measurements by Copernicus Emergency Service

The company GISAT studied land subsidence in the VMD using Sentinel-1 data acquired in descending orbit between November 2014 and January 2019. The study was initiated by an activation of the Copernicus Emergency Management Service and the processing and the results were described in Copernicus (2019) and Minderhoud et al. (2020). The PSI processing was carried out with the SARPROZ software (Perissin et al., 2011). A spatial low-pass filter was applied in order to estimate spatially correlated signals in interferograms after the subtraction of estimated linear displacement rates. The estimated LOS displacements were converted into vertical displacements, and spatial trends in the estimated velocity field were estimated and subtracted. No detailed information of the low-pass filter and final detrending operation was given. The processing was realized in spatial patches which were merged later, and the displacements were referenced to the available solid rock outcrops, as done in our referencing scenario 1.

They identified 668710 PSs across the VMD in the study area shown in Figure 6.1 (d). They compared their results with unpublished results from data acquired in ascending orbit over parts of the VMD. The estimated subsidence rates diverged by 7.07 mm/yr on average, which is significantly larger than the differences between our results from descending and ascending orbits. We compared our results from the descending orbit in referencing scenario 2 with their results in the overlapping time period of April 2016 to January 2019. For this purpose, we extracted their estimated subsidence time series in the given time period and estimated subsidence rates. The same was carried out for all (T)PSs in our results which were active in the overlapping time period. The estimated rates from both approaches were spatially gridded by calculating the median of estimated rates of observation points inside grid cells of $500 \, \text{m} \times 500 \, \text{m}$.

The differences between the gridded subsidence rates of the GISAT analysis and our approach are displayed in Figure 6.11. The differences are characterized by a mean of $2.14 \, \text{mm/yr}$ and a standard deviation of $4.9 \, \text{mm/yr}$, indicating slightly larger subsidence rates in the results by GISAT, on average. The differences are mainly spatially correlated, and larger differences are primarily situated at the margin of the study area, where uncertainties in both results are largest. An exemplary patch of differences of more than $10 \, \text{mm/yr}$ is located on the southern Ca Mau peninsula. The patch features slight discontinuities to adjacent areas, which correspond to specific range and azimuth lines in the SAR geometry. As this patch is also characterized
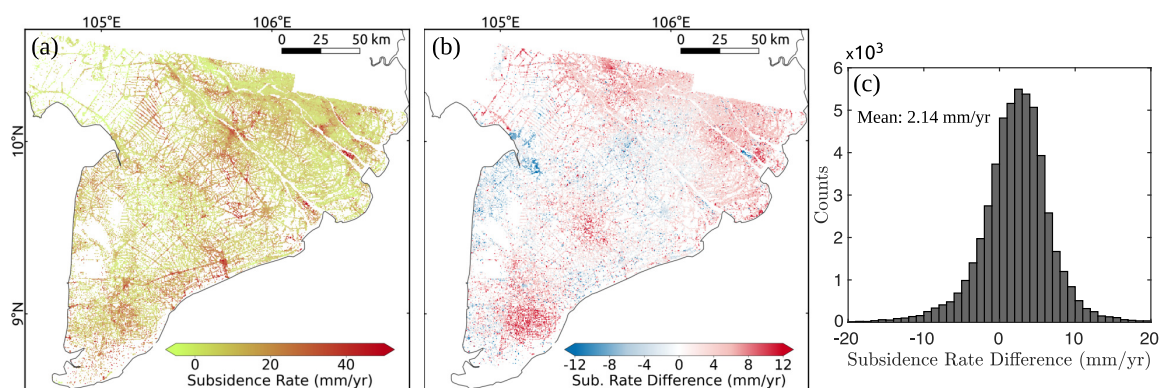
Figure 6.11.: (a) Subsidence Rates estimated with our approach for the time series between April 2016 and January 2019 based on data from the descending orbit and the referencing scenario 2. The rates were spatially gridded by calculating the median of estimated rates of observation points inside grid cells of $500\,\mathrm{m} \times 500\,\mathrm{m}$. (b) Difference between gridded subsidence rates from the analysis by GISAT and our analysis. (c) Histogram of differences.

by discontinuities to neighboring areas in the estimated height error in the GISAT analysis, we assume that there are slight spatial inconsistencies in their results which originate in the PSIs patch processing and subsequent merging.

Summing up, the comparison showed a substantial consistency between our results and those from the company GISAT. Differences between gridded subsidence rates are spatially correlated in large parts. They are most considerable at the margins of the study area, which might be caused by the large distances to the outcrops, which were used as reference in the analysis by GISAT. We assume that the differences in a patch in the southern peninsula are processing artifacts in the analysis by GISAT. An advantage of our results is that no filtering and detrending was performed, which is contrary to the GISAT analysis. In the latter, displacement signals of interest might have been filtered out and the spatial detrending prevents the analysis of large-scale displacement phenomena.

Comparison with Results from StaMPS

Finally, we compared our results with results achieved with the StaMPS software. Due to computational reasons, the comparison was only realized in a representative patch of the study area with a size of about $30\,\mathrm{km} \times 30\,\mathrm{km}$ centered around the city of Can Tho (Figure 6.12). Furthermore, we compared only results from the descending data stack between April 2016 and April 2022. The phase noise estimation and identification of PSs was carried out with default parameters. For the subsequent unwrapping, we tested different parameter settings and here present results with an unwrapping grid size of $100\,\mathrm{m}$. The grid size is 5 times smaller compared to the unwrapping grid size we used in our approach, resulting in considerably higher computational cost of the unwrapping. The results were supposed to be referenced to the selected reference
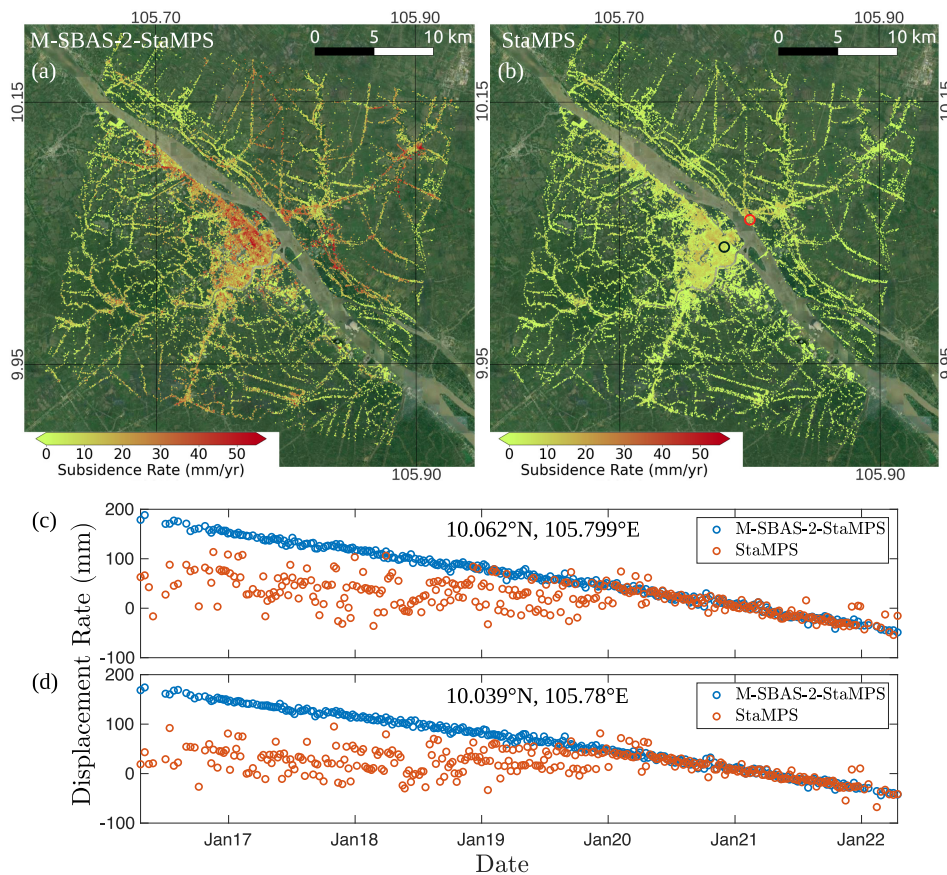
Figure 6.12.: (a)-(b) Estimated subsidence rates using M-SBAS-2-StaMPS and StaMPS, respectively, around the city of Can Tho, based on data from the descending orbit between April 2016 and April 2022. (c)-(d) Mean estimated subsidence time series of all (T)PSs in a radius of 100 m around the locations in the red and black circles in (b), respectively. Imagery data: Google Earth, © 2023 Maxar Technologies.

bridges in the study area. However, a building which was identified as stable in our results was finally used as reference in this comparison, as the identified PSs on the reference bridges were affected by large unwrapping errors in the StaMPS analysis.

The StaMPS approach identified 228 738 PSs in the study area, while our approach identified 665 925 observations points which comprise 116 574 PSs and 549 351 TPSs. The ratio of identified TPSs to PSs in our approach for the time series length of six years meets the findings in Section 5.5. Considering the similar ratios of identified PSs and AmPSs in a time series of six years length in Section 5.5, we assume that the number of identified PSs would be the similar in both analyses without the integration of TPSs.

The estimated subsidence rates in both analyses are displayed in Figure 6.12. Solely the rates of PSs are shown for our analyses for the sake of temporal consistency in the displayed results. It is striking that the estimated subsidence rates are much higher in our results than in the results derived from the StaMPS analysis. The

estimated subsidence rates in our analysis are on average 10.68 mm/yr higher than those in the StaMPS analysis. This is caused by severe unwrapping errors in the latter, as shown in two exemplary subsidence time series in Figure 6.12 (c)-(d). It can be observed that the subsidence time series agree well around the master acquisition on February, 1st 2021. However, the differences increase with increasing temporal distance to the master. The time series from the StaMPS analysis are characterized by unwrapping errors, shifted by a multiple of $\lambda/2$ from the time series in our results. The results meet the findings of the M-SBAS and StaMPS comparison in Schenk (2015), which was shortly described in Section 3.2. The StaMPS algorithm bases on the assumption of spatial correlation in the displacement field. The advantage of this is that no deformation model has to be assumed during the PSI processing. No displacements of single PSs are estimated and subtracted prior to the unwrapping. This leads to problems for the phase unwrapping when small-scale variations in the displacement field prevail, as in the example in the city of Can Tho. The phases due to varying displacements on short spatial distances increasingly diverge with increasing temporal baselines, leading to large phase differences on short spatial scales which are difficult to unwrap. The M-SBAS algorithm, on the other hand, estimates displacement rates of all (T)PSs and reduces the phases due to these displacements prior to the unwrapping. This leads to smooth interferograms which can be robustly unwrapped. The unwrapping grid size can be chosen much larger in that case, since phase variations inside the grids are greatly reduced.

Concluding, the PS identification shows similar performance in both approaches, whereas the TPS integration obviously leads to a considerable increase in identified observation points. The StaMPS algorithm is characterized by an incapability to properly unwrap interferometric phases due to small scale variations in the displacement field, while the unwrapping results in our approach do not feature unwrapping errors. This result could be expected based on the different applications which the approaches were designed for. The StaMPS algorithm was designed to study spatially correlated displacement phenomena, while the M-SBAS was designed to study displacement fields which are potentially characterized by large small-scale variations. This is why the latter is much better suited to study subsidence in the VMD. Another advantage of the M-SBAS algorithm is the faster parameter estimation in the phase noise estimation step of PSCs. The PS identification in M-SBAS including parameter estimation only took 23 % of the processing time in StaMPS in the study by Schenk (2015). It has to be noted that the StaMPS results could probably be improved by choosing a small-baseline interferogram network to be analyzed and unwrapped, which is actually intended for the inclusion of DSs in the algorithm (Hooper, 2008).

6.5.3. Systematic Analysis of Initial Subsidence of New Buildings

The integration of TPSs into PSI not only leads to a flexible PSI monitoring system which analyzes point scatterers in their coherent lifetime segments, but leads to additional information in the form of change dates of TPSs. This information can be

used for land surface change detection, as done in Yang et al. (2017). We here present a special use case of the TPS integration which is based on clustering appearing TPSs based on their location, estimated subsidence rate and appearing date in order to identify newly built constructions. Their initial subsidence time series is systematically analyzed with the goal to assess potential load-induced settlement and its contribution to the measured total subsidence in the VMD. The study was initially published in Dörr et al. (2022c). The updated analysis with the final results of this thesis is described in the following. The analysis is solely based on the results in the descending stack due to the longer time series and lower noise level compared to the ascending stack.

We used Density-Based Spatial Clustering of Applications with Noise (DBSCAN) (Ester et al., 1996) to cluster appearing TPSs based on their location including their estimated residual height above the used reference DEM, appearing date and estimated subsidence rate. A minimum number of 3 points within a cluster was demanded. The data matrix was whitened prior to the clustering operation and the weights of the single parameters for the clustering were slightly adjusted in order to optimize the clustering results, according to personal observations. For example, the weight of the estimated height of the points was reduced due to its limited estimation accuracy (see Section 6.2).

An example of clustered appearing TPSs is displayed in Figure 6.13, which covers an area at the eastern border of the city of Can Tho. Several industrial buildings were constructed in that area during the covered time series. The identified observation points are shown in Figure 6.13 (c), which mainly consist of appearing and visiting TPSs. It is assumed that most identified visiting TPSs were interrupted by ongoing construction activities and will probably re-appear as recurring TPSs in the future. Identified clusters of appearing TPSs are shown in Figure 6.13 (d). The different clusters are mainly distributed on new constructions, partly also on newly sealed land surface areas. Few buildings triggered various clusters, which is caused by different parts of the particular buildings being affected by differing displacements, as also observed in a PSI study by Schneider and Soergel (2021), for example. The large red cluster in the center of the area covers three adjacent buildings which look alike, were built at the same time and probably share a similar construction. In Figures 6.13 (e)-(g), the subsidence time series of three exemplary clusters are displayed, which are located on the three western buildings in the covered area. It is striking that two of the three clusters are characterized by a strong initial settlement of about 30 mm/yr, which decreases considerably after approximately 1.5 years at one of them and one year at the other. It is assumed that this is caused by load-induced settlement of shallow soil layers. On the contrary, the third house is subsiding at a nearly linear rate of about 30 mm/yr, which is only slightly decreasing over the covered time period. Either there is not a significant contribution of load-induced settlement to the total subsidence at this building, or it takes longer for the shallow soil layers to be fully consolidated at this place, so that the decrease in initial settlement only set in after the end of the time series. Differences in the initial displacement time series of new
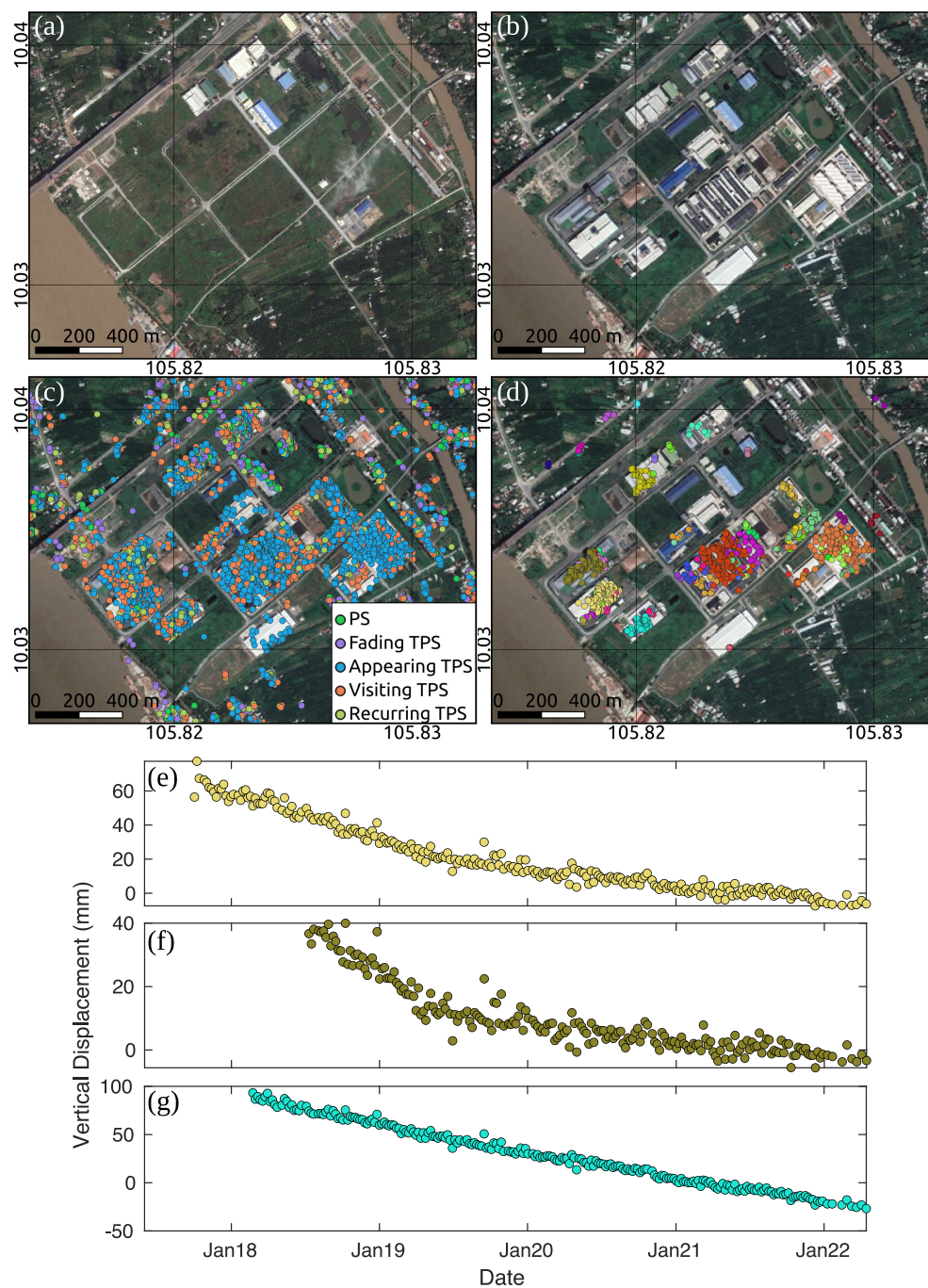
Figure 6.13.: (a)-(b) Satellite images over part of Can Tho city in 2017 (a) and 2021 (b) (Google Earth, © 2023 Maxar Technologies). (c) Location and scatterer type of identified (T)PS pixels. (d) Clusters of appearing and visiting TPS pixels, identified using DBSCAN clustering based on the location, appearing date, height and mean subsidence rate of the pixels. Points displayed in a common color belong to the same cluster. (e)-(g) Mean vertical displacement time series of three clusters with respect to the selected master scene on February 2nd, 2021. The colors identify the location of the clusters in subfigure (d).
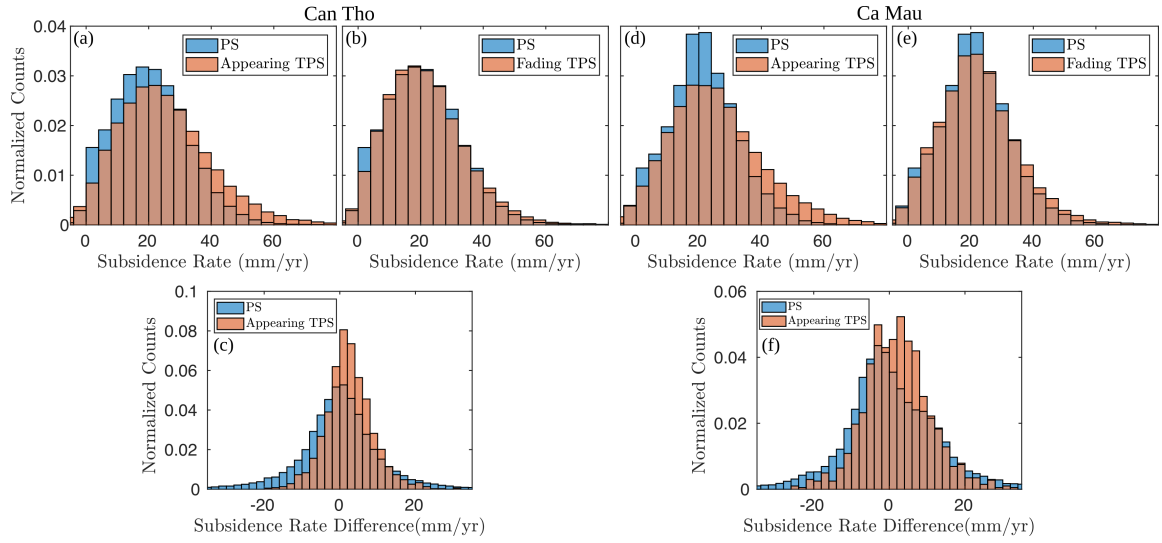
Figure 6.14.: Subsidence statistics in Can Tho (a)-(c) and Ca Mau (d)-(f). (a)/(d) Histograms of the subsidence rate of PSs and subsidence rate of appearing TPSs in their first year. (b)/(f) Histograms of the subsidence rate of PSs and fading TPSs. (c)/(f) Histogram of differences in first and second year subsidence rate of appearing TPS clusters and differences in subsidence rates of PSs in 2017 and 2018.

buildings might be due to differences in the type of constructions, foundation depths, local geology and land use/land cover history.

We systematically studied initial settlements of appearing TPSs in the cities of Can Tho and Ca Mau. We only studied appearing TPSs with a lifetime of more than two years. The histogram of estimated subsidence rates of PSs and those of TPSs in the first year after their appearance are shown in Figure 6.14. A higher portion of appearing TPSs exhibits high subsidence rates compared to PSs in both cities. In Can Tho, 15 % and 9 % of the appearing TPSs are subsiding at a rate of more than 40 mm/yr in the first year after appearance and in their total lifetime, respectively. On the contrary, only 6 % of the PSs are subsiding at a rate of more than 40 mm/yr. The particular percentages are 16 %, 10 % and 5 % in Ca Mau, respectively. The results show that a portion of appearing TPSs in both cities is subsiding at an exceptional high initial subsidence rate after appearance, which is decreasing over time, as found for scatterers on two buildings in the example in Figure 6.13. We attribute this signal to load-induced initial settlement of new constructions. In order to test a systematic bias in the subsidence rate estimation of TPSs, we also compared the estimated subsidence rates of fading TPSs and PSs in Figure 6.14. No significant differences are visible between the subsidence rates of both scatterer groups in both cities, i.e. a systematic bias in the subsidence rate estimation of TPSs can be ruled out.

In order to study the temporal evolution of the subsidence of new buildings in more detail, the estimated subsidence rates of clusters of appearing TPSs were calculated in the first year and second year after their appearance. The clusters are expected to represent new constructions or built-up areas. The mean subsidence time series

in both cities was removed in order to reduce temporal changes in the large-scale subsidence field in the cities. The results for both cities are presented in Figure 6.14 (c)/(f). Appearing TPS clusters have a slight tendency of decreasing subsidence rates between the first and second year after their appearance. The mean difference in subsidence rates is 2.5 mm/yr and 2.1 mm/yr in Can Tho and Ca Mau, respectively. We also compared the subsidence rates of PSs for the exemplary years 2017 and 2018. The histograms of the subsidence rate differences are plotted in Figure 6.14 (c)/(f). The mean subsidence rate differences are -0.1 mm/yr and 0.4 mm/yr.

Summing up, the TPS integration into PSI not only leads to a flexible monitoring system which is able to handle dynamic land surface changes during the time series, but provides additional information in form of change dates of identified TPSs, which can be used to carry out change detection. We here identified new buildings by clustering appearing TPSs based on their location, appearing date, height and displacement rate and systematically studied their initial displacement. We found that the portion of appearing TPSs with high initial subsidence rates is larger than the portion of PSs and fading TPSs with high subsidence rates in the cities of Ca Mau and Can Tho. New buildings are on average characterized by a slightly decreasing subsidence rate in the first two years after appearing. We attribute part of their measured subsidence to loading-induced initial settlement of the shallow (sub)surface and expect settlement of this kind to contribute noticeably to the measured total subsidence across the VMD, especially due to the recent high building activity (Minderhoud et al., 2018).

6.6. Conclusion

In this chapter, the proposed M-SBAS-2-StaMPS approach was applied to subsidence monitoring in the VMD. Sentinel-1 data acquired in descending orbit between April 2016 and April 2022 and in ascending orbit between April 2017 and April 2022 were evaluated for this purpose. Both stacks are affected by high residual noise after the subtraction of modelled phase disturbances, which is probably mainly tropospheric noise caused by the insufficient performance of the tropospheric delay modelling, due to the low latitude location of the study area and direct connection to the sea. The ascending data stack is characterized by an even higher noise level than the descending data stack, which we assume is caused by larger atmospheric noise due to its acquisition time at dusk, compared to the acquisition of the descending stack at dawn.

The algorithm identified a high density of observation points across the study area. Considerably more TPSs than PSs were identified in both stacks. The ratios of identified TPSs to PSs confirm the findings in Section 5.5 in the descending stack. The ratios are different in the ascending stack, which is mainly caused by the much lower number of acquisitions in this stack compared to the descending stack. The share of appearing TPSs in the total number of TPSs is highest among all TPS types in both stacks, which we assume to be a result of the high construction activity in the VMD. The results confirm the applicability of the proposed TPS integration method

in Chapter 5 in large scale problems, which provides a significant densification of the observation point networks.

The estimation of residual SCN with the proposed method in Section 4.5 was realized in two different referencing scenarios. In the first scenario, only solid rock outcrops were selected as presumably stable reference areas. They are mainly located in the north-western part of the study area, leading to an insufficient spatial distribution for a reasonable SCN estimation all across the study area. This is why large bridges with deep foundations were selected as additional reference areas in referencing scenario 2, which are well distributed across the study area. It must be pointed out that only subsidence originating from above the foundation depth of the selected bridges can be measured this way. The results from both data stacks and both referencing scenarios were compared in detail.

The results feature subsidence rates which are up to 6 cm/yr in urban areas and are characterized by high spatial variability on short and large spatial scales, which is probably due to numerous reasons, including different foundation depths of constructions. We found that the proposed method to reduce residual SCN significantly improves the results in referencing scenario 2, demonstrating that the method robustly removes SCN in case that the reference network is characterized by a proper spatial distribution. This has been noted in that the estimated rates in both stacks as well as exemplary subsidence time series agree to a much higher degree in referencing scenario 2 than in scenario The estimated mean standard deviations of the subsidence estimates are decreased from 28.1 mm and 35.6 mm to 10.9 mm and 17.5 mm in the descending and ascending stack, respectively. As a consequence, the estimated mean standard deviations of the rate estimates are approximately halved to 0.5 mm/yr and 1.2 mm/yr. Still, there are differences in the estimated subsidence time series between the descending and ascending stack, which are outside the estimated 2σ uncertainty interval and have to be studied in more detail in the future. We assume that the standard deviation of the subsidence rate estimation might be underestimated at locations with large distances to reference areas due to residual temporally correlated SCN in the subsidence time series. This was noted in the comparison of subsidence rate differences between both stacks in both referencing scenarios. The differences are characterized by a large spatial trend in scenario 1, which is removed in scenario 2. As we do not expect horizontal displacements of this spatial scale after the reduction of plate motions, we attribute this observation to temporal correlations in the residual SCN in referencing scenario 1, which are largely removed in scenario 2. A robust approach to estimate the temporal covariance of the residual SCN should be developed in the future in order to enable its integration into the stochastic model.

The averaged differences between the estimated rates in both referencing scenarios are small, resulting in the conclusion that most of the subsidence indeed originates in depths above the foundation of the bridges, which we expect to be about 70 m deep. The validation of the estimated subsidence rates is difficult as a consequence of a sparsity of ground truth measurements. However, the independent results from the descending and ascending stack agree well in referencing scenario 2. Furthermore, the

estimated subsidence rates were compared with sparse alternative measurements. They agree with subsidence rate measurements at two subsidence monitoring stations on the Ca Mau peninsula, which were presented in Karlsrud et al. (2020). They also agree well on short spatial scales with PSI results by the company GISAT, with averaged differences of 2.14 mm/yr and a standard deviation of 4.9 mm/yr. Larger magnitude differences in the comparison are mainly spatially correlated and might be due to diverging temporally correlated SCN in both results. The results by GISAT were filtered and detrended with unknown processing parameters, leading to the fact that displacement differences at large distances exhibit a high uncertainty. Our proposed PSI approach does not rely on spatio-temporal filters and detrending operations. For a last comparison, the StaMPS algorithm was applied to a representative spatial patch around the city of Can Tho. It turned out that the standard StaMPS approach for PS processing is not suitable to study subsidence in the VMD in the long-term due to the large subsidence rate variations on short spatial scales. The estimated subsidence time series exhibit large unwrapping errors for interferograms with medium to long temporal baselines, which is contrary to our results.

At the end of the chapter, a special use case of the TPS integration was presented. The TPS integration not only leads to a significant increase in identified observation points, but provides additional information in the form of the change dates of TPSs which can be exploited to do change detection. New constructions were identified by clustering appearing TPSs and it was found that a higher portion of them is subsiding at an exceptional high rate in the first year after their appearing, compared to PSs and fading TPSs. Furthermore, their subsidence rate was on average decreasing within the first two years after appearance. We attribute these findings to loading-induced initial settlement of buildings, which contributes to the measured total subsidence.

7. Conclusion and Outlook

PSI has developed into an operational technology in certain applications to monitor displacements on the Earth's surface from space. However, long-term and large-scale displacement monitoring with PSI still represent challenging applications. In this thesis, an extended PSI approach was presented which is able to robustly and flexibly handle these challenges. The approach is based on the M-SBAS approach described in Schenk (2015). The essential extensions of the approach are listed in the following.

- **Integration into Large-Scale PSI**
  The M-SBAS algorithm was originally designed to robustly and efficiently monitor heterogeneous displacements in small-scale urban study areas. The approach did not include phase unwrapping. Various modifications were developed to extend the approach to a full PSI approach which includes unwrapping and robustly handles large-scale displacement monitoring. The approach is referred to as M-SBAS-2-StaMPS, since the results are imported into StaMPS to make use of its unwrapping algorithm. Great focus was put on the reduction of phase noise contributions which are especially relevant for large-scale displacement monitoring. This includes in a first step the modelling of the tropospheric delay, tidally induced displacements and plate motion. Additionally, a covariance-based reference integration method was presented to reduce residual SCN in interferograms. Reference pixels with known displacement time series could be located around permanent GNSS stations or located in areas which are stable during the considered time series, for example. The SCN is sampled at these pixels and interpolated on all other pixels, making use of error cokriging which takes the estimated covariance of the sampled SCN into account. The method showed superior performance in the reduction of residual SCN in a simulation and a real data study, compared to other methods which are based on reducing SCN on basis of reference pixels.

- **Fully Integrated Temporary Persistent Scatterer Interferometry**
  Physical changes of the land surface and changes in the acquisition geometry can cause PSs to fade or appear in periods of the SAR time series. The number of continuously coherent PSs decreases with increasing time series, while the number of such TPSs increases. Standard PSI approaches are not able to identify and analyze TPSs. A method to fully integrate TPSs into M-SBAS-2-StaMPS was presented in order to establish a flexible PSI system which handles dynamic land surface changes during the analyzed time series, thus provides the best possible PSI-based geodetic observation network for long-term monitoring. The detection of TPSs and an initial estimation of their change dates is realized

with the amplitude-based approach by Hu et al. (2019). The initially estimated change dates are iteratively refined during the phase noise estimation process, using a newly developed phase-based change detection method. The phases of identified PSs and TPSs are jointly unwrapped in a modified version of the unwrapping algorithm in StaMPS. No previous TPS approach included phase unwrapping to our knowledge. At the end, the temporal datum of those TPSs is re-defined, whose coherent lifetime does not cover the master scene.

Experimental results based on Sentinel-1 data acquired over the Vietnamese city of Ca Mau showed that the change date refinement significantly increases the average coherence and number of identified TPSs. The relevance of the TPS integration for PSI-based observation networks as a function of the considered SAR time series length was analyzed in another small-scale study. It could be shown that the TPS integration leads to an increasingly significant improvement of the observation network with increasing time series length both in urban and rural areas in the VMD.

The proposed algorithm was finally applied to subsidence monitoring in the VMD, based on Sentinel-1 data acquired between 2016 and 2022 in descending and ascending orbits. The algorithm identified a high density of observation points across the study area. The number of identified TPSs exceeded the number of identified PSs in both stacks, indicating a highly significant contribution of the TPS integration to the observations, as found before in the small-scale studies. The results confirm that the proposed method shows high performance in large-scale problems. The estimation of residual SCN was realized in two different referencing scenarios, one of which included only solid rock outcrops as reference areas. In the second, large bridges with deep foundations were selected as additional reference areas to achieve a proper spatial distribution of reference areas across the study area. We found that the proposed method to reduce residual SCN significantly improved the results in referencing scenario 2, demonstrating that the method robustly removes SCN in case that the reference network is characterized by a proper spatial distribution. The inclusion of the bridges as reference areas in scenario 2 led to a decrease of the estimated mean standard deviations of the subsidence estimates from 28.1 mm and 35.6 mm to 10.9 mm and 17.5 mm in the descending and ascending stack, respectively. As a consequence, the estimated mean standard deviations of the rate estimates were approximately halved to 0.5 mm/yr and 1.2 mm/yr. The method does not rely on filtering and detrending operations.

The validation of the estimated subsidence rates is difficult due to sparse ground truth. However, the results from both orbits showed good agreement in referencing scenario 2. Furthermore, the results showed good agreement with measurements at two subsidence monitoring stations and an alternative PSI analysis which was carried out in the scope of the Copernicus Emergency Service. A last comparison demonstrated a superior performance of our approach compared to the StaMPS algorithm for subsidence monitoring in the VMD, because the estimated subsidence time series by StaMPS feature a lot of unwrapping errors, which is contrary to our results.

Lastly, a special use case of the TPS integration was presented. The TPS integration not only leads to a significant increase in identified observation points, but provides additional information in the form of the change dates of TPSs which can be exploited for the purpose of change detection. It was exemplarily demonstrated that new constructions can be identified by clustering appearing TPSs, whose initial displacement time series can be systematically analyzed afterwards. In the case of the VMD, this method was used to find that load-induced initial settlement of new constructions contributes to the measured total subsidence.

The estimated subsidence rates in the VMD are highly heterogeneous on short and large spatial scales, and highest rates of up to 6 cm/yr are mainly found in urban areas. It could be demonstrated that the largest part of the subsidence originates from shallow subsurface depths of less than approximately 70 m. As a result, subsidence heterogeneity on short spatial scales are largely induced by varying foundation depths of infrastructure. It must be noted that the results of the subsidence monitoring in the VMD were mainly examined with regard to the evaluation of the proposed method. It is desirable that the achieved results are geologically evaluated in detail by experts on land subsidence. This way, the results could contribute to the understanding of causes of land subsidence in the VMD.

The proposed approach offers potential for improvements, which should be considered in future developments:

- **Estimation of Ionospheric Noise**
  Ionospheric effects can lead to significant noise in large-scale InSAR studies which base on C-band or longer-wavelength SAR data (Liang et al., 2019). This noise is not estimated and subtracted in our approach, but treated as residual noise, which is estimated and subtracted in the proposed reference integration method. As the latter method depends on a proper spatial distribution of reference areas across the study area, all estimable phase contributions should be estimated and removed a-priori. Methods to account for the ionosphere are the range split-spectrum method (Rosen et al., 2010; Gomba et al., 2016) and modelling based on TEC maps (Eineder et al., 2011; Yunjun et al., 2022). One of these should be implemented in M-SBAS-2-StaMPS in the future.

- **Spatial Statistics of Residual SCN**
  A fundamental step of the reference integration method to reduce SCN in interferograms is the estimation of the spatial covariance of the residual SCN. This is achieved by averaging isotropic variograms in interferograms with small temporal baselines. However, Knospe and Jónsson (2010) showed that the atmospheric noise in InSAR is often anisotropic. Following their study, it should be tested in various study areas whether the covariance description of the residual SCN by means of anisotropic variogram models could further improve the SCN estimation method.

- **Uncertainty of Estimated Displacement Rates**
  Temporally correlated signals can persist in the residual noise, even after the

subtraction of modelled phase disturbances and the reference integration method to estimate and remove residual SCN. They are not considered in the stochastic model of the rate estimation in M-SBAS-2-StaMPS, potentially leading to biased rate estimations and underestimated rate uncertainties. Robust methods should be developed to model the spatio-temporal covariance of the residual SCN and consider it in the PSI approach.

- **TPS Visualization**
  The TPS integration leads to a flexible PSI system which analyzes point scatterers in their coherent lifetimes. Estimated displacement rates are only valid in the differing lifetime of the scatterers, leading to potential inconsistencies in joint visualizations of displacement rates. Suitable visualization approaches should be developed which consider the lifetime of each scatterer in the visualizations, in order to avoid misinterpretations. Examples of such approaches could be time-laps movies which only display the displacement rate of TPSs during their particular lifetimes. Another aspect to consider for visualizations is that the variance of displacement rate estimation depends on the number of acquisitions in the particular lifetime of each TPS.

Bibliography

Abidin, H. Z., H. Andreas, I. Gumilar, and I. R. Wibowo (2015). "On correlation between urban development, land subsidence and flooding phenomena in Jakarta". In: *IAHS-AISH Proceedings and Reports* 370, pp. 15–20.

Adam, N. (2022). "Empirical Bayesian Estimation of the Interferometric SAR Coherence Magnitude". In: *IEEE Journal of Selected Topics in Applied Earth Observations and Remote Sensing* 15, pp. 6306–6323.

Adam, N., B. Kampes, and M. Eineder (2005). "Development of a scientific permanent scatterer system: Modifications for mixed ERS/ENVISAT time series". In: *European Space Agency, (Special Publication) ESA SP*. 572. Salzburg, pp. 457–465.

Adam, N., B. Kampes, M. Eineder, J. Worawattanamateekul, and M. Kircher (2003). "The development of a scientific permanent scatterer system". In: *ISPRS Workshop High Resolution Mapping from Space*. Hannover, Germany, pp. 119–123.

Agnew, D. C. (2012). "SPOTL : Some Programs for Ocean-Tide Loading". In: *SIO Technical Report* 1.June 1996, p. 28.

Aguiar, P., A. Cunha, M. Bakon, A. M. Ruiz-Armenteros, and J. J. Sousa (2022). "PS-InSAR Target Classification Using Deep Learning". In: *International Geoscience and Remote Sensing Symposium (IGARSS)* 2022-July.1, pp. 2931–2934.

Alshawaf, F., B. Fersch, S. Hinz, H. Kunstmann, M. Mayer, and F. J. Meyer (2015). "Water vapor mapping by fusing InSAR and GNSS remote sensing data and atmospheric simulations". In: *Hydrology and Earth System Sciences* 19.12, pp. 4747–4764.

Altamimi, Z., L. Métivier, P. Rebischung, H. Rouby, and X. Collilieux (2017). "ITRF2014 plate motion model". In: *Geophysical Journal International* 209.3, pp. 1906–1912.

Anastassopoulos, V., G. A. Lampropoulos, A. Drosopoulos, and M. Key (1999). "High resolution radar clutter statistics". In: *IEEE Transactions on Aerospace and Electronic Systems* 35.1, pp. 43–60.

Ansari, H., N. Adam, and R. Brcic (2014). "Amplitude time series analysis in detection of persistent and temporal coherent scatterers". In: *International Geoscience and Remote Sensing Symposium (IGARSS)* 1, pp. 2213–2216.

Ansari, H., F. De Zan, and R. Bamler (2018). "Efficient Phase Estimation for Interferogram Stacks". In: *IEEE Transactions on Geoscience and Remote Sensing* 56.7, pp. 4109–4125.

Anthony, E. J., G. Brunier, M. Besset, M. Goichot, P. Dussouillez, and V. L. Nguyen (2015). "Linking rapid erosion of the Mekong River delta to human activities". In: *Scientific Reports* 5, pp. 1–12.

Aobpaet, A., M. C. Cuenca, A. Hooper, and I. Trisirisatayawong (2013). "InSAR time-series analysis of land subsidence in Bangkok, Thailand". In: *International Journal of Remote Sensing* 34.8, pp. 2969–2982.

Arciniegas, G. A., W. Bijker, N. Kerle, and V. A. Tolpekin (2007). "Coherence- and amplitude-based analysis of seismogenic damage in Bam, Iran, using ENVISAT ASAR data". In: *IEEE Transactions on Geoscience and Remote Sensing* 45.6, pp. 1571–1581.

Argus, D. F., R. G. Gordon, and C. Demets (2011). "Geologically current motion of 56 plates relative to the no-net-rotation reference frame". In: *Geochemistry, Geophysics, Geosystems* 12.11, pp. 1–13.

Argus, D. F., M. B. Heflin, G. Peltzer, F. Crampé, and F. H. Webb (2005). "Interseismic strain accumulation and anthropogenic motion in metropolitan Los Angeles". In: *Journal of Geophysical Research: Solid Earth* 110.4, pp. 1–26.

Aslan, G., M. Foumelis, D. Raucoules, M. De Michele, S. Bernardie, and Z. Cakir (2020). "Landslide mapping and monitoring using persistent scatterer interferometry (PSI) technique in the French alps". In: *Remote Sensing* 12.8.

Bähr, H. (2013). "Orbital effects in spaceborne synthetic aperture radar interferometry". PhD thesis. Karlsruhe Institute of Technology.

Bähr, H., S. Samiei-Esfahany, and R. F. Hanssen (2012). "On The Effect Of Reference Frame Motion On InSAR Deformation Estimates". In: *Proceedings of Fringe 2011*.

Bamler, R., M. Eineder, N. Adam, X. Zhu, and S. Gernhardt (2009). "Interferometric potential of high resolution spaceborne SAR". In: *Photogrammetrie, Fernerkundung, Geoinformation* 2009.5, pp. 407–419.

Bamler, R. and P. Hartl (1998). "Synthetic aperture radar interferometry". In: *Inverse Problems* 14.4, R1–R54.

Bekaert, D. P., A. Hooper, and T. J. Wright (2015a). "A spatially variable power law tropospheric correction technique for InSAR data". In: *Journal of Geophysical Research: Solid Earth* 120.2, pp. 1345–1356.

Bekaert, D. P., R. J. Walters, T. J. Wright, A. J. Hooper, and D. J. Parker (2015b). "Statistical comparison of InSAR tropospheric correction techniques". In: *Remote Sensing of Environment* 170, pp. 40–47.

Belcher, D. P. (2008). "Theoretical limits on SAR imposed by the ionosphere". In: *IET Radar, Sonar and Navigation* 2.6, pp. 435–448.

Bell, F. G., T. R. Stacey, and D. D. Genske (2000). "Mining subsidence and its effect in the environment: Some differing examples". In: *Environmental Geology* 40.1-2, pp. 135–152.

Berardino, P., G. Fornaro, R. Lanari, and E. Sansosti (2002). "A new algorithm for surface deformation monitoring based on small baseline differential SAR interferograms". In: *IEEE Transactions on Geoscience and Remote Sensing* 40.11, pp. 2375–2383.

Blachman, N. M. (1953). "A Comparison of the Informational Capacities of Amplitude- and Phase-Modulation Communication Systems". In: *Proceedings of the IRE* 41.6, pp. 748–759.

Brcic, R. and N. Adam (2013). "Detecting changes in persistent scatterers". In: *International Geoscience and Remote Sensing Symposium (IGARSS)* 1, pp. 117–120.

Bullard, E., J. E. Everett, and A. G. Smith (1965). "The fit of the continents around the Atlantic". In: *Philosophical Transactions of the Royal Society of London. Series A, Mathematical and Physical Sciences* 258.1088, pp. 41–51.

Cattaneo, G., P. Faruolo, U. F. Petrillo, and G. F. Italiano (2010). "Maintaining dynamic minimum spanning trees: An experimental study". In: *Discrete Applied Mathematics* 158.5, pp. 404–425.

Chen, C. W. and H. A. Zebker (2001). "Two-dimensional phase unwrapping with use of statistical models for cost functions in nonlinear optimization". In: *Journal of the Optical Society of America A* 18.2, p. 338.

Chilès, J. P. and P. Delfiner (2012). *Geostatistics: Modeling Spatial Uncertainty: Second Edition*. 2nd ed. Wiley series in probability and statistics. New York: Wiley, pp. 1–699.

Chilès, J. P. and N. Desassis (2018). "Fifty years of kriging". In: *Handbook of Mathematical Geosciences: Fifty Years of IAMG*. Ed. by S. B. Daya, Q. Cheng, and F. Agterberg, pp. 589–612.

Cong, X., U. Balss, F. R. Gonzalez, and M. Eineder (2018). "Mitigation of tropospheric delay in SAR and InSAR using NWP data: Its validation and application examples". In: *Remote Sensing* 10.10.

Copernicus (2019). *EMSN062: Assessing changes in ground subsidence rates, Mekong Delta, Vietnam*. URL: https://emergency.copernicus.eu/mapping/list-of-components/EMSN062 (visited on 03/17/2023).

Cosslett, T. L. and P. D. Cosslett (2014). *Water Resources and Food Security in the Vietnam Mekong Delta*. Vienna, VA: Springer.

Costantini, M., S. Falco, F. Malvarosa, and F. Minati (2008). "A new method for identification and analysis of persistent scatterers in series of sar images". In: *International Geoscience and Remote Sensing Symposium (IGARSS)* 2.1, pp. 449–452.

Costantini, M., F. Minati, F. Trillo, A. Ferretti, F. Novali, E. Passera, J. Dehls, Y. Larsen, P. Marinkovic, M. Eineder, R. Brcic, R. Siegmund, P. Kotzerke, M. Probeck, A. Kenyeres, S. Proietti, L. Solari, and H. S. Andersen (2021). "European Ground Motion Service (Egms)". In: *International Geoscience and Remote Sensing Symposium (IGARSS)* 2021-July, pp. 3293–3296.

Costantini, M., F. Minati, F. Trillo, A. Ferretti, E. Passera, A. Rucci, J. Dehls, Y. Larsen, P. Marinkovic, M. Eineder, R. Brcic, R. Siegmund, P. Kotzerke, A. Kenyeres, V. Costantini, S. Proietti, L. Solari, and H. S. Andersen (2022). "EGMS: Europe-Wide Ground Motion Monitoring based on Full Resolution Insar Processing of All Sentinel-1 Acquisitions". In: *International Geoscience and Remote Sensing Symposium (IGARSS)* 2022-July, pp. 5093–5096.

Crosetto, M., O. Monserrat, A. Barra, M. Cuevas-González, V. Krishnakumar, M. Mróz, and B. Crippa (2019). "A persistent scatterer interferometry procedure to monitor urban subsidence". In: *International Archives of the Photogrammetry, Remote Sensing and Spatial Information Sciences - ISPRS Archives* 42.2/W13, pp. 1921–1926.

Crosetto, M., O. Monserrat, M. Cuevas-González, N. Devanthéry, G. Luzi, and B. Crippa (2015). "Measuring thermal expansion using X-band persistent scatterer interferometry". In: *ISPRS Journal of Photogrammetry and Remote Sensing* 100, pp. 84–91.

Crosetto, M., L. Solari, M. Mróz, J. Balasis-Levinsen, N. Casagli, M. Frei, A. Oyen, D. A. Moldestad, L. Bateson, L. Guerrieri, V. Comerci, and H. S. Andersen (2020). "The evolution of wide-area DInSAR: From regional and national services to the European ground motion service". In: *Remote Sensing* 12.12, pp. 1–20.

Cumming, I. G. and F. Wong (2005). *Digital Processing of Synthetic Aperture Radar Data*. Boston: Artech House.

Curlander, J. C. and R. N. McDonough (1992). *Synthetic aperture radar — systems and signal processing*. New York: Wiley.

D. P. McKenzie and R. L. Parker (1967). "The North Pacific · an Example of Tectonics on a Sphere". In: *Nature* 216, pp. 1276–1280.

Darby, S. E., C. R. Hackney, J. Leyland, M. Kummu, H. Lauri, D. R. Parsons, J. L. Best, A. P. Nicholas, and R. Aalto (2016). "Fluvial sediment supply to a mega-delta reduced by shifting tropical-cyclone activity". In: *Nature* 539.7628, pp. 276–279.

Delacourt, C., P. Briole, and J. Achache (1998). "Tropospheric corrections of SAR interferograms with strong topography. Application to Etna". In: *Geophysical Research Letters* 25.15, pp. 2849–2852.

Deledalle, C. A., L. Denis, and F. Tupin (2011). "NL-InSAR: Nonlocal interferogram estimation". In: *IEEE Transactions on Geoscience and Remote Sensing* 49.4, pp. 1441–1452.

Devanthéry, N., M. Crosetto, O. Monserrat, M. Cuevas-González, and B. Crippa (2014). "An approach to persistent scatterer interferometry". In: *Remote Sensing* 6.7, pp. 6662–6679.

Deverel, S. J. and S. Rojstaczer (1996). "Subsidence of agricultural lands in the Sacramento-San Joaquin Delta, California: Role of aqueous and gaseous carbon fluxes". In: *Water Resources Research* 32.8, pp. 2359–2367.

Dicaprio, C. J. and M. Simons (2008). "Importance of ocean tidal load corrections for differential InSAR". In: *Geophysical Research Letters* 35.22, pp. 1–5.

Dogan, O. and D. Perissin (2014). "Detection of multitransition abrupt changes in multitemporal SAR images". In: *IEEE Journal of Selected Topics in Applied Earth Observations and Remote Sensing* 7.8, pp. 3239–3247.

Doin, M. P., C. Lasserre, G. Peltzer, O. Cavalié, and C. Doubre (2009). "Corrections of stratified tropospheric delays in SAR interferometry: Validation with global atmospheric models". In: *Journal of Applied Geophysics* 69.1, pp. 35–50.

Doin, M.-P., F. Lodge, S. Guillaso, R. Jolivet, C. Lasserre, G. Ducret, R. Grandin, E. Pathier, and V. Pinel (2011). "Presentation of the small baseline NSBAS processing chain on a case example: the Etna deformation monitoring from 2003 to 2010 using Envisat data". In: *ESA Fringe 2011 Workshop*. Frascati, Italy, pp. 19–23.

Don, N. C., N. T. M. Hang, H. Araki, H. Yamanishi, and K. Koga (2006). "Salinization processes in an alluvial coastal lowland plain and effect of sea water level rise". In: *Environmental Geology* 49.5, pp. 743–751.

Dörr, N., A. Schenk, and S. Hinz (2021). "Analysis of Heterogeneous Ps-Insar Derived Subsidence Rates Using Categorized Gis Objects - a Case Study in the Mekong Delta". In: *International Geoscience and Remote Sensing Symposium (IGARSS)*, pp. 2655–2658.

Dörr, N., A. Schenk, and S. Hinz (2022a). "Fully Integrated Temporary Persistent Scatterer Interferometry". In: *IEEE Transactions on Geoscience and Remote Sensing* 60, pp. 1–15.

Dörr, N., A. Schenk, and S. Hinz (2022b). "On the Relevance of Temporary Persistent Scatterers for Long-Term PS-InSAR Monitoring". In: *Proceedings of the European Conference on Synthetic Aperture Radar, EUSAR*. Leipzig, pp. 541–546.

Dörr, N., A. Schenk, and S. Hinz (2022c). "Systematic Analysis of Initial Settlement of new Constructions in the Mekong Delta by Coherence Change Detection of Temporary Persistent Scatterers". In: *International Geoscience and Remote Sensing Symposium (IGARSS)*, pp. 1111–1114.

Dörr, N., A. Schenk, and S. Hinz (2023). "Land Subsidence in the Mekong Delta Derived from Advanced Persistent Scatterer Interferometry with an Infrastructural Reference Network". In review at *IEEE Journal of Selected Topics in Applied Earth Observations and Remote Sensing*.

Duy, N. L., T. V. K. Nguyen, D. V. Nguyen, A. T. Tran, H. T. Nguyen, I. Heidbüchel, B. Merz, and H. Apel (2021). "Groundwater dynamics in the Vietnamese Mekong Delta: Trends, memory effects, and response times". In: *Journal of Hydrology: Regional Studies* 33.October 2020, p. 100746.

Edmonds, D. A., R. L. Caldwell, E. S. Brondizio, and S. M. Siani (2020). "Coastal flooding will disproportionately impact people on river deltas". In: *Nature Communications* 11.1, pp. 1–8.

Eineder, M., C. Minet, P. Steigenberger, X. Cong, and T. Fritz (2011). "Imaging geodesy - Toward centimeter-level ranging accuracy with TerraSAR-X". In: *IEEE Transactions on Geoscience and Remote Sensing* 49.2, pp. 661–671.

Elgered, G. K. (1982). "Tropospheric Wet Path-Delay Measurements". In: *IEEE Transactions on Antennas and Propagation* 30.3, pp. 502–505.

Eltoft, T. (2005). "The Rician inverse Gaussian distribution: A new model for non-Rayleigh signal amplitude statistics". In: *IEEE Transactions on Image Processing* 14.11, pp. 1722–1735.

Engdahl, M. E. and J. M. Hyyppä (2003). "Land-cover classification using multitemporal ERS-1/2 InSAR data". In: *IEEE Transactions on Geoscience and Remote Sensing* 41.7 PART I, pp. 1620–1628.

Erban, L. E., S. M. Gorelick, and H. A. Zebker (2014). "Groundwater extraction, land subsidence, and sea-level rise in the Mekong Delta, Vietnam". In: *Environmental Research Letters* 9.8.

Eslami, S., P. Hoekstra, H. W. Kernkamp, N. Nguyen Trung, D. Do Duc, H. Nguyen Nghia, T. Tran Quang, A. Van Dam, S. E. Darby, D. R. Parsons, G. Vasilopoulos, L. Braat, and M. Van Der Vegt (2021). "Dynamics of salt intrusion in the Mekong Delta: Results of field observations and integrated coastal-inland modelling". In: *Earth Surface Dynamics* 9.4, pp. 953–976.

Ester, M., H.-P. Kriegel, J. Sander, and X. Xu (1996). "Density-Based Clustering Methods". In: *Second International Conference on Knowledge Discovery and Data Mining (KDD-96)*. AAAI Press, pp. 226–231.

Fattahi, H. and F. Amelung (2014). "InSAR uncertainty due to orbital errors". In: *Geophysical Journal International* 199.1, pp. 549–560.

Fattahi, H. and F. Amelung (2015). "InSAR bias and uncertainty due to the systematic and stochastic tropospheric delay". In: *Journal of Geophysical Research: Solid Earth* 120.12, pp. 8758–8773.

Ferretti, A., C. Colesanti, and D. Perissin (2004). "Evaluating the Effect of the Observation Time on the Distribution of SAR Permanent Scatterers". In: *ESA FRINGE 2003 Workshop*. Frascati, Italy.

Ferretti, A., A. Fumagalli, F. Novali, C. Prati, F. Rocca, and A. Rucci (2011). "A new algorithm for processing interferometric data-stacks: SqueeSAR". In: *IEEE Transactions on Geoscience and Remote Sensing* 49.9, pp. 3460–3470.

Ferretti, A., C. Prati, and F. Rocca (2000). "Nonlinear subsidence rate estimation using permanent scatterers in differential SAR interferometry". In: *IEEE Transactions on Geoscience and Remote Sensing* 38.5 I, pp. 2202–2212.

Ferretti, A., C. Prati, and F. Rocca (2001). "Permanent scatterers in SAR interferometry". In: *IEEE Transactions on Geoscience and Remote Sensing* 39.1, pp. 8–20.

Ferretti, A., G. Savio, R. Barzaghi, A. Borghi, S. Musazzi, F. Novali, C. Prati, and F. Rocca (2007). "Submillimeter accuracy of InSAR time series: Experimental validation". In: *IEEE Transactions on Geoscience and Remote Sensing* 45.5, pp. 1142–1153.

Fersch, B., A. Wagner, B. Kamm, E. Shehaj, A. Schenk, P. Yuan, A. Geiger, G. Moeller, B. Heck, S. Hinz, H. Kutterer, and H. Kunstmann (2022). "Tropospheric water vapor: A comprehensive high-resolution data collection for the transnational Upper Rhine Graben region". In: *Earth System Science Data* 14.12, pp. 5287–5307.

Fornaro, G., F. Lombardini, and F. Serafino (2005). "Three-dimensional multipass SAR focusing: Experiments with long-term spaceborne data". In: *IEEE Transactions on Geoscience and Remote Sensing* 43.4, pp. 702–714.

Fornaro, G., D. Reale, and S. Verde (2013). "Bridge thermal dilation monitoring with millimeter sensitivity via multidimensional SAR imaging". In: *IEEE Geoscience and Remote Sensing Letters* 10.4, pp. 677–681.

Fournier, T., M. E. Pritchard, and N. Finnegan (2011). "Accounting for atmospheric delays in InSAR data in a search for long-wavelength deformation in South America". In: *IEEE Transactions on Geoscience and Remote Sensing* 49.10 PART 2, pp. 3856–3867.

Fuhrmann, T. and M. C. Garthwaite (2019). "Resolving three-dimensional surface motion with InSAR: Constraints from multi-geometry data fusion". In: *Remote Sensing* 11.3.

Gabriel, A. K., R. M. Goldstein, and H. A. Zebker (1989). "Mapping small elevation changes over large areas: differential radar interferometry". In: *Journal of Geophysical Research* 94.B7, pp. 9183–9191.

Gaddes, M. E., A. Hooper, and M. Bagnardi (2019). "Using Machine Learning to Automatically Detect Volcanic Unrest in a Time Series of Interferograms". In: *Journal of Geophysical Research: Solid Earth* 124.11, pp. 12304–12322.

Galloway, D. L., K. W. Hudnut, S. E. Ingebritsen, S. P. Phillips, G. Peltzer, F. Rogez, and P. A. Rosen (1998). "Detection of aquifer system compaction and land subsidence using interferometric synthetic aperture radar, Antelope Valley, Mojave Desert, California". In: *Water Resources Research* 34.10, pp. 2573–2585.

Galloway, D. L. and T. J. Burbey (2011). "Review: Regional land subsidence accompanying groundwater extraction". In: *Hydrogeology Journal* 19.8, pp. 1459–1486.

Gernhardt, S. M. (2011). "High Precision 3D Localization and Motion Analysis of Persistent Scatterers using Meter-Resolution Radar Satellite Data". PhD thesis. Technical University of Munich.

Goldhirsh, J. and J. R. Rowland (1982). "A Tutorial Assessment of Atmospheric Height Uncertainties for High-Precision Satellite Altimeter Missions to Monitor Ocean Currents". In: *IEEE Transactions on Geoscience and Remote Sensing* GE-20.4, pp. 418–434.

Goldstein, R. (1995). "Atmospheric limitations to repeat-track radar interferometry". In: *Geophysical Research Letters* 22.18, pp. 2517–2520.

Goldstein, R. M. and C. L. Werner (1998). "Radar interferogram filtering for geophysical applications". In: *Geophysical Research Letters* 25.21, pp. 4035–4038.

Gomba, G., A. Parizzi, F. De Zan, M. Eineder, and R. Bamler (2016). "Toward operational compensation of ionospheric effects in SAR interferograms: The split-spectrum method". In: *IEEE Transactions on Geoscience and Remote Sensing* 54.3, pp. 1446–1461.

Gong, W., F. J. Meyer, S. Liu, and R. F. Hanssen (2015). "Temporal Filtering of InSAR Data Using Statistical Parameters from NWP Models". In: *IEEE Transactions on Geoscience and Remote Sensing* 53.7, pp. 4033–4044.

Gonzalez, F. R., A. Parizzi, and R. Brcic (2018). "Evaluating the impact of geodetic corrections on interferometric deformation measurements". In: *Proceedings of the European Conference on Synthetic Aperture Radar, EUSAR* 2018-June, pp. 377–381.

Goodman, J. W. (2015). *Statistical optics.* John Wiley & Sons.

Goodman, N. R. (1963). "Statistical Analysis Based on a Certain Multivariate Complex Gaussian Distribution (An Introduction)". In: *The Annals of Mathematical Statistics* 34.1, pp. 152–177.

Graham, L. C. (1974). "Synthetic Interferometer Radar For Topographic Mapping". In: *Proceedings of the IEEE* 62.6, pp. 763–768.

Gray, A. L., K. E. Mattar, and G. Sofko (2000). "Influence of Ionospheric Electron Density Fluctuations on Satellite Radar Interferometry". In: *Geophysical Research Letters* 27.10, pp. 1451–1454.

Guarnieri, A. M. and S. Tebaldini (2008). "On the exploitation of target statistics for SAR interferometry applications". In: *IEEE Transactions on Geoscience and Remote Sensing* 46.11, pp. 3436–3443.

Gunnink, J. L., H. V. Pham, G. H. Oude Essink, and M. F. Bierkens (2021). "The three-dimensional groundwater salinity distribution and fresh groundwater volumes in the Mekong Delta, Vietnam, inferred from geostatistical analyses". In: *Earth System Science Data* 13.7, pp. 3297–3319.

Hak, D., K. Nadaoka, L. Patrick Bernado, V. Le Phu, N. Hong Quan, T. Quang Toan, N. Hieu Trung, D. Van Ni, and V. Pham Dang Tri (2016). "Spatio-temporal variations of sea level around the Mekong Delta: Their causes and consequences on the coastal environment". In: *Hydrological Research Letters* 10.2, pp. 60–66.

Hanssen, R. (2001). *Data Interpretation and Error Analysis*. Vol. 91. Dordrecht: Kluwer Academic.

Hanssen, R. F., T. M. Weckwerth, H. A. Zebker, and R. Klees (1999). "High-resolution water vapor mapping from interferometric radar measurements". In: *Science* 283.5406, pp. 1297–1299.

Hersbach, H. et al. (2020). "The ERA5 global reanalysis". In: *Quarterly Journal of the Royal Meteorological Society* 146.730, pp. 1999–2049.

Hoffmann, J. and H. A. Zebker (2003). "Prospecting for horizontal surface displacements in Antelope Valley, California, using satellite radar interferometry". In: *Journal of Geophysical Research: Earth Surface* 108.6011.

Hooper, A., P. Segall, and H. Zebker (2007). "Persistent scatterer interferometric synthetic aperture radar for crustal deformation analysis, with application to Volcán Alcedo, Galápagos". In: *Journal of Geophysical Research: Solid Earth* 112.7, pp. 1–21.

Hooper, A. (2010). "A statistical-cost Approach to Unwrapping the Phase of InSAR Time series". In: *International Workshop on ERS SAR*. March.

Hooper, A., D. Bekaert, K. Spaans, and M. Arikan (2012). "Recent advances in SAR interferometry time series analysis for measuring crustal deformation". In: *Tectonophysics* 514-517, pp. 1–13.

Hooper, A., H. Zebker, P. Segall, and B. Kampes (2004). "A new method for measuring deformation on volcanoes and other natural terrains using InSAR persistent scatterers". In: *Geophysical Research Letters* 31.23, pp. 1–5.

Hooper, A. and H. A. Zebker (2007). "Phase unwrapping in three dimensions with application to InSAR time series". In: *Journal of the Optical Society of America A* 24.9, p. 2737.

Hooper, A. J. (2008). "A multi-temporal InSAR method incorporating both persistent scatterer and small baseline approaches". In: *Geophysical Research Letters* 35.16, pp. 1–5.

Hou, J., B. Xu, Z. Li, Y. Zhu, and G. Feng (2021). "Block PS-InSAR ground deformation estimation for large-scale areas based on network adjustment". In: *Journal of Geodesy* 95.10, pp. 1–15.

Hu, F., J. Wu, L. Chang, and R. F. Hanssen (2019). "Incorporating Temporary Coherent Scatterers in Multi-Temporal InSAR Using Adaptive Temporal Subsets". In: *IEEE Transactions on Geoscience and Remote Sensing* 57.10, pp. 7658–7670.

Hu, J., Z. W. Li, X. L. Ding, J. J. Zhu, L. Zhang, and Q. Sun (2014). "Resolving three-dimensional surface displacements from InSAR measurements: A review". In: *Earth-Science Reviews* 133, pp. 1–17.

Hu, Z. and J. J. Mallorquí (2019). "An accurate method to correct atmospheric phase delay for InSAR with the ERA5 global atmospheric model". In: *Remote Sensing* 11.17.

Huang, S. A. and H. A. Zebker (2022). "InSAR Time-Series Analysis With a Non-Gaussian Detector for Persistent Scatterers". In: *IEEE Journal of Selected Topics in Applied Earth Observations and Remote Sensing* 15, pp. 9208–9225.

Jacob, A. W., C. Notarnicola, G. Suresh, O. Antropov, S. Ge, J. Praks, Y. Ban, E. Pottier, J. J. Mallorqui Franquet, J. Duro, M. E. Engdahl, F. Vicente-Guijalba, C. Lopez-Martinez, J. M. Lopez-Sanchez, M. Litzinger, H. Kristen, A. Mestre-Quereda, D. Ziolkowski, and M. Lavalle (2020). "Sentinel-1 InSAR Coherence for Land Cover Mapping: A Comparison of Multiple Feature-Based Classifiers". In: *IEEE Journal of Selected Topics in Applied Earth Observations and Remote Sensing* 13, pp. 535–552.

Jiang, M., X. Ding, Z. Li, X. Tian, C. Wang, and W. Zhu (2014). "InSAR coherence estimation for small data sets and its impact on temporal decorrelation extraction". In: *IEEE Transactions on Geoscience and Remote Sensing* 52.10, pp. 6584–6596.

Jolivet, R., R. Grandin, C. Lasserre, M. P. Doin, and G. Peltzer (2011). "Systematic InSAR tropospheric phase delay corrections from global meteorological reanalysis data". In: *Geophysical Research Letters* 38.17, pp. 1–6.

Jónsson, S., H. Zebker, P. Segall, and F. Amelung (2002). "Fault slip distribution of the 1999 Mw 7.1 Hector Mine, California, earthquake, estimated from satellite radar and GPS measurements". In: *Bulletin of the Seismological Society of America* 92.4, pp. 1377–1389.

Just, D. and R. Bamler (1994). "Phase statistics of interferograms with applications to synthetic aperture radar". In: *Applied Optics* 33.20, p. 4361.

Kampes, B. M. (2005). "Displacement Parameter Estimation using Permanent Scatterer Interferometry". PhD thesis. TU Delft.

Kampes, B. M. and R. F. Hanssen (2004). "Ambiguity resolution for permanent scatterer interferometry". In: *IEEE Transactions on Geoscience and Remote Sensing* 42.11, pp. 2446–2453.

Karlsrud, K., L. Tunbridge, N. Q. Khanh, and N. Q. Dinh (2020). "Preliminary results of land subsidence monitoring in the Ca Mau Province". In: *Proceedings of the International Association of Hydrological Sciences* 382, pp. 111–115.

Knospe, S. H. and S. Jónsson (2010). "Covariance estimation for dInSAR surface deformation measurements in the presence of anisotropic atmospheric noise". In: *IEEE Transactions on Geoscience and Remote Sensing* 48.4 PART 2, pp. 2057–2065.

Kondolf, G. M., Z. K. Rubin, and J. T. Minear (2014). "Dams on the Mekong: Cumulative sediment starvation". In: *Water Resources Research* 50.6, pp. 5158–5169.

Kumiko, T., M. Takao, and M. Toru (2008). "Seasonal changes in radiation and evaporation implied from the diurnal distribution of rainfall in the Lower Mekong". In: *Hydrological Processes* 22.9, pp. 1257–1266.

Kuruoğlu, E. E. and J. Zerubia (2004). "Modeling SAR images with a generalization of the Rayleigh distribution". In: *IEEE Transactions on Image Processing* 13.4, pp. 527–533.

Lanari, R., O. Mora, M. Manunta, J. J. Mallorquí, P. Berardino, and E. Sansosti (2004). "A small-baseline approach for investigating deformations on full-resolution differential SAR interferograms". In: *IEEE Transactions on Geoscience and Remote Sensing* 42.7, pp. 1377–1386.

Lee, J. S., A. R. Miller, and S. A. Mango (1994). "Intensity and Phase Statistics of Multilook Polarimetric and Interferometric SAR Imagery". In: *IEEE Transactions on Geoscience and Remote Sensing* 32.5, pp. 1017–1028.

Leijen, F. van (2014). "Persistent Scatterer Interferometry based on geodetic estimation theory". PhD thesis. TU Delft.

Liang, C., P. Agram, M. Simons, and E. J. Fielding (2019). "Ionospheric correction of InSAR time series analysis of C-band sentinel-1 TOPS data". In: *IEEE Transactions on Geoscience and Remote Sensing* 57.9, pp. 6755–6773.

Liu, S., R. Hanssen, and Á. Mika (2009). "On the value of high-resolution weather models for atmospheric mitigation in SAR interferometry". In: *International Geoscience and Remote Sensing Symposium (IGARSS)* 2, pp. II–749–II–752.

Liu, Y., G. Wang, X. Yu, and K. Wang (2022). "Sentinel-1 InSAR and GPS-Integrated Long-Term and Seasonal Subsidence Monitoring in Houston, Texas, USA". In: *Remote Sensing* 14.23.

Liu, Z., C. Zhou, H. Fu, J. Zhu, and T. Zuo (2020). "A framework for correcting ionospheric artifacts and atmospheric effects to generate high accuracy InSAR DEM". In: *Remote Sensing* 12.2.

Ljung, G. M. and G. E. Box (1978). "On a measure of lack of fit in time series models". In: *Biometrika* 65.2, pp. 297–303.

Lundgren, P., E. A. Hetland, Z. Liu, and E. J. Fielding (2009). "Southern San Andreas-San Jacinto fault system slip rates estimated from earthquake cycle models constrained by GPS and interferometric synthetic aperture radar observations". In: *Journal of Geophysical Research: Solid Earth* 114.2, pp. 1–18.

Mahapatra, P., H. van der Marel, F. van Leijen, S. Samiei-Esfahany, R. Klees, and R. Hanssen (2018). "InSAR datum connection using GNSS-augmented radar transponders". In: *Journal of Geodesy* 92.1, pp. 21–32.

Martinez, J. D., K. S. Johnson, and J. T. Neal (1998). "Sinkholes in Evaporite Rocks". In: *American Scientist* 86.1, pp. 38–51.

Massonnet, D. and K. L. Feigl (1998). "Radar interferometry and its application to changes in the earth's surface". In: *Reviews of Geophysics* 36.4, pp. 441–500.

Massonnet, D., M. Rossi, C. Carmona, F. Adragna, G. Peltzer, K. Feigl, and T. Rabaute (1993). "The displacement field of the Landers earthquake mapped by radar interferometry". In: *Nature* 364.6433, pp. 138–142.

Meckel, T. A., U. S. ten Brink, and S. J. Williams (2006). "Current subsidence rates due to compaction of Holocene sediments in southern Louisiana". In: *Geophysical Research Letters* 33.11, pp. 1–5.

Meyer, F., R. Bamler, N. Jakowski, and T. Fritz (2006). "The potential of low-frequency SAR systems for mapping ionospheric TEC distributions". In: *IEEE Geoscience and Remote Sensing Letters* 3.4, pp. 560–564.

Milbert, D. (2018). *Solid Earth Tide*. URL: https://geodesyworld.github.io/SOFTS/solid.htm.

Milillo, P., G. Giardina, M. J. DeJong, D. Perissin, and G. Milillo (2018). "Multi-temporal InSAR structural damage assessment: The London crossrail case study". In: *Remote Sensing* 10.2, pp. 20–22.

Miller, M. M. and M. Shirzaei (2019). "Land subsidence in Houston correlated with flooding from Hurricane Harvey". In: *Remote Sensing of Environment* 225, pp. 368–378.

Minderhoud, P. S., L. Coumou, L. E. Erban, H. Middelkoop, E. Stouthamer, and E. A. Addink (2018). "The relation between land use and subsidence in the Vietnamese Mekong delta". In: *Science of the Total Environment* 634, pp. 715–726.

Minderhoud, P. S., L. Coumou, G. Erkens, H. Middelkoop, and E. Stouthamer (2019). "Mekong delta much lower than previously assumed in sea-level rise impact assessments". In: *Nature Communications* 10.1, pp. 1–13.

Minderhoud, P. S., G. Erkens, V. H. Pham, V. T. Bui, L. Erban, H. Kooi, and E. Stouthamer (2017). "Impacts of 25 years of groundwater extraction on subsidence in the Mekong delta, Vietnam". In: *Environmental Research Letters* 12.6.

Minderhoud, P. S., I. Hlavacova, J. Kolomaznik, and O. Neussner (2020). "Towards unraveling total subsidence of a mega-delta-the potential of new PS InSAR data for the Mekong delta". In: *Proceedings of the International Association of Hydrological Sciences* 382, pp. 327–332.

Minh, D. H. T., R. Hanssen, and F. Rocca (2020). "Radar interferometry: 20 years of development in time series techniques and future perspectives". In: *Remote Sensing* 12.9, pp. 1–18.

Monserrat, O., M. Crosetto, M. Cuevas, and B. Crippa (2011). "The thermal expansion component of persistent scatterer interferometry observations". In: *IEEE Geoscience and Remote Sensing Letters* 8.5, pp. 864–868.

Monti-Guarnieri, A. V., M. A. Brovelli, M. Manzoni, M. Mariotti D'Alessandro, M. E. Molinari, and D. Oxoli (2018). "Coherent change detection for multipass SAR". In: *IEEE Transactions on Geoscience and Remote Sensing* 56.11, pp. 6811–6822.

Morishita, Y., M. Lazecky, T. J. Wright, J. R. Weiss, J. R. Elliott, and A. Hooper (2020). "LiCSBAS: An open-source insar time series analysis package integrated with the LiCSAR automated sentinel-1 InSAR processor". In: *Remote Sensing* 12.3, pp. 5–8.

Moritz, H. (1978). "Least-squares collocation". In: *Reviews of Geophysics* 16.3, pp. 421–430.

Mukherjee, S., A. Zimmer, X. Sun, P. Ghuman, and I. Cheng (2021). "An Unsupervised Generative Neural Approach for InSAR Phase Filtering and Coherence Estimation". In: *IEEE Geoscience and Remote Sensing Letters* 18.11, pp. 1971–1975.

Murray, K. D., R. B. Lohman, and D. P. Bekaert (2021). "Cluster-Based Empirical Tropospheric Corrections Applied to InSAR Time Series Analysis". In: *IEEE Transactions on Geoscience and Remote Sensing* 59.3, pp. 2204–2212.

Navarro-Sanchez, V. D. and J. M. Lopez-Sanchez (2012). "Improvement of persistent-scatterer interferometry performance by means of a polarimetric optimization". In: *IEEE Geoscience and Remote Sensing Letters* 9.4, pp. 609–613.

Neely, W. R., A. A. Borsa, and F. Silverii (2020). "GInSAR: A cGPS Correction for Enhanced InSAR Time Series". In: *IEEE Transactions on Geoscience and Remote Sensing* 58.1, pp. 136–146.

Nelson, F. E., O. A. Anisimov, and N. I. Shiklomanov (2001). "Subsidence risk from thawing permafrost". In: *Nature* 410.6831, pp. 889–890.

Papoulis, A. and S. U. Pillai (2002). *Probability, random variables, and stochastic processes.* 4th ed. New York: McGraw-Hill.

Parizzi, A., R. Brcic, and F. De Zan (2021). "InSAR Performance for Large-Scale Deformation Measurement". In: *IEEE Transactions on Geoscience and Remote Sensing* 59.10, pp. 8510–8520.

Parizzi, A., F. R. Gonzalez, and R. Brcic (2020). "A covariance-based approach to merging InSAR and GNSS displacement rate measurements". In: *Remote Sensing* 12.2.

Pavlis, N. K., S. A. Holmes, S. C. Kenyon, and J. K. Factor (2012). "The development and evaluation of the Earth Gravitational Model 2008 (EGM2008)". In: *Journal of Geophysical Research: Solid Earth* 117.4, pp. 1–38.

Peng, W., Q. Wang, F. B. Zhan, and Y. Cao (2020). "Spatiotemporal Ocean Tidal Loading in InSAR Measurements Determined by Kinematic PPP Solutions of a Regional GPS Network". In: *IEEE Journal of Selected Topics in Applied Earth Observations and Remote Sensing* 13, pp. 3772–3779.

Pepe, A. and F. Calò (2017). "A review of interferometric synthetic aperture RADAR (InSAR) multi-track approaches for the retrieval of Earth's Surface displacements". In: *Applied Sciences* 7.12.

Pepe, A. and R. Lanari (2006). "On the extension of the minimum cost flow algorithm for phase unwrapping of multitemporal differential SAR interferograms". In: *IEEE Transactions on Geoscience and Remote Sensing* 44.9, pp. 2374–2383.

Perissin, D. and A. Ferretti (2007). "Urban-target recognition by means of repeated spaceborne SAR images". In: *IEEE Transactions on Geoscience and Remote Sensing* 45.12, pp. 4043–4058.

Perissin, D. and T. Wang (2012). "Repeat-pass SAR interferometry with partially coherent targets". In: *IEEE Transactions on Geoscience and Remote Sensing* 50.1, pp. 271–280.

Perissin, D., Z. Wang, and T. Wang (2011). "The SARPROZ InSAR tool for urban subsidence/manmade structure stability monitoring in China". In: *34th International Symposium on Remote Sensing of Environment - The GEOSS Era: Towards Operational Environmental Monitoring*.

Phan, D. C., T. H. Trung, V. T. Truong, T. Sasagawa, T. P. T. Vu, D. T. Bui, M. Hayashi, T. Tadono, and K. N. Nasahara (2021). "First comprehensive quantification of annual land use/cover from 1990 to 2020 across mainland Vietnam". In: *Scientific Reports* 11.1, pp. 1–20.

Phien-wej, N., P. H. Giao, and P. Nutalaya (2006). "Land subsidence in Bangkok, Thailand". In: *Engineering Geology* 82.4, pp. 187–201.

Poland, J. F. and G. H. Davis (1969). "Land subsidence due to withdrawal of fluids". In: *GSA Reviews in Engineering Geology* 2, pp. 187–269.

Pritchard, M. E., M. Simons, P. A. Rosen, S. Hensley, and F. H. Webb (2002). "Co-seismic slip from the 1995 July 30 Mw = 8.1 Antofagasta, Chile, earthquake as constrained by InSAR and GPS observations". In: *Geophysical Journal International* 150.2, pp. 362–376.

Rebmeister, M., A. Schenk, P. E. Bradley, N. Dörr, and S. Hinz (2021). "OCLeaS - A tomographic PSI algorithm using orthogonal matching pursuit and complex least squares". In: *Procedia Computer Science* 181.2019, pp. 220–230.

Rice, S. O. (1948). "Statistical Properties of a Sine Wave Plus Random Noise". In: *Bell System Technical Journal* 27.1, pp. 109–157.

Rignot, E., K. C. Jezek, and H. G. Sohn (1995). "Ice flow dynamics of the Greenland Ice Sheet from SAR interferometry". In: *Geophysical Research Letters* 22.5, pp. 575–578.

Rizzoli, P., M. Martone, C. Gonzalez, C. Wecklich, D. Borla Tridon, B. Bräutigam, M. Bachmann, D. Schulze, T. Fritz, M. Huber, B. Wessel, G. Krieger, M. Zink, and A. Moreira (2017). "Generation and performance assessment of the global TanDEM-X digital elevation model". In: *ISPRS Journal of Photogrammetry and Remote Sensing* 132, pp. 119–139.

Rodriguez, E. and J. M. Martin (1992). "Theory and design of interferometric synthetic aperture radars". In: *IEE Proceedings, Part F: Radar and Signal Processing* 139.2, pp. 147–159.

Rosen, P., S. Hensley, I. Joughin, F. Li, S. Madsen, E. Rodriguez, and R. Goldstein (2000). "Synthetic aperture radar interferometry". In: *Proceedings of the IEEE* 88.3, pp. 333–382.

Rosen, P. A., S. Hensley, and C. Chen (2010). "Measurement and mitigation of the ionosphere in L-band Interferometric SAR data". In: *IEEE National Radar Conference - Proceedings*, pp. 1459–1463.

Sadeghi, Z., M. J. Valadan Zoej, A. Hooper, and J. M. Lopez-Sanchez (2018). "A new polarimetric persistent scatterer interferometry method using temporal coherence optimization". In: *IEEE Transactions on Geoscience and Remote Sensing* 56.11, pp. 6547–6555.

Samiei-Esfahany, S., J. E. Martins, F. Van Leijen, and R. F. Hanssen (2016). "Phase Estimation for Distributed Scatterers in InSAR Stacks Using Integer Least Squares Estimation". In: *IEEE Transactions on Geoscience and Remote Sensing* 54.10, pp. 5671–5687.

Schenk, A. (2015). "PS-Interferometrie in urbanen Räumen - Optimierte Schätzung von Oberflächenbewegungen mittels Multi-SBAS Verfahren". PhD thesis. Karlsruhe Institute of Technology.

Schneider, P. J. and U. Soergel (2021). "Segmentation of buildings based on high resolution persistent scatterer point clouds". In: *ISPRS Annals of the Photogrammetry, Remote Sensing and Spatial Information Sciences* 5.3, pp. 65–71.

Seymour, M. S. and I. G. Cumming (1994). "Maximum likelihood estimation for SAR interferometry". In: *International Geoscience and Remote Sensing Symposium (IGARSS)*. Vol. 4, pp. 2272–2274.

Shanker, P. and H. Zebker (2007). "Persistent scatterer selection using maximum likelihood estimation". In: *Geophysical Research Letters* 34.22, pp. 2–5.

Skolnik, M. I. (1999). *Introduction to Radar Systems*. 2nd ed. Vol. 19. 2. New York: McGraw-Hill.

Smajgl, A., T. Q. Toan, D. K. Nhan, J. Ward, N. H. Trung, L. Q. Tri, V. P. Tri, and P. T. Vu (2015). "Responding to rising sea levels in the Mekong Delta". In: *Nature Climate Change* 5.2, pp. 167–174.

Smith, E. K. and S. Weintraub (1953). "The Constants in the Equation for Atmospheric Refractive Index at Radio Frequencies". In: *Proceedings of the IRE* 41.8, pp. 1035–1037.

Snoeij, P., N. Van Der Valk, E. Boom, and D. Hoekman (2001). "Effect of the ionosphere on P-band spaceborne SAR images". In: *International Geoscience and Remote Sensing Symposium (IGARSS)* 1.C, pp. 132–134.

Stephens, J. C., L. H. Allen, and E. Chen (1984). "Organic soil subsidence". In: *GSA Reviews in Engineering Geology* 6, pp. 107–122.

Stephenson, O. L., Y. K. Liu, Z. Yunjun, M. Simons, P. Rosen, and X. Xu (2022). "The Impact of Plate Motions on Long-Wavelength InSAR-Derived Velocity Fields". In: *Geophysical Research Letters* 49.21.

Syvitski, J. P., A. J. Kettner, I. Overeem, E. W. Hutton, M. T. Hannon, G. R. Brakenridge, J. Day, C. Vörösmarty, Y. Saito, L. Giosan, and R. J. Nicholls (2009). "Sinking deltas due to human activities". In: *Nature Geoscience* 2.10, pp. 681–686.

Tarantola, A. (2005). *Inverse Problem Theory*. Paris, France: Society for Industrial and Applied Mathematics.

Tarayre, H. and D. Massonnet (1994). "Effects of a refractive atmosphere on interferometric processing". In: *International Geoscience and Remote Sensing Symposium (IGARSS)* 2.4, pp. 717–719.

Teatini, P., L. Tosi, and T. Strozzi (2011). "Quantitative evidence that compaction of Holocene sediments drives the present land subsidence of the Po Delta, Italy". In: *Journal of Geophysical Research: Solid Earth* 116.8, pp. 1–10.

Teunissen, P. J. G. (1995). "The least-squares ambiguity decorrelation adjustment: a method for fast GPS integer ambiguity estimation". In: *Journal of Geodesy* 70, pp. 65–82.

Teunissen, P. J. G., P. J. de Jonge, and C. C. J. M. Tiberius (1995). "The LAMBDA-Method for Fast GPS Surveying". In: *Proceedings of International Symposium «GPS technology applications»'* 1, pp. 203–210.

Tiwari, A., A. B. Narayan, and O. Dikshit (2020). "Deep learning networks for selection of measurement pixels in multi-temporal SAR interferometric processing". In: *ISPRS Journal of Photogrammetry and Remote Sensing* 166, pp. 169–182.

Tomás, R., J. I. Pagán, J. A. Navarro, M. Cano, J. L. Pastor, A. Riquelme, M. Cuevas-González, M. Crosetto, A. Barra, O. Monserrat, J. M. Lopez-Sanchez, A. Ramón, S. Ivorra, M. Del Soldato, L. Solari, S. Bianchini, F. Raspini, F. Novali, A. Ferretti, M. Costantini, F. Trillo, G. Herrera, and N. Casagli (2019). "Semi-automatic identification and pre-screening of geological-geotechnical deformational processes using persistent scatterer interferometry datasets". In: *Remote Sensing* 11.14.

Tosi, L., P. Teatini, L. Carbognin, and G. Brancolini (2009). "Using high resolution data to reveal depth-dependent mechanisms that drive land subsidence: The Venice coast, Italy". In: *Tectonophysics* 474.1-2, pp. 271–284.

Trunk, G. V. (1972). "Radar Properties of Non-Rayleigh Sea Clutter." In: *IEEE Transactions on Aerospace and Electronic Systems* AES-8.2, pp. 196–204.

Van Leijen, F. J. and R. F. Hanssen (2007). "Persistent scatterer density improvement using adaptive deformation models". In: *International Geoscience and Remote Sensing Symposium (IGARSS)*, pp. 2102–2105.

Van Nguyen, L., T. K. O. Ta, and M. Tateishi (2000). "Late Holocene depositional environments and coastal evolution of the Mekong River Delta, Southern Vietnam". In: *Journal of Asian Earth Sciences* 18.4, pp. 427–439.

Vu, D. T., S. Bruinsma, S. Bonvalot, D. Remy, and G. S. Vergos (2020). "A quasigeoid-derived transformation model accounting for land subsidence in the mekong delta towards height system unification in Vietnam". In: *Remote Sensing* 12.5, pp. 1–21.

Wackernagel, H. (2013). *Multivariate geostatistics: an introduction with applications*. Springer Science & Business Media.

Wang, G. Y., G. You, B. Shi, J. Yu, and M. Tuck (2009). "Long-term land subsidence and strata compression in Changzhou, China". In: *Engineering Geology* 104.1-2, pp. 109–118.

Wang, K. and J. Chen (2022). "Accurate Persistent Scatterer Identification Based on Phase Similarity of Radar Pixels". In: *IEEE Transactions on Geoscience and Remote Sensing* 60, pp. 1–1.

Werner, C., U. Wegmüller, T. Strozzi, and A. Wiesmann (2003). "Interferometric Point Target Analysis for Deformation Mapping". In: *International Geoscience and Remote Sensing Symposium (IGARSS)* 7.1, pp. 4362–4364.

Wicks, C. W., D. Dzurisin, S. Ingebritsen, W. Thatcher, Z. Lu, and J. Iverson (2002). "Magmatic activity beneath the quiescent Three Sisters volcanic center, central Oregon Cascade Range, USA". In: *Geophysical Research Letters* 29.7, pp. 26–1–26–4.

Williams, S., Y. Bock, P. Fang, and H. Cecil (1998). "Aperture Radar Products". In: *Network* 98, pp. 51–67.

Wit, K. de, B. R. Lexmond, E. Stouthamer, O. Neussner, N. Dörr, A. Schenk, and P. S. Minderhoud (2021). "Identifying causes of urban differential subsidence in the

Vietnamese mekong delta by combining insar and field observations". In: *Remote Sensing* 13.2, pp. 1–33.

Wright, T. J., B. E. Parsons, and Z. Lu (2004). "Toward mapping surface deformation in three dimensions using InSAR". In: *Geophysical Research Letters* 31.1, pp. 1–5.

Xu, X. and D. T. Sandwell (2020). "Toward Absolute Phase Change Recovery with InSAR: Correcting for Earth Tides and Phase Unwrapping Ambiguities". In: *IEEE Transactions on Geoscience and Remote Sensing* 58.1, pp. 726–733.

Xu, X., D. T. Sandwell, E. Klein, and Y. Bock (2021). "Integrated Sentinel-1 InSAR and GNSS Time-Series Along the San Andreas Fault System". In: *Journal of Geophysical Research: Solid Earth* 126.11, pp. 1–14.

Yague-Martinez, N., P. Prats-Iraola, F. R. Gonzalez, R. Brcic, R. Shau, D. Geudtner, M. Eineder, and R. Bamler (2016). "Interferometric Processing of Sentinel-1 TOPS Data". In: *IEEE Transactions on Geoscience and Remote Sensing* 54.4, pp. 2220–2234.

Yang, C. H., Y. Pang, and U. Soergel (2017). "Monitoring of Building Construction by 4D Change Detection Using Multi-temporal SAR Images". In: *ISPRS Annals of the Photogrammetry, Remote Sensing and Spatial Information Sciences* 4.1W1, pp. 35–42.

Yang, C. H. and U. Soergel (2018). "Adaptive 4D Psi-Based Change Detection". In: *ISPRS Annals of the Photogrammetry, Remote Sensing and Spatial Information Sciences* 4.3, pp. 245–250.

Yu, C., Z. Li, N. T. Penna, and P. Crippa (2018). "Generic Atmospheric Correction Model for Interferometric Synthetic Aperture Radar Observations". In: *Journal of Geophysical Research: Solid Earth* 123.10, pp. 9202–9222.

Yunjun, Z., H. Fattahi, X. Pi, P. Rosen, M. Simons, P. Agram, and Y. Aoki (2022). "Range Geolocation Accuracy of C-/L-Band SAR and its Implications for Operational Stack Coregistration". In: *IEEE Transactions on Geoscience and Remote Sensing* 60.

Zebker, H. A. and R. M. Goldstein (1985). "Topographic Mapping From Interferometric Synthetic Aperture Radar Observations." In: *Digest - International Geoscience and Remote Sensing Symposium (IGARSS)* 91.B5, pp. 113–117.

Zebker, H. A., P. A. Rosen, and S. Hensley (1997). "Atmospheric effects in interferometric synthetic aperture radar surface deformation and topographic maps". In: *Journal of Geophysical Research: Solid Earth* 102.B4, pp. 7547–7563.

Zebker, H. A. and J. Villasenor (1992). "Decorrelation in interferometric radar echoes". In: *IEEE Transactions on Geoscience and Remote Sensing* 30.5, pp. 950–959.

Zhang, L., X. Ding, and Z. Lu (2011). "Ground settlement monitoring based on temporarily coherent points between two SAR acquisitions". In: *ISPRS Journal of Photogrammetry and Remote Sensing* 66.1, pp. 146–152.

Zhang, Y., K. Fu, X. Sun, G. Xu, and H. Wang (2016). "Model accuracy comparison for high resolution insar coherence statistics over Urban Areas". In: *International Archives of the Photogrammetry, Remote Sensing and Spatial Information Sciences - ISPRS Archives* 41.July, pp. 753–756.

Zhou, L., H. Yu, V. Pascazio, and M. Xing (2022). "PU-GAN: A One-Step 2-D InSAR Phase Unwrapping Based on Conditional Generative Adversarial Network". In: *IEEE Transactions on Geoscience and Remote Sensing* 60.

Zhu, X. X. and R. Bamler (2010a). "Tomographic SAR inversion by L1-norm regularization-the compressive sensing approach". In: *IEEE Transactions on Geoscience and Remote Sensing* 48.10, pp. 3839–3846.

Zhu, X. X. and R. Bamler (2010b). "Very high resolution spaceborne SAR tomography in urban environment". In: *IEEE Transactions on Geoscience and Remote Sensing* 48.12, pp. 4296–4308.

Zhu, X. X., S. Montazeri, C. Gisinger, R. F. Hanssen, and R. Bamler (2016). "Geodetic SAR Tomography". In: *IEEE Transactions on Geoscience and Remote Sensing* 54.1, pp. 18–35.

Zoccarato, C., P. S. Minderhoud, and P. Teatini (2018). "The role of sedimentation and natural compaction in a prograding delta: insights from the mega Mekong delta, Vietnam". In: *Scientific Reports* 8.1, pp. 1–12.

Zou, L., J. Kent, N. S. Lam, H. Cai, Y. Qiang, and K. Li (2016). "Evaluating land subsidence rates and their implications for land loss in the Lower Mississippi River Basin". In: *Water (Switzerland)* 8.1, pp. 1–15.

List of Figures

List of Tables

List of Publications

The following list includes publications which have been published by or with me within the scope of the presented thesis. The ideas and results of this thesis have been partly published in those publications.

Publications:

Dörr, N., Schenk, A., Hinz, S. (2022). Fully Integrated Temporary Persistent Scatterer Interferometry. *IEEE Transactions on Geoscience and Remote Sensing*, vol. 60, 1-15, Art no. 4412815.

Dörr, N., Schenk, A., Hinz, S. (2022). Systematic Analysis of Initial Settlement of New Constructions in the Mekong Delta by Coherence Change Detection of Temporary Persistent Scatterers. In proceedings of *2022 IEEE International Geoscience and Remote Sensing Symposium IGARSS*, 1111-1114.

Dörr, N., Schenk, A., Hinz, S. (2022). On the Relevance of Temporary Persistent Scatterers for Long-Term PS-InSAR Monitoring. In proceedings of *EUSAR 2022; 14th European Conference on Synthetic Aperture Radar*, 541-546.

Dörr, N., Schenk, A., Hinz, S. (2021). Analysis of heterogeneous PS-InSAR derived subsidence rates using categorized GIS objects - A case study in the Mekong Delta. In proceedings of *2021 IEEE International Geoscience and Remote Sensing Symposium IGARSS*, 2655-2658.

Rebmeister, M., Schenk, A., Bradley, P.E., **Dörr, N.**, Hinz, S. (2021). OCLeaS – A tomographic PSI Algorithm using Orthogonal Matching Pursuit and Complex Least Squares. *Procedia Computer Science*, Volume 181, 220-230.

Wit, K.d., Lexmond, B.R., Stouthamer, E., Neussner, O., **Dörr, N.**, Schenk, A., Minderhoud, P.S.J. (2021). Identifying Causes of Urban Differential Subsidence in the Vietnamese Mekong Delta by Combining InSAR and Field Observations. *Remote Sensing*, 13, 189.

A. Appendix

A.1. Statistical Tests for the Selection of Reference Areas

Large bridges with deep foundations were selected as additional reference areas in referencing scenario 2 in the application of M-SBAS-2-StaMPS to subsidence monitoring in the VMD, described in Section 6.4. Bridges with length larger than 250 m were selected as potential reference areas. Afterward, various statistical tests were carried out with the goals to (i) identify and remove (T)PSs which are actually not located on the bridges or located on parts of the bridges which are actually moving over time, (ii) identify and remove bridges which are subsiding or moving horizontally. The tests are summarized in the following.

The selection of (T)PSs on potential reference bridges included the following requirements and steps:

- Reference bridge (T)PSs are located within estimated bridge polygons.

- There must be more than two potential reference (T)PSs identified within bridge polygons in order that this bridge is further considered as a potential reference bridge.

- The linear displacement rate of a potential reference (T)PS, which was estimated in the phase noise estimation step in M-SBAS, must not deviate more than 1.5 of the mean absolute deviation (MAD) of all potential reference (T)PSs on the same bridge. The weights are computed by multiplying the normalized inverse distance from the bridge center with the estimated coherence.

- The displacement standard deviation of a potential reference (T)PS must not exceed the double of the MAD of all potential reference (T)PS on the same bridge after subtraction of the weighted median phase time series of all potential reference points on the bridge.

After the selection of the reference (T)PSs on potential reference bridges, reference bridges which are subsiding with regard to surrounding potential reference bridges were identified and dropped. Subsiding bridges were identified in a triangulation network between all potential reference areas. For this purpose, the average differential subsidence time series along edges of connected potential reference areas were calculated, and differential rates were estimated. Bridge connections which featured an estimated differential rate above a threshold were removed. The threshold was
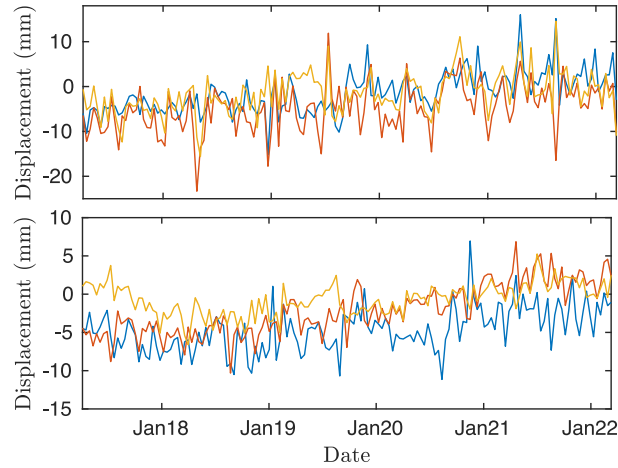
Figure A.1.: Exemplary double differential subsidence time series between ascending and descending stack and along edges of connected reference areas in a triangulation network. The two subfigures show three time series along connections to a dropped bridge, respectively.

empirically determined as a function of the edge length, in order to account for potentially increasingly biased rate estimations with increasing edge length due to temporally correlated noise in the data. At the end, bridges without connections to other bridges were dropped from the set of potential bridges.

In a last step, the remaining reference areas were tested for horizontal movements by combining observations from the descending and ascending stacks. We spanned a triangulation network between all remaining potential reference areas, including solid rock outcrops and potential reference bridges, with the purpose to identify horizontally moving areas or (T)PSs on them. First, weighted mean subsidence time series of each potential reference area in both the descending and ascending stacks were computed. Then, subsidence time series differences were computed along each edge in the triangulation network to get an estimate of the differential subsidence time series between connected potential reference areas. We assumed that the differential subsidence time series should be similar in the ascending and descending stack if none of the involved reference areas is moving horizontally. In order to test this, we interpolated the differential subsidence time series d_z between the reference areas in descending and ascending stacks onto common time instances and subtracted them. Subsequently, we applied the Ljung-Box-Test (Equation 5.10), as done for the TPS datum reformulation in Section 5.3.5, to test if the differences are stationary without any autocorrelation exhibited. If the null hypothesis was rejected, we concluded that one of the involved bridges is moving horizontally and the edge between the two was removed. At the end, isolated bridges without connections to others were dropped from the set of reference areas. Double-differential subsidence time series between the results of both stacks and along connections of two dropped bridges to neighboring reference areas are displayed in Figure A.1. The time series of both bridges feature significant temporal trends, indicating horizontal movements.

A.2. Temporal Evolution of Estimated Subsidence in Referencing Scenario 1
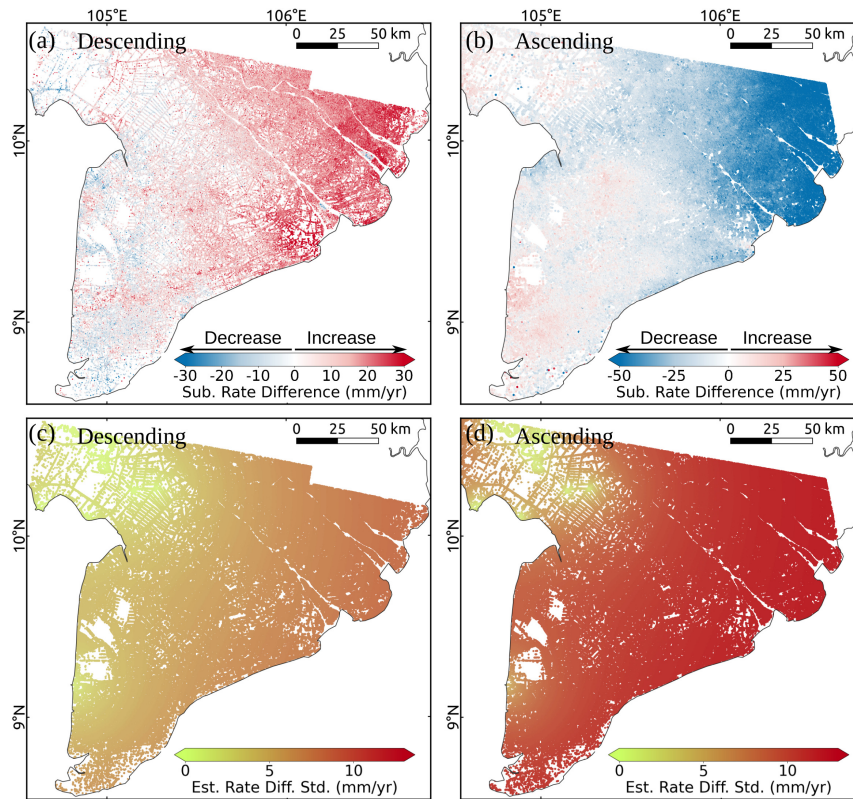
Figure A.2.: (a)-(b) Difference in estimated subsidence rates between the periods Oct. 2019 to Apr. 2022 and Apr. 2017 to Oct. 2019 in the descending and ascending stack, respectively, in referencing scenario 1. (c)-(d) Estimated standard deviation of the rate difference calculation in (a)-(b). Only (T)PSs which cover the whole period of Apr. 2017 to Apr. 2022 are displayed in (a)-(d).